| | |
|---|---|
| 題目(和文) | 大気圧マイクロ波プラズマにより生成された反応場における粒子製造 |
| Title(English) | Particle preparation in reactive field induced by atmospheric pressure microwave plasma |
| 著者(和文) | 金東旭 |
| Author(English) | Dong-Wook Kim |
| 出典(和文) | 学位:博士(工学),<br>学位授与機関:東京工業大学,<br>報告番号:甲第9444号,<br>授与年月日:2014年3月26日,<br>学位の種別:課程博士,<br>審査員:関口　秀俊,鈴木　正昭,Wiwut Tanthapanichakoon,森　伸介,下山　裕介,朴　東化 |
| Citation(English) | Degree:Doctor (Engineering),<br>Conferring organization: Tokyo Institute of Technology,<br>Report number:甲第9444号,<br>Conferred date:2014/3/26,<br>Degree Type:Course doctor,<br>Examiner:,,,,, |
| 学位種別(和文) | 博士論文 |
| Type(English) | Doctoral Thesis |

Doctoral Thesis Academic Year 2013

# Particle preparation in reactive field induced by atmospheric pressure microwave plasma

Dong-Wook Kim

11D09023

Supervisor: Professor Hidetoshi Sekiguchi

**Department of Chemical Engineering**

**Graduate School of Science and Engineering**

**Tokyo Institute of Technology**

# Contents

# Chapter 1

# Introduction

## 1.1. Plasma

Nowadays, the term “plasma” have been frequently referred to in not only the research field but also the daily life. Then what is the plasma? The definition of plasma is “gaseous state which consists of electrons, ions and neutral species” [1]. Although a plasma is definitely a kind of the gaseous state, someone used to mention plasma as the fourth state of matter followed by solid, liquid and gas since transitions from solid to liquid, from liquid to gas, from gas require commonly transition energy.

The plasma is easily observed in nature. One of those may be the Sun which mostly consists of the ionized hydrogen and the ionized helium. The lightning, the aurora and the universe are also in the plasma state. There are the numerous applications of the plasma even in the industrial field such as etching processing, display and welding [2-4].

In contrast to an ordinary gas, plasma has some unique features. First, plasma is electrically conducting due to electrons and ions. However, plasma is still electrically neutral because of balance between overall negative and positive charges called as quasi-neutrality. Second, plasmas offer very high energy density. Third, plasma can generate the highly reactive chemical species such as radicals, excited species as well as electrons and ions. The application of these properties enables to perform the distinct process from the traditional process.

Electron density, electron temperature and pressure are an important factor to determine the properties of the plasma. The classification of plasmas as a function of electron density and electron temperature is shown in Fig. 1.1 [1]. The electron density is related to the ionization degree which is a ratio of density of charged species to that of neutral gas. The plasma with the ionization degree close to unity is called completely ionized plasma such as the Sun and nuclear fusion plasma. The plasma with the low ionization degree called weakly ionized plasma is focused on the industrial application.

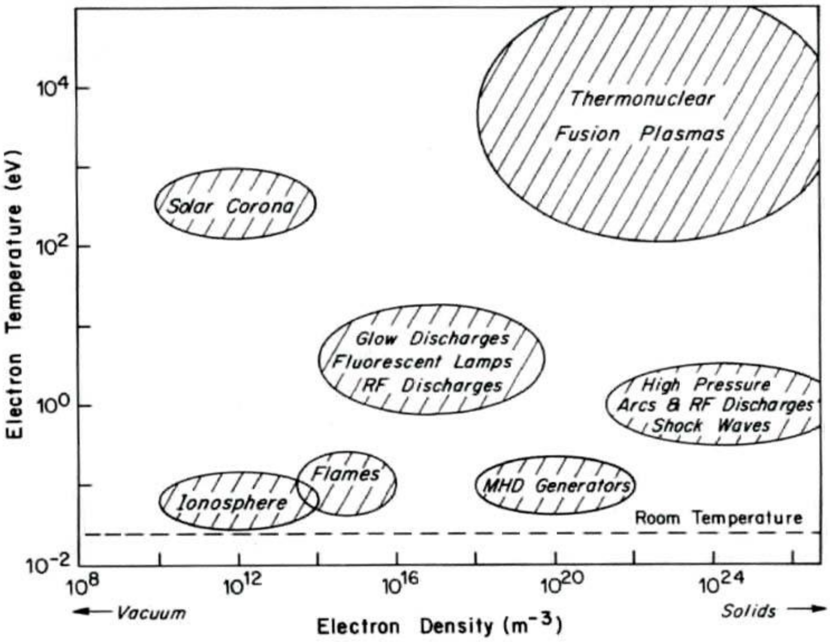

**Fig. 1.1**. Classification of plasmas

## 1.2. Plasma in local thermodynamic equilibrium

The temperature in the plasma bulk is determined by the temperature of the neutral species and ions called as the heavy particles because the masses of these are much higher than the mass of the electron. In the initial stage of the plasma generation, the electron is excited in the electric field. Therefore the energy transfer from the electron to the heavy particle directly relates to the plasma temperature. Local Thermodynamic Equilibrium (LTE) in plasma means kinetic equilibrium in which the heavy particle temperature approaches the electron temperature.

The difference of the temperature between the electron and the heavy particle is expressed by

$$\frac{T_e - T_h}{T_e} = \frac{3\pi m_h}{32 m_e}\left(\frac{e l_e E}{3kT_e/2}\right)^2 \qquad (1.1)$$

where $T_e$ and $T_h$ are the temperature of the electron and the heavy particle, $m_e$ and $m_h$ are the mass of the electron and the heavy particle, $e$ is the electric charge of the electron (-1.602×10$^{-19}$C), $l_e$ is the mean free path of the electron, $E$ is the electric field and $k$ is the Boltzmann constant. Since $T_e = T_h$ is required for LTE, the energy acquired by the electron in an electric field between collisions ($el_eE$) must be much smaller than the average kinetic energy of the electron ($3kT_e/2$). Because of $l_e \sim (1/p)$ where $p$ is pressure, transformation of Eq. (1.1) permits to consider the relationship between LTE and pressure as follows;

$$\frac{T_e - T_h}{T_e} \sim \left(\frac{E}{p}\right)^2 \qquad (1.2)$$

, indicating high pressure and/or small values of *E* is required for LTE. The behavior of the electron temperature ($T_e$) and the heavy particle temperature ($T_h$) in arc plasma is shown in Fig. 1.2 where the temperature of the kinetic equilibrium is accomplished near atmospheric pressure (≈10 kPa) [1].

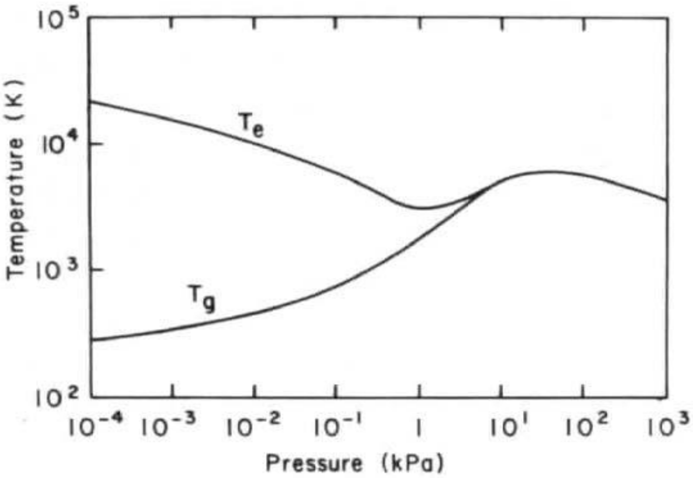

**Fig. 1.2**. Behavior of electron temperature ($T_e$) and heavy particle temperature ($T_h$) in arc plasma

## 1.3. Atmospheric microwave plasma

The plasma sustained by the centimeter-range electromagnetic waves is called microwave plasma. Fig. 1.3 shows pictures of the atmospheric microwave air plasma. After the breakdown of the initial gas flowing in the dielectric discharge tube, the microwave travels the tube as the energy transfer medium to sustain the discharge [5]. As the microwave travels along the tube, the microwave losses energy to induce the non-uniformity of the plasma properties along the tube-axis direction. Finally the plasma terminates at which the microwave does not have enough energy to sustain discharge or the dielectric tube is no longer present. The researches have reported that the microwave plasma can be generated and sustained with various frequencies from 1 MHz to 10 GHz and at various pressures from $10^{-3}$ Pa to several hundred kPa. The pressure is an important factor to determine the temperature of the microwave plasma. The microwave plasma generated at low pressure generally below 10 kPa becomes far from LTE resulting in $T_e >> T_h$ because of the poor collisional coupling between electrons and heavy particles. As the pressure increases, the plasma approaches to LTE resulting in the increase of the plasma temperature. However, the microwave reflection becomes very high as the temperature increases (81% at 6,000K), limiting to the increase of the temperature over 5,000~6,000K [6]. It is reported that the maximum temperature of the atmospheric pressure microwave plasma is from 2,000K to 6,000K [7-11]. Therefore the atmospheric pressure microwave plasma provides reactive field having high temperature as well as reactive species.

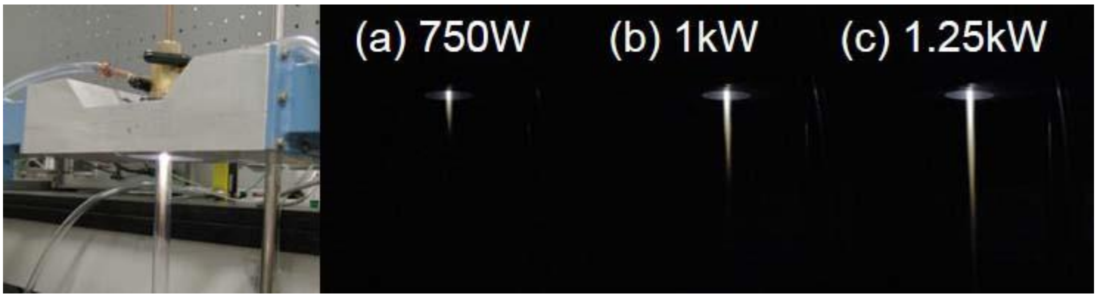

**Fig. 1.3**. Atmospheric microwave air plasma operated with various power

## 1.4. Thermal plasma

Thermal plasma is plasma that approaches to LTE, so that has the maximum temperature around or over 10,000 K and electron density ranging from $10^{21}$ to $10^{26}$ $m^{-3}$ [12-14]. From Fig. 1.2, it is not difficult to recognize that pressure near or over atmospheric pressure is required for thermal plasma. The types of thermal plasma are classified by the types of power source as shown in Fig. 1.4.

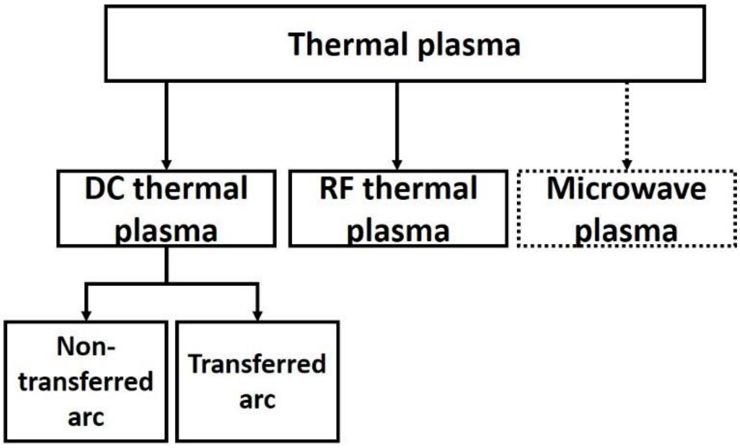

**Fig. 1.4**. Classification of thermal plasma

Direct current (DC) thermal plasma also called arc plasma is operated at current over 50 A and pressure over 10 kPa. Because of using DC power supply, DC thermal plasma requires two electrodes, those of which are anode and cathode. The plasma arc is generated between the anode and the cathode. The flow velocity of the order of 100 m/s produced in the DC thermal plasma torch makes large gradient of the plasma properties such as temperature, electron density along the plasma flow [15]. The DC thermal plasma can be classified by the arrangement of the electrodes as shown in Fig. 1.5. Non-transferred arc plasma torch has both anode and cathode. The plasma arc generated between the electrodes is transferred to the torch exit nozzle by the gas flow. Transferred arc plasma torch only has an anode itself but the conductive raw material works as cathode. The plasma arc is generated between the torch and the raw material.

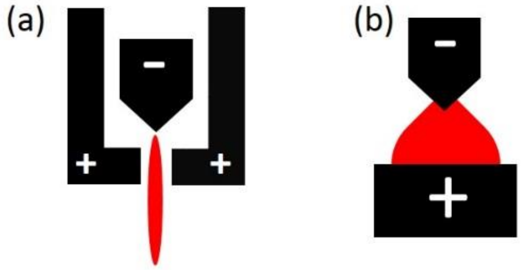

**Fig. 1.5**. Types of DC thermal plasma;

(a) non-transferred plasma, (b) transferred plasma

Radiofrequency (RF) thermal plasma also called inductively coupled plasma (ICP) is generated by high frequency electric current which passes through a solenoid coil providing an axial magnetic field. Generally RF ranged from 0.1 MHz to 100 MHz is required to sustain the plasma. Since RF plasma torch does not have electrodes, the contamination from the electrode corrosion which is one of the problems in the DC thermal plasma processing [16] do not have to be considered. The flow velocity of the RF plasma is lower than that of the DC thermal plasma so that the gradient of the plasma properties is small and the residence time of the flow becomes longer than that in the DC thermal plasma. Because of these properties, the RF plasma is frequently used for material processing.

Microwave plasma explained in the previous section is sometimes classified to thermal plasma because it becomes close to LTE under atmospheric pressure. The microwave plasma has similar properties (e.g. the electrodeless discharge, the low flow velocity) with the RF plasma but except temperature.

The temperatures and the flow velocities of the DC thermal plasma, the RF thermal plasma and microwave plasma are compared in Fig. 1.6.

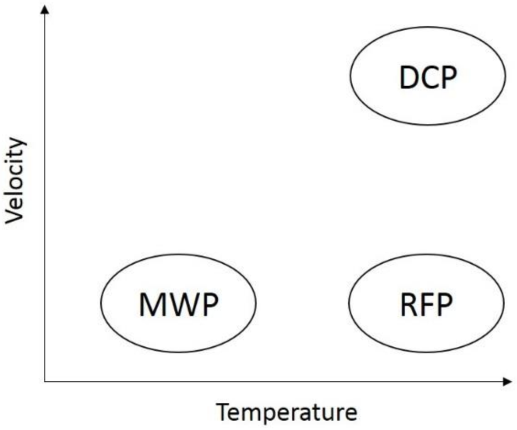

**Fig. 1.6**. Comparison of thermal plasmas

(DCP: DC thermal plasma, RFP: RF thermal plasma, MWP: microwave plasma)

## 1.5. Particle preparation using the plasma

The role of the ultrafine particle in the material processing has grown as raw material due to miniaturization of product [17-19]. Therefore the particle preparation technique has also become more important for the industrial application. The traditional particle preparation techniques such as hydrothermal synthesis [20], sol-gel process [21], and precipitation method [22] have been researched for a long time and have shown that it is proper to produce novel particles and to control those formation mechanisms. However the organic solvent used in those techniques makes environmental problems in mass production and reduces the purity of the product. Among the problems, application of the plasma to the particle preparation is expected as a promising field. Especially the particle preparation using the thermal plasma is one of the valuable field having the possibility for mass production and production of novel material. The thermal plasma which is in LTE or close to LTE provides very high temperature close to or over 10,000 K which can't be obtained by conventional energy source and gaseous reactive species, inducing the unique processing. When the processing using the non-equilibrium plasma is referred, the effect of the reactive species such as radicals, ions and electrons is mainly focused. However the contribution of the temperature is mainly considered in the thermal plasma. The high temperature of the thermal plasma may induce the phase transfer or the decomposition of the material and may promote the reaction.

The most famous particle preparation using the thermal plasma may be the preparation of the ultrafine particle performed by vapor phase synthesis in which the raw material is vaporized or decomposed to the gaseous phase [23-29]. After that, the product is condensed as the temperature of the product flow is decreased. Here the introduction of the rapid cooling also called quenching enable to obtain the ultrafine particle because the quenching limits the particle growth [30-31]. The size of the obtained ultrafine particle is generally distributed from some nanometer to some hundreds nanometer although it differs by the experimental condition. The vapor phase synthesis by the thermal plasma has the following advantages.

1) Various raw material such as solid particle, bulk ingot as well as gas, liquid can be used. The vapor phase synthesis using the flame or the furnace generally uses the vapor or liquid precursor which is easily decomposed. However the plasma temperature over the boiling temperature of most of the solid material enables to apply solid precursor to the vapor phase synthesis. Introducing the solid precursor permits the mass production of the ultrafine particle as well as broaden the selection of the reaction.

2) Various reactive fields are easily generated. In the vapor phase synthesis, the gaseous condition determines the reaction. For example, the oxidation of the vaporized precursor can be performed in the oxygen atmosphere. Furthermore, the reactive species such as radicals, ions and excited gas atoms promotes the reaction which may be slow without plasma. For example, a metal vapor easily transforms to a metal nitride in the nitrogen atmosphere with the plasma, while its conversion is low without the plasma.

3) Metastable phase can be obtained by quenching. When the cooling rate is much faster than the transition rate to the thermodynamic equilibrium phase, the phase at the high temperature region freezes. From this principle, the novel metastable phase which is thermodynamically unstable at the room temperature but stable in the high temperature region such as most of spinel, solid-solution can be obtained.

4) The process is simple and continuous. The vapor phase synthesis generally does not require the pre-treatment or the after-treatment. Therefore the entire process from the raw material to the product occurs only in the plasma system. Furthermore semi-batch or

continuous process can be used for the plasma system. Due to these features, the plasma processing is considered to be desirable for the industrial application.

The vapor phase synthesis also has some problems. The frequently mentioned problems are broad particle size distribution. As mentioned above, the ultrafine particle is easily synthesized by the vapor phase synthesis, however the problem is the particle size distribution, that is, the particle with the size of some nanometer and some hundreds nanometer may co-exist. Therefore the control of the particle size distribution is one of the most important topics in the vapor phase synthesis. Another issue may be how to control the particle composition. This is not so significant problem in the single-component system but not in the multi-component system. Due to difficulty to control the diffusion and the collision of each component in the plasma region, the products with the various phases or the different composition used to be obtained. This problem still remains to be solved.

Another famous particle processing is spheroidization of the particle [32-34]. When the particle melts in the plasma, it forms the spherical liquid drop. It is similar to the plasma spray coating but the difference is the presence of the substrate. For spheroidization, the ceramic material having high boiling point is frequently referred because the particle shouldn’t be vaporized.

## 1.6. Previous researches

The previous researches have shown that the particle preparation by the microwave plasma seems not so far from that by the thermal plasma, reporting that the vapor phase synthesis also can be performed by the microwave plasma [35-38]. Since those results didn't focus on the specific feature of the microwave plasma as well as the comparison between using the microwave plasma and the thermal plasma, it is difficult to consider similarity or difference caused by using those plasmas from the results. However it is obvious that the solid precursor is hardly used in the microwave plasma processing although some researches introduced the solid precursors having a low boiling point such as zinc (b.p.1,180K) [39]. The most frequently used precursors in the previous researches are organic metallic compounds or metal chloride which have relatively low boiling point and is easily decomposed [40-43]. It may be due to the relatively lower temperature of the microwave plasma than the thermal plasma. We expect that the specific properties of the microwave plasma including the moderate temperature distinguished from the thermal plasma enable to achieve the different processing or the different results.

## 1.7. Objectives of this thesis

The main purpose of this thesis is to investigate the specific features of the microwave plasma for the particle preparation and to find out the particle formation phenomena. In this thesis, the two types of the particle preparation were investigated. The former is the dehydration of indium hydroxide to investigate the particle preparation from the solid precursor. The latter is the synthesis of the ultrafine particle in Fe-Si-O system to investigate the particle preparation from the vapor precursor. In order to find out the specific features, the results were compared with those by thermal plasma which has much higher temperature than the microwave plasma as well as those by conventional electrical furnace.

## 1.8. Structure of this thesis

This thesis is composed of five chapters as follows.

**Chapter 1** introduces the principle of the particle preparation by the plasma, the existing research and the objectives.

**Chapter 2** describes the preparation of indium oxide from dehydration of indium hydroxide. The reaction mechanism by which the indium hydroxide, the solid precursor transforms to the indium oxide are focused.

**Chapter 3** describes the synthesis of ultrafine particle from decomposition of iron pentacarbonyl [$Fe(CO)_5$] and tetraethyl orthosilicate [$(C_2H_5O)_4Si)$]. The behavior of Fe-Si-O system which is expected to determine the final products is discussed.

**Chapter 4** deals with the effect of the microwave plasma on the particle processing. The factors of the microwave plasma to affect the particle behavior are investigated.

**Chapter 5** remarks conclusions obtained from discussion and proposes the future research for the next step.

The structure of this thesis is shown in Fig. 1.7.

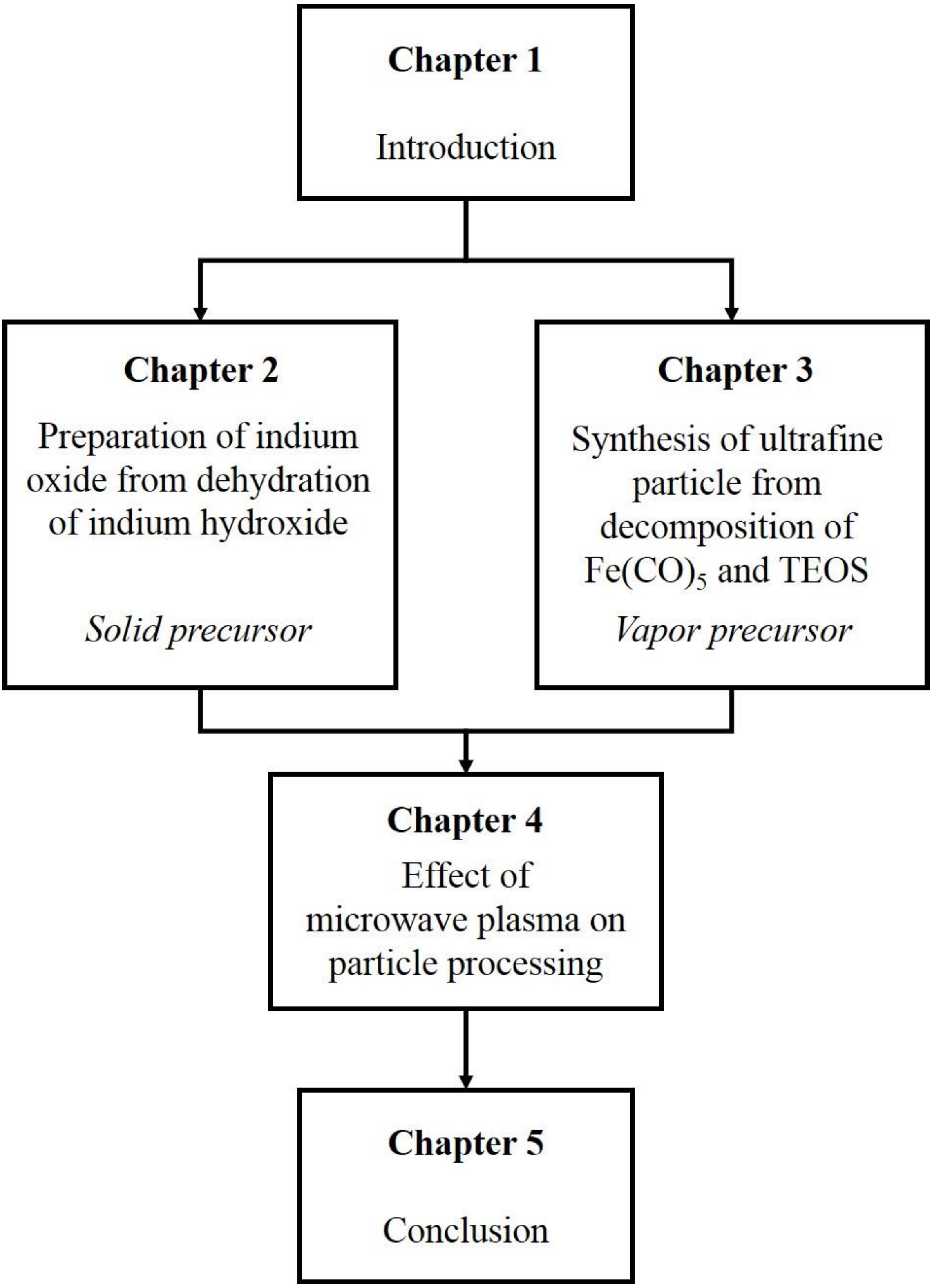

**Fig. 1.7**. Flow chart displaying structure of this thesis

# Chapter 2

# Dehydration of indium hydroxide

## 2.1. Introduction

### 2.1.1. Indium oxide and dehydration of indium hydroxide

Indium oxide ($In_2O_3$) is an n-type semiconductor with band-gap energy of 3.6 eV. It is optically transparent and has a high electric conductivity by doping its impurities [44]. Tin-doped indium oxide (ITO) is the most widely used transparent conductive oxide (TCO) in the display field [45]. As $In_2O_3$ is the base material of TCO, techniques related to $In_2O_3$ have attracted much attention. The melting temperature of $In_2O_3$ is 2,183K, and its vaporization temperature is about 2,800K.

Dehydration of indium hydroxide [$2In(OH)_3 \rightarrow In_2O_3 + 3H_2O$] is a favorable method to obtain $In_2O_3$ because of some of its advantages [46-48]. First, $In(OH)_3$ can be simply synthesized with a desirable morphology. Second, the macro-morphology of the as-prepared $In(OH)_3$ is maintained during the dehydration to convert it into $In_2O_3$. As a result, morphology-controlled $In_2O_3$ can be obtained. Similar results have been reported for other hydrates [49-51]. This process generally includes not only the dehydration but also the crystallization of the product. Therefore, the actual process is performed at a higher temperature for some hours in an electric furnace to obtain a high-crystalline product, although the dehydration of $In(OH)_3$ starts at nearly 480 K.

## 2.1.2. Purpose of this chapter

The main purpose of this chapter is to investigate the behavior of the solid particle precursor injected into the atmospheric microwave plasma region, for which $In(OH)_3$ is chosen as the solid particle precursor. The melting point and the boiling point of $In(OH)_3$ is unknown because it transforms to $In_2O_3$ by dehydration reaction at about 500 K. If the injected $In(OH)_3$ is dehydrated in the plasma flow, the melting point and the boiling point of $In_2O_3$ becomes important. Since the temperature of the microwave plasma used in this thesis ($\approx$3,000 K) is not so far from the boiling point of $In_2O_3$, $In_2O_3$ obtained from the dehydration is expected to remain without evaporation. Furthermore, the additional energy supply followed by the dehydration is expected to promote the crystallization of the obtained $In_2O_3$ like as heat treatment in the furnace. For the investigation of the specific reaction by the microwave plasma, the results are compared with those by the DC thermal plasma expected to evaporate $In_2O_3$ and the conventional electric furnace generally used for the dehydration of $In_2O_3$. From the comparison, it is discussed that which reaction step induces the specific reaction by the microwave plasma.

## 2.2. Experiments

### 2.2.1. Preparation of $In_2O_3$ using microwave plasma

The experiment setup is shown in Fig. 2.1. The following is the detailed explanation of the apparatus. The microwave generator (MG-213V-2P, Micro-densi) can produce 2.45GHz microwave through continuous wave (CW) mode with the maximum power of 1.3 kW or pulse wave (PW) mode with the maximum power of 2.0 kW. In this thesis, the microwave generator was operated in CW mode with variable power. The produced microwave from the microwave generator passed through the isolator (MDI-2H, Micro-densi), the power monitor (MMO-2H, Micro-densi) and the three stab tuner (MTS-2H, Micro-densi) and then was transmitted the resonance cavity (WR284, IDX Company, Ltd.) by $TE_{10}$ mode waveguide which is made from aluminum. The isolator protects the microwave generator by separating the reflected microwave. The power monitor was connected with the power supply and then enabled to indicate the power generated from the magnetron. The three stab tuner enabled to control the reflected wave from the end of the waveguide. During the experiments, the reflected wave was kept to be the minimum value by controlling the valve at the tuner. The resonance cavity called as “surfaguide” has a tapered morphology and enabled to form the concentrated microwave electric field in the dielectric material that was the quartz tube in this thesis. For the first ignition of the plasma, a high voltage spark generated by vacuum leak detector was applied from the outlet of the quartz tube. Once the spark is generated in the quartz tube and then plasma is sustained without a further supply of the frequency source. This plasma called as surface wave sustained discharge grows in the direction parallel to the tube axis.

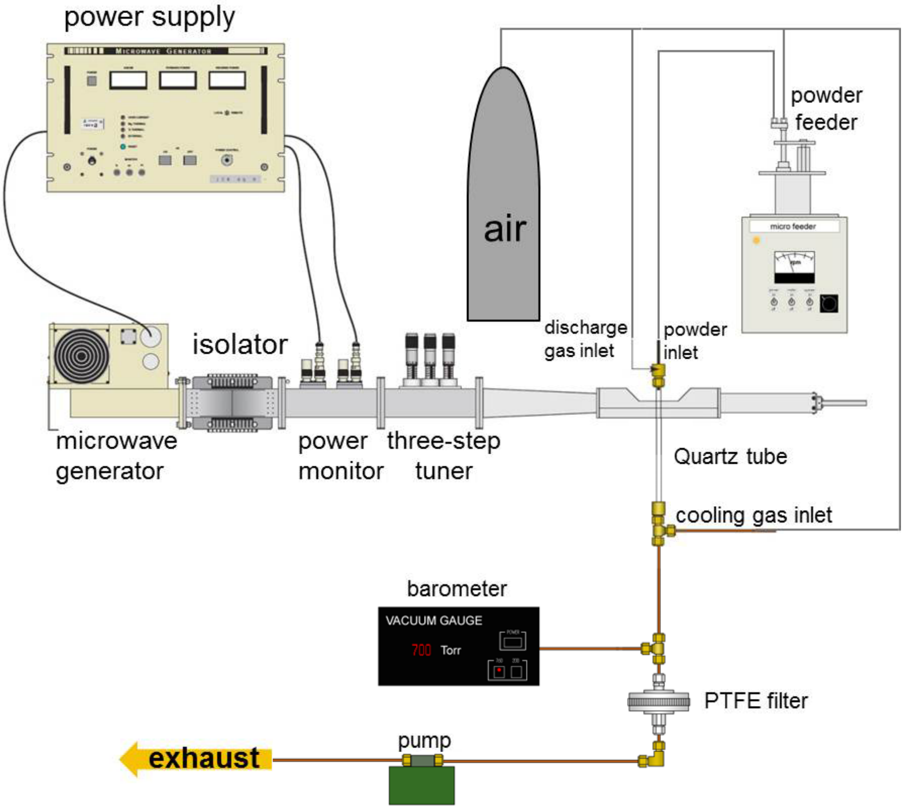

**Fig. 2.1**. Experimental apparatus of microwave plasma

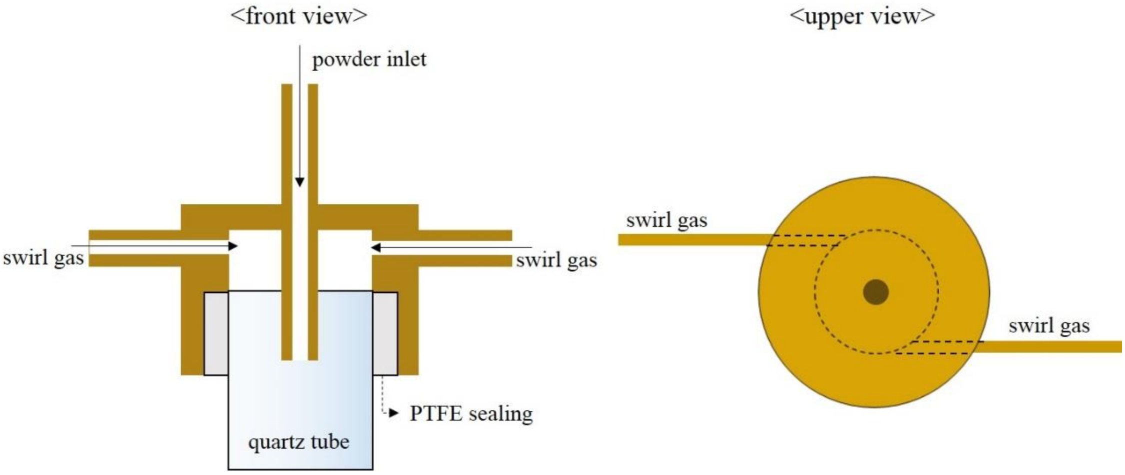

**Fig. 2.2**. Detailed structure of injection block

The reactor was composed of an injection block, the quartz tube, the cooling pipe, the filter and the pump. Fig. 2.2 shows the detailed structure of the injection block. The injection block has three nozzles. The two nozzles perpendicular to the tube were positioned tangentially to inlet the swirl gas. Introducing the swirl gas prevented the quartz tube to melt during the plasma generation as well as to stabilize the plasma generation by reducing the pressure a little in the central region of the tube. The nozzle parallel to the tube was to inject the powder with carrier gas. The quartz tube was chosen as the reaction tube due to the following advantages. First, the quartz reduces the dielectric loss of the microwave, leading to the efficient generation of the plasma. Second, high melting point (1,950K) and low thermal expansion coefficient permit to apply at the high temperature processing. Third, the high optical transmittance to broad wavelength range enables to measure the plasma condition. The quartz tube was fixed to the injection block with the polytetrafluoroethylene (PTFE) sealing. The cooling gas was introduced to quench the product flow and to prevent the filter to burn. The filter was composed of stainless steel holder and PTFE filter film with a pore size of 1 μm. The filter film was exchangeable and was fixed in the holder. The pump was operated to control the pressure in the reactor. The pump was set up to maintain 700~750 torr, the slightly lower pressure than the atmospheric pressure which prevented the back flow of the prepared particle.

The procedure to generate the atmospheric air plasma is following. First, argon was tangentially introduced in a quartz tube (I.D. : 9 mm). Second, the microwave generator was turned on. Third, the high frequency generator (BD-10A, Electro-technic products, Inc.) was operated to generate a spark. Then the argon filament discharge was generated. Next, the argon was gradually substituted to the air. Finally the atmospheric pure air plasma jet was formed.

$In(OH)_3$ (99.99% purity, Aldrich Co.) as the raw material was fed to the plasma jet through the powder injection nozzle with the air carrier gas using a powder feeder (type: MF, Technoserve Co., Ltd.). The feeding rate was determined by the combination between the carrier gas flow rate and the rotation rate of the stirrer and was estimated by measuring the weight of the remained powder after the experiments. In all experiments, the feeding rate was maintained as 0.1 g/min with the carrier gas flow rate of 1 L/min and the rotation rate of 250 rpm (rotations per minute). The fed particles passed through the quartz tube and then were collected in the filter. The detailed experimental conditions for the microwave plasma are summarized in Table 2.1. The experiments were performed with the different microwave power; 750W, 1,000W and 1,250W. The increase of the microwave power led to the increase of the gas temperature and the extension of the discharge region.

**Table 2.1**. Detailed experimental conditions for microwave plasma

| Power | 750W | 1000W | 1250W |
|---|---|---|---|
| Pressure | 700~750 torr | | |
| Discharge gas | Air : 10 L/min | | |
| Carrier gas | Air : 1 L/min | | |
| Cooling gas | Air : 5 L/min | | |
| Feeding rate | 0.1 g/min | | |
| Quartz tube | Outer diameter : 11 mm<br>Inner diameter : 9 mm<br>Length : 350 mm | | |

### 2.2.2. Preparation of $In_2O_3$ using DC thermal plasma

The experimental setup of thermal plasma shown in Fig. 2.3 is composed of a DC power supply, a plasma torch and a reactor. The DC power supply with the maximum power of 20kW was connected to a cathode and an anode of the plasma torch and enabled to control the discharge current. The discharge voltage changed with the variation of the discharge current to maintain the constant power according to equation $P = VI$ ($P$ is power, $V$ is voltage and I is current). In addition, the DC power supply controlled the cooling water flow in the plasma torch. The plasma torch was the non-transferred type which was composed of a tungsten anode, a copper cathode and a polyimide insulation block. The plasma torch had the cooling path where the cooling water flowed to cool the electrodes. The polyimide insulation block fixed the anode and prevents the contact between the electrodes. The reactor made from stainless steel had a double walled water-cooling system for the rapid quenching of the product flow. The pressure controller attached to the reactor enabled to control the reactor pressure. Similarly to the case using the microwave plasma, the reactor pressure was maintained close to 700~750 torr under the experimental conditions. The detailed experimental conditions for the DC thermal plasma are summarized in Table 2.2.

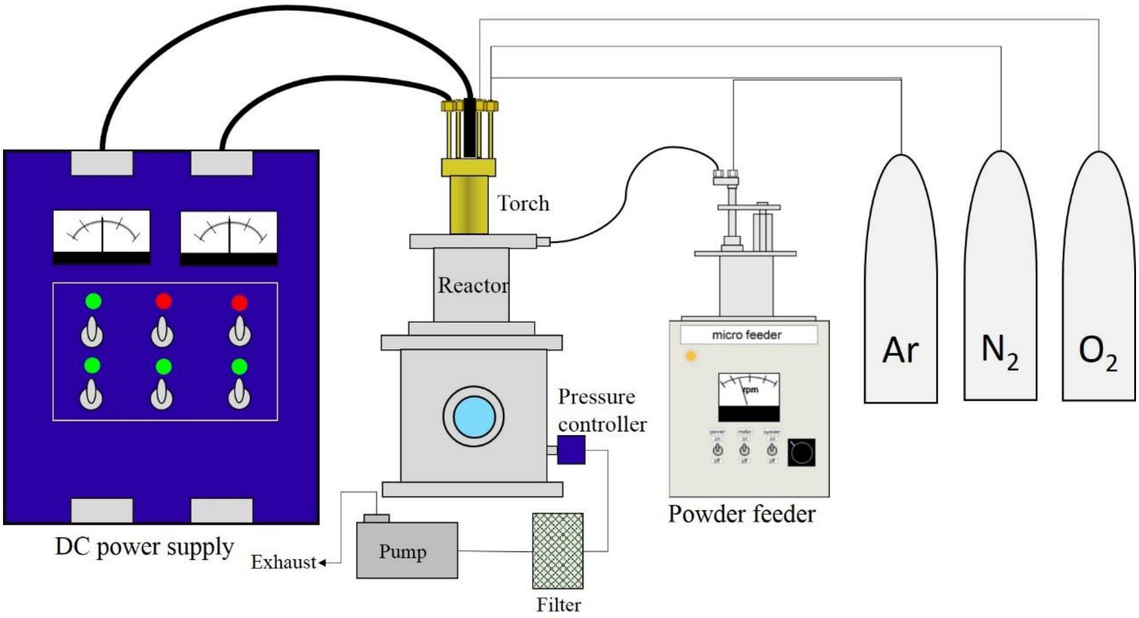

**Fig. 2.3**. Experimental apparatus of DC thermal plasma

**Table 2.2**. Detailed experimental conditions for thermal plasma

| Power (kW) | 6 kW | 9 kW |
|---|---|---|
| Pressure (torr) | 700~750 torr | |
| Discharge gas (L/min) | Ar : 10 | Ar : 8<br>$N_2$ : 2 |
| Additional gas (3 L/min) | $O_2$ : 3 | |
| Carrier gas (L/min) | Ar : 1 | |
| Feeding rate (g/min) | 0.1 | |

In the non-transferred plasma torch, the electric field is formed at the gap between the anode and the cathode. When the high voltage was applied with discharge gas flow, the plasma was generated at this gap and simultaneously flows to the torch exit. The powder was injected perpendicularly to the plasma jet flow through the nozzle positioned at the upper part of the reactor with the feeding rate of 0.1 g/min. As the experimental variables, the experiments were performed under the discharge power of 6 kW and 9 kW, respectively. Here, nitrogen was mixed with the discharge gas to increase the power.

### 2.2.3. Preparation of $In_2O_3$ using an electric furnace

Ceramic tube furnace (ARF-30KC, Asahi Rika Seisakusho) with the maximum power of 500W was used for the dehydration of $In(OH)_3$ as the conventional method. The furnace was insulated with ceramic foam. The temperature of the furnace was measured by K-type thermocouple located on top of the alumina tube. 0.5 g of $In(OH)_3$ put in the alumina tube was heated by the furnace with natural convection at 773 K, 1,023 K and 1,273 K for 90 minutes, respectively.

Finally the samples prepared from the experiments were named as in Table 2.3 for convenience.

**Table 2.3**. List of the samples

| Classification | Sample name | Experimental conditions | | |
|---|---|---|---|---|
| | | Method | Operating variables | |
| MWPs | MWP750 | Microwave plasma | Power | 750W |
| | MWP1000 | | | 1,000W |
| | MWP1250 | | | 1,250W |
| EFs | EF773 | Electric furnace | Temperature | 773K |
| | EF1023 | | | 1,023K |
| | EF1273 | | | 1,273K |
| TPs | TP6 | Thermal plasma | Power | 6kW |
| | TP9 | | | 9kW |

## 2.2.4. Characterization

The phase composition of the obtained particles was analyzed with an X-ray diffractometer (XRD, X'Pert-MPD-OEC, Philips) utilizing Cu Kα radiation with a wavelength of 1.540598Å. All samples were measured twice. For the first measurement, the scanned range of 2θ was from 20° to 80° with step size of 0.02° and time per step of 0.4 s/step. This measurement aimed to confirm the change of the phase composition. For the second time, the scanned range of 2θ was from 85° to 86.5° with step size of 0.01° and time per step of 20 s/step. The second measurement was to calculate the crystallite size from Schrerr equation as follows;

$$D = \frac{K\lambda}{\beta cos\theta} \qquad (2.1)$$

where $D$ is crystallite size, $K$ is shape factor which varies with the actual crystalline shape but is determined as 0.9 here, $\lambda$ is X-ray wavelength (1.540598Å), $\beta$ is full width at half maximum (FWHM) of a peak and $\theta$ is half of 2θ at the peak.

The morphology and surface of the obtained particles were observed with a scanning electron microscope (SEM, VE-7800, Kyence) for low magnification and a field emission-scanning electron microscope (FE-SEM, S4500, Hitachi) for high magnification. Gold for SEM or Platinum-Palladium for FE-SEM was coated on the surface of the samples by sputter to reduce charging effect.

The conversion of the reaction was confirmed via a thermogravimetry/differential thermal analysis (TG, TP2, Rigaku). Above all, 15 mg of each sample put in an alumina pan was placed on the scale of TG and then 50 ml/min of nitrogen purge gas was introduced to make inert condition. The heating rate was set up as 10K /min and the target temperature was 673 K. When the temperature arrived at the target temperature, the operation stopped without holding time.

The state of the chemical bonding was investigated via an X-ray photoelectron spectroscopy (XPS, PHI 5000 Versa Probe, ULVAC-PHI Inc.). The X-ray of mono Al-Kα was used for the measurement. Each sample was stuck on a copper tape. The ranges of the measurement were from 440 to 460 eV for $In3d_{3/2}$ peak and $In3d_{5/2}$ peak and from 523 eV to 543 eV for O1s peak. It is noted that XPS can analysis on the 10 nm depth of the sample surface.

# 2.3. Results and discussion

## 2.3.1. Phase composition of the prepared powder

**XRD**

Fig. 2.4 shows the XRD patterns of the raw material and the products. The peaks of the cubic $In_2O_3$ (PDF #01-071-2195) appeared, and most of the peaks that indicated the cubic $In(OH)_3$ (PDF #01-073-1810) disappeared in all the products. Only the weak peak that indicated the $In(OH)_3$ at 22 degrees remained in the XRD patterns of the MWPs and the TPs. This might be because $In(OH)_3$ was sensitive to the X-ray at 22 degrees, at which the strongest peak of the $In(OH)_3$ appeared, although the products included only a small amount of crystalline $In(OH)_3$.

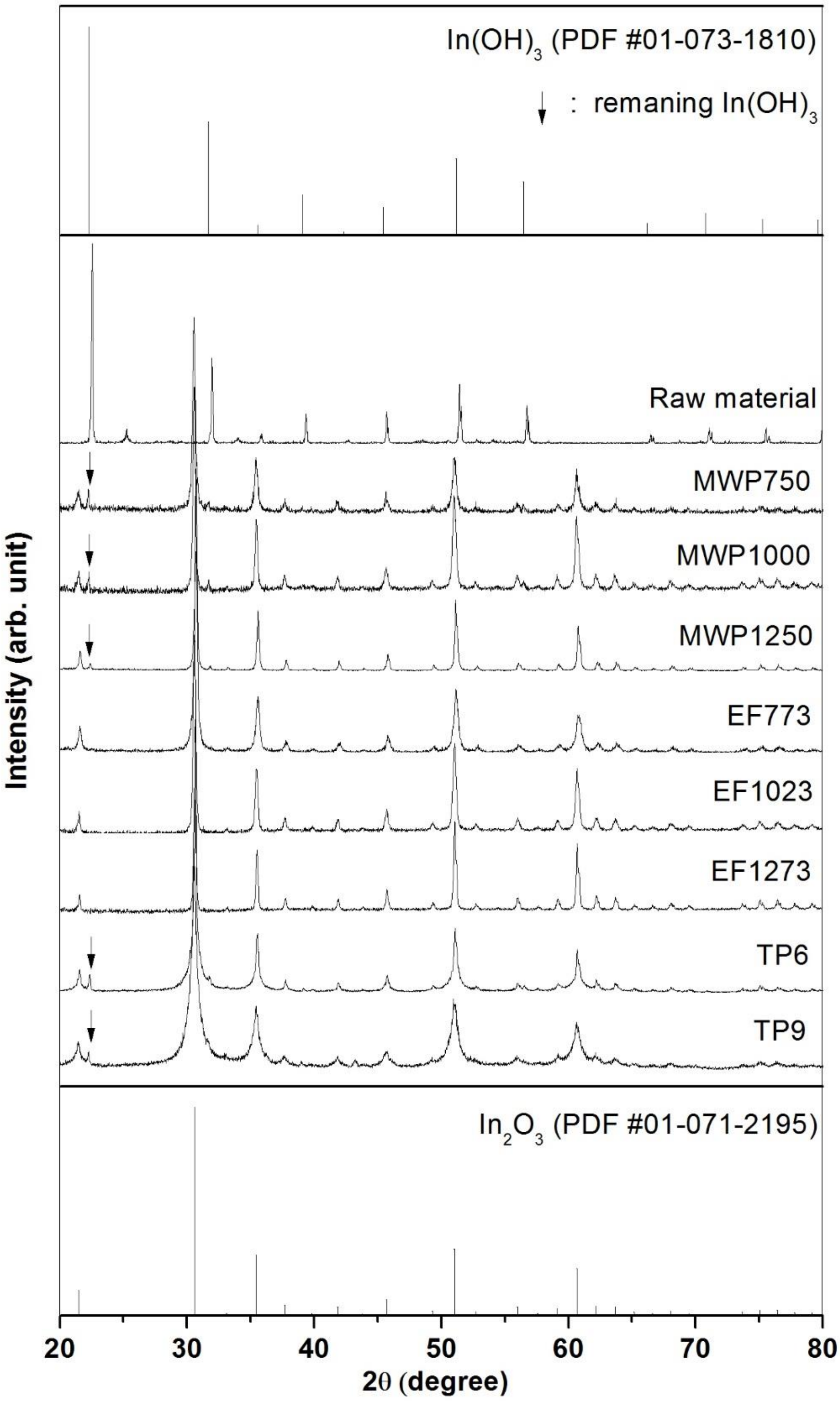

**Fig. 2.4**. XRD patterns of In(OH)$_3$ and the products

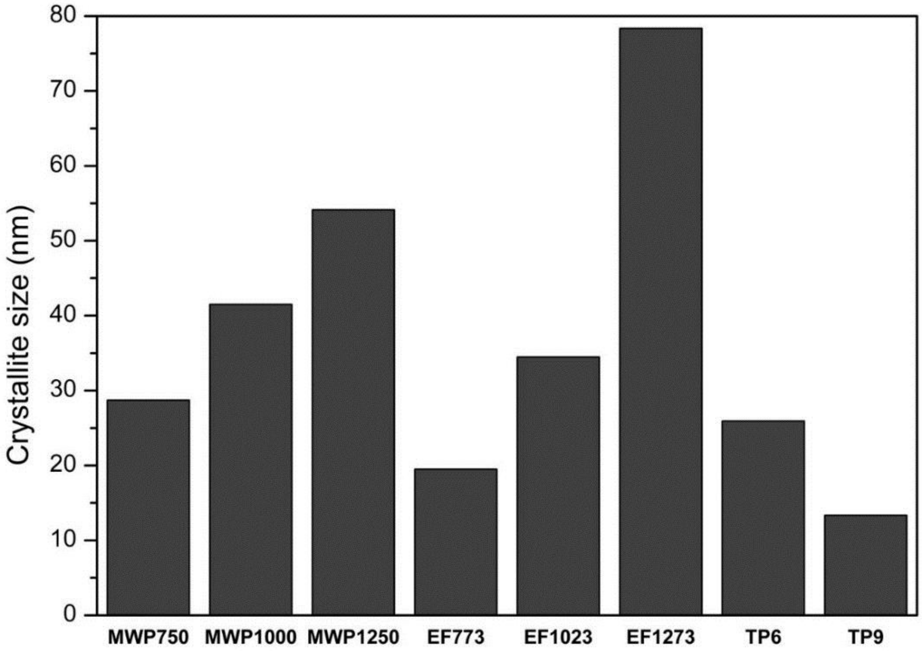

**Fig. 2.5**. Crystallite sizes calculated by Scherrer equation

The crystalline sizes of the prepared $In_2O_3$ were calculated using Scherrer equation. The results are shown in Fig. 2.5. In both the cases of the microwave plasma and the electric furnace, the crystalline size increased as the microwave power and the furnace temperature increased, respectively. The crystalline sizes of the TPs were relatively small because the fast cooling controlled the particle growth.

### TG/DTA

To estimate the conversion quantitatively, TG analysis was performed. General TG/DTA curve of $In(OH)_3$ in Fig. 2.6 shows a sharp endothermic peak around 550K indicating the dehydration of $In(OH)_3$. The following broad endothermic peak indicates that the crystallization of the obtained $In_2O_3$. Fig. 2.7 shows TG curve of the MWP750, MWP1250 and raw material from 373 K to 773 K. The weight decreases of the MWP750, MWP1250 and raw material were about 1%, 0.4% and 15.9%, respectively, for the dehydration. The raw material had been completely dehydrated during the TG analysis, the conversions of the dehydration for the MWP750 and MWP1250 would have been 93.7% and 97.5%, respectively. When the microwave power was 750 W, the conversion was relatively low because there was less microwave power.

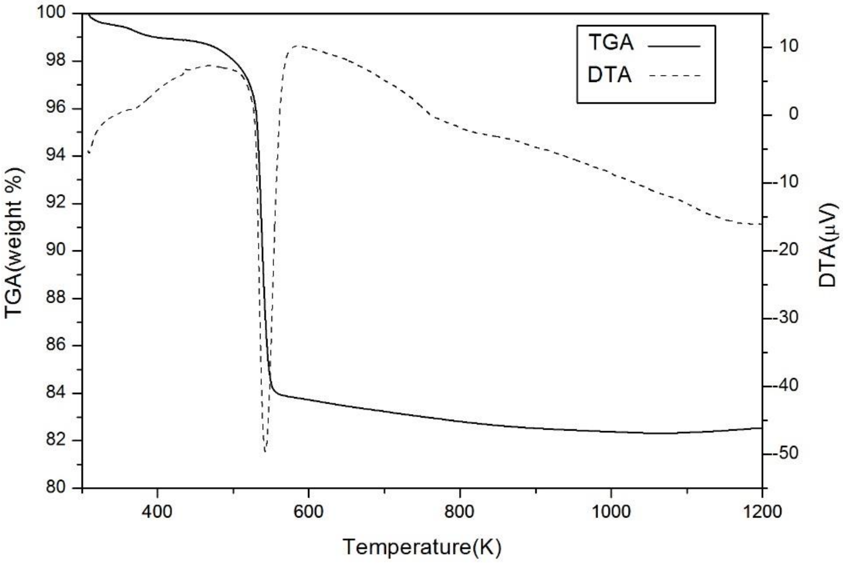

**Fig. 2.6**. General TG/DTA curve of $In(OH)_3$

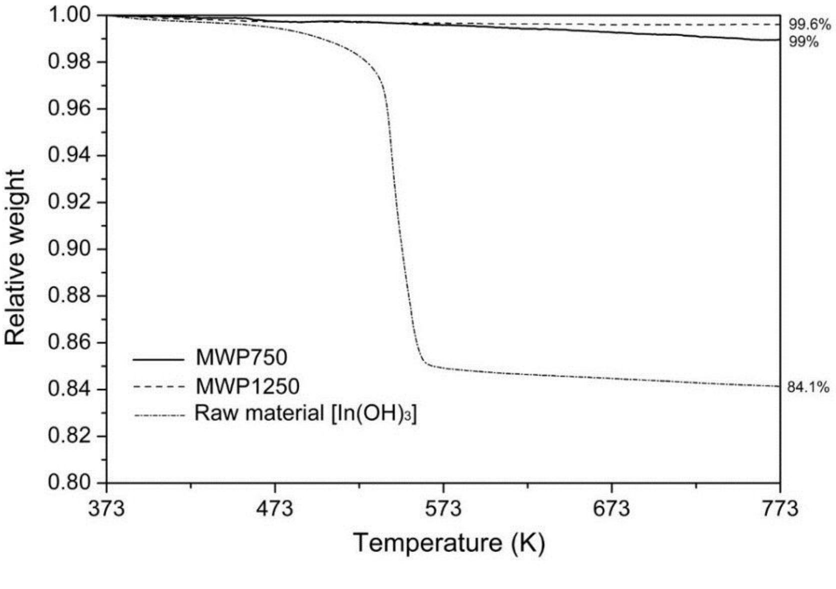

**Fig. 2.7**. TG curves of raw material, MWP750 and MWP1250

**XPS**

XPS analysis was performed to investigate the difference in the chemical bonding states for the O1s, In3d3/2 and In3d5/2 bonds which vary with the state of the bonded atom.

First, the peaks indicating O1s were observed. Each peak was split into two or three symmetric peaks. The ratio of each oxygen component to the O1s bond was calculated from the ratio of the area under each fitted curve to the area of all O1s related peak. Fig. 2.8 shows that the peaks can be classified into three types; MWP750 composed of $O^{2-}$($In_2O_3$), $O^{2-}$($In(OH)_3$) and $O^-$/$OH^-$, the group of MWP1250, EF773 and EF1273 composed of $O^{2-}$($In_2O_3$) and $O^-$/$OH^-$, the group of TP6 and TP9 composed of $O^{2-}$($In_2O_3$), $O^{2-}$($H_2O$) and $O^-$/$OH^-$. Here $O^{2-}$($In_2O_3$) indicates the $O^{2-}$ in the bulk $In_2O_3$ lattice [52-55]; $O^-$/$OH^-$, the oxygen components with an additional charge; $O^{2-}$($In(OH)_3$), the remaining $In(OH)_3$; and $O^{2-}$($H_2O$), the oxygen in the water molecule.

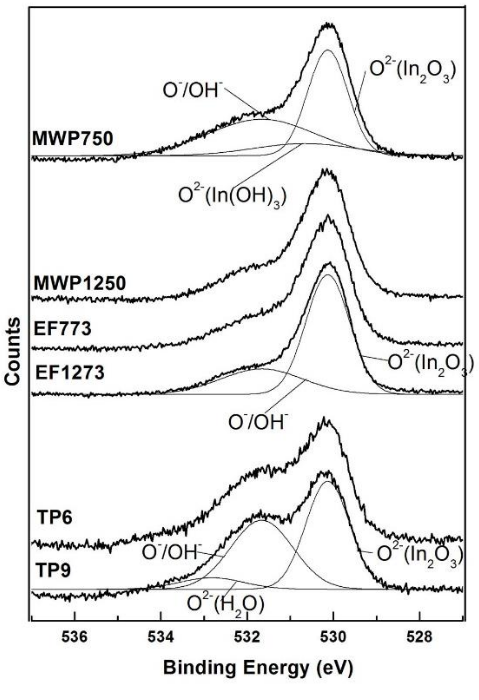

**Fig. 2.8**. The fitted peaks of O1s curves

From the curves fitted in Fig. 2.8, the relative ratio of each oxygen component was calculated as shown in Fig. 2.9.

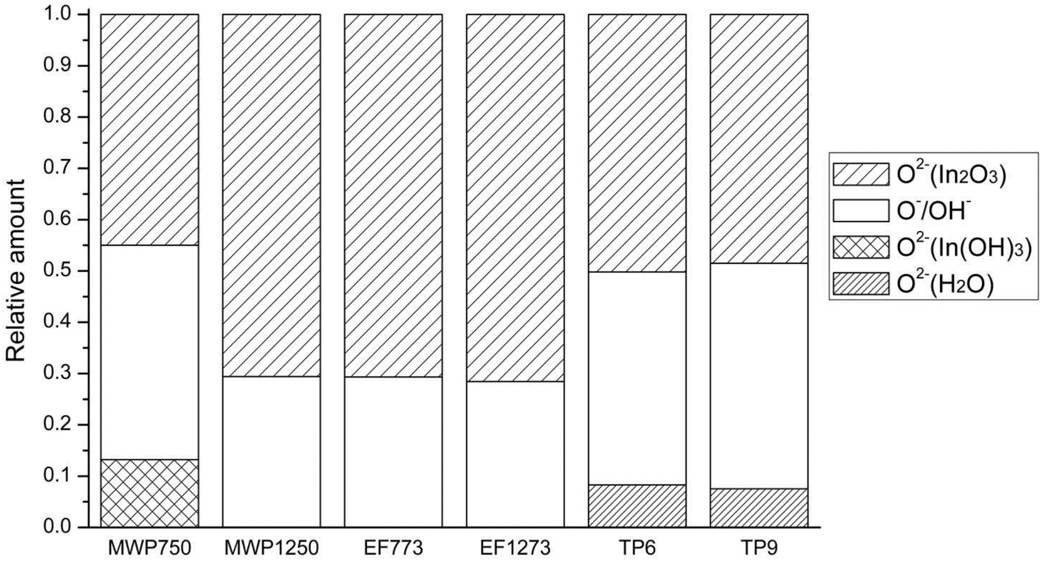

**Fig. 2.9**. Composition of oxygen atoms in each product calculated from O1s peaks

The $O^{2-}(In(OH)_3)$ was only observed at MWP750. It suggests that some $In(OH)_3$ still remained without the destruction of their lattice structure in MWP750. Next the $O^-/OH^-$ is focused. That is regarded as the oxygen with an additional charge in the transition state and at the surface layer of the $In_2O_3$ lattice [56]. MWP1250, EF773 and EF1273 had similar $O^-/OH^-$ ratios, close to 0.3. If the EF samples were assumed to be dehydrated completely, the $O^-/OH^-$ values of the samples might be of the oxygen at the surface layer shown in Fig. 2.10. Therefore, the ratios of MWP1250, EF773 and EF1273 in Fig. 2.9 implies two things; one is that MWP1250 was completely dehydrated as like as EF773 and EF1273, another is that $In_2O_3$ that is completely dehydrated by the microwave plasma is on the similar chemical state with those by the electric furnace.

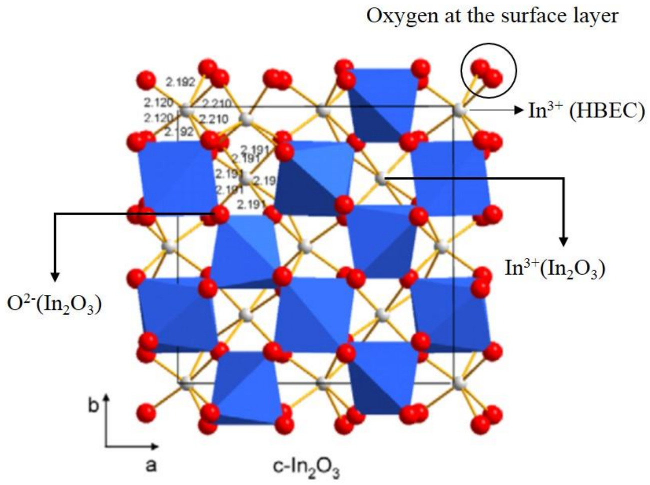

**Fig. 2.10**. Lattice model of In2O3 including the oxygen at the surface layer

(grey sphere : indium atom, red sphere : oxygen atom)

The large contribution of the surface oxygen to this value is because XPS can analyze the top of 1-10 nm below the surface layer. On the other hand, the MWP750 and the TPs had higher values (0.4-0.45). The $O^-/OH^-$ of the MWP750 was derived from both the surface oxygen and the intermediate oxygen bond in the transition state, which means the lattice structure of $In(OH)_3$ was destroyed but was not completely converted to that of $In_2O_3$. The high $O^-/OH^-$ ratio of the TPs may be related to the formation of the nanoparticles that will be discussed with SEM images later. The large surface area of the nanoparticles contributed to the increase in the surface oxygen. The presence of $H_2O$ is also related to it because $H_2O$ can easily adsorb on the surface of the nanoparticles.

To confirm the results obtained from the analysis of O1s bond, the chemical bonding states of In3d were also confirmed. The curves were split into two peaks which indicates $In^{3+}(In_2O_3)$ and High Bonding Energy Component (HBEC) of $In^{3+}$ expect MWP750 having also $In^{3+}(In(OH)_3)$ as shown in Fig. 2.11. Here $In^{3+}$(HBEC) means In-O bond in insufficient oxygen structure, which agrees with $O^-/OH^-$ in O1s curves [57]. In Fig. 2.12, the ratios of $In^{3+}$(HBEC) in In3d bond and $O^-/OH^-$ in O1s bond were compared , showing good agreement.

As the results of XPS analysis, it is confirmed that the chemical bonding states of the MWPs and the EFs is almost same although MWP750 wasn't completely dehydrated.

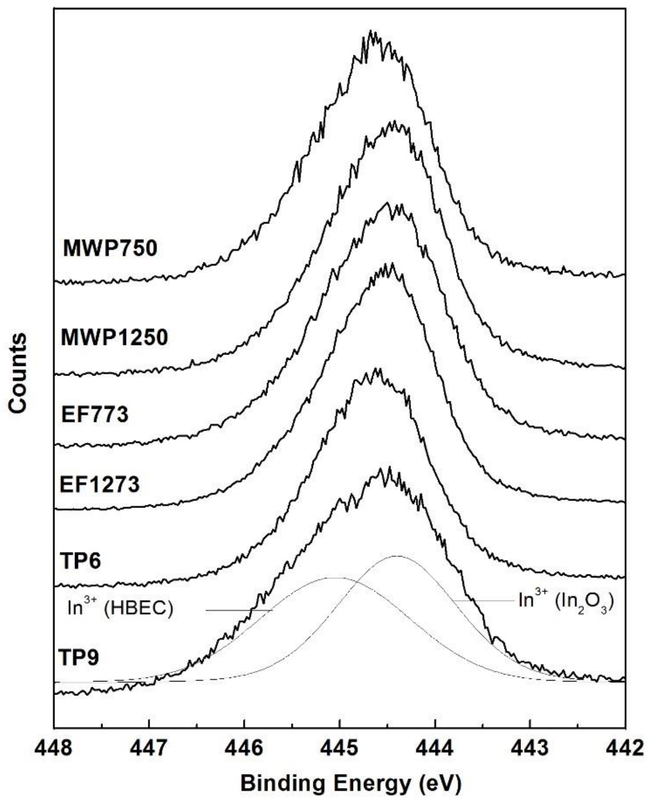

**Fig. 2.11**. The fitted peaks of In3d5/2 curves

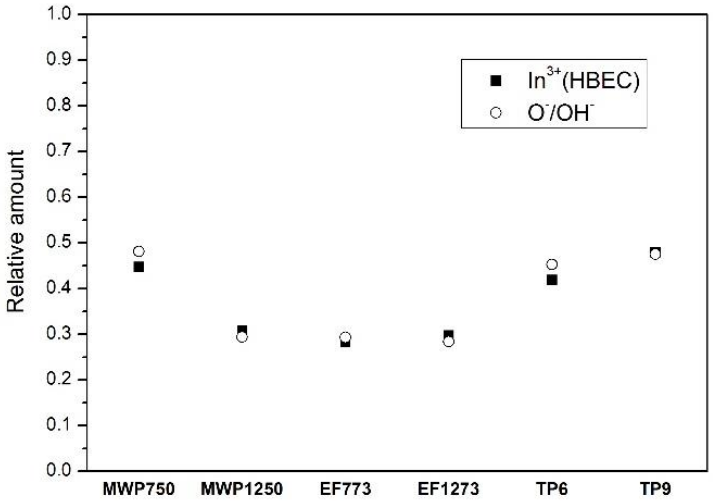

**Fig. 2.12**. Comparison of the ratios of $In^{3+}$(HBEC) in In3d and $O^-/OH^-$ in O1s

## 2.3.2. Morphologies of the prepared powder

The morphologies of the MWPs and the EFs that were regarded as the products of the solid-state reaction were observed with electron microscopes. Fig. 2.13 shows the SEM and FE-SEM images of the raw material, the MWPs and the EFs with magnification levels of x5.0k and x30.0k, respectively. $In(OH)_3$ originally had a hexahedral morphology with a smooth surface, and the size of each particle ranged from 1 μm to 5 μm. After the dehydration using microwave plasma, both the macro-morphology and the micro-morphology of the raw material were maintained. The MWPs still had hexahedral morphologies and smooth surfaces with few cracks. In addition, a few nano-sized particles were observed on the surface of the products, which were formed by the vaporization of the dehydrated particles as the microwave power increased. In the case of the EFs, the macro-morphology was maintained but the micro-morphology changed. As shown in Fig. 2.13, the EFs had rough and cracked surfaces.

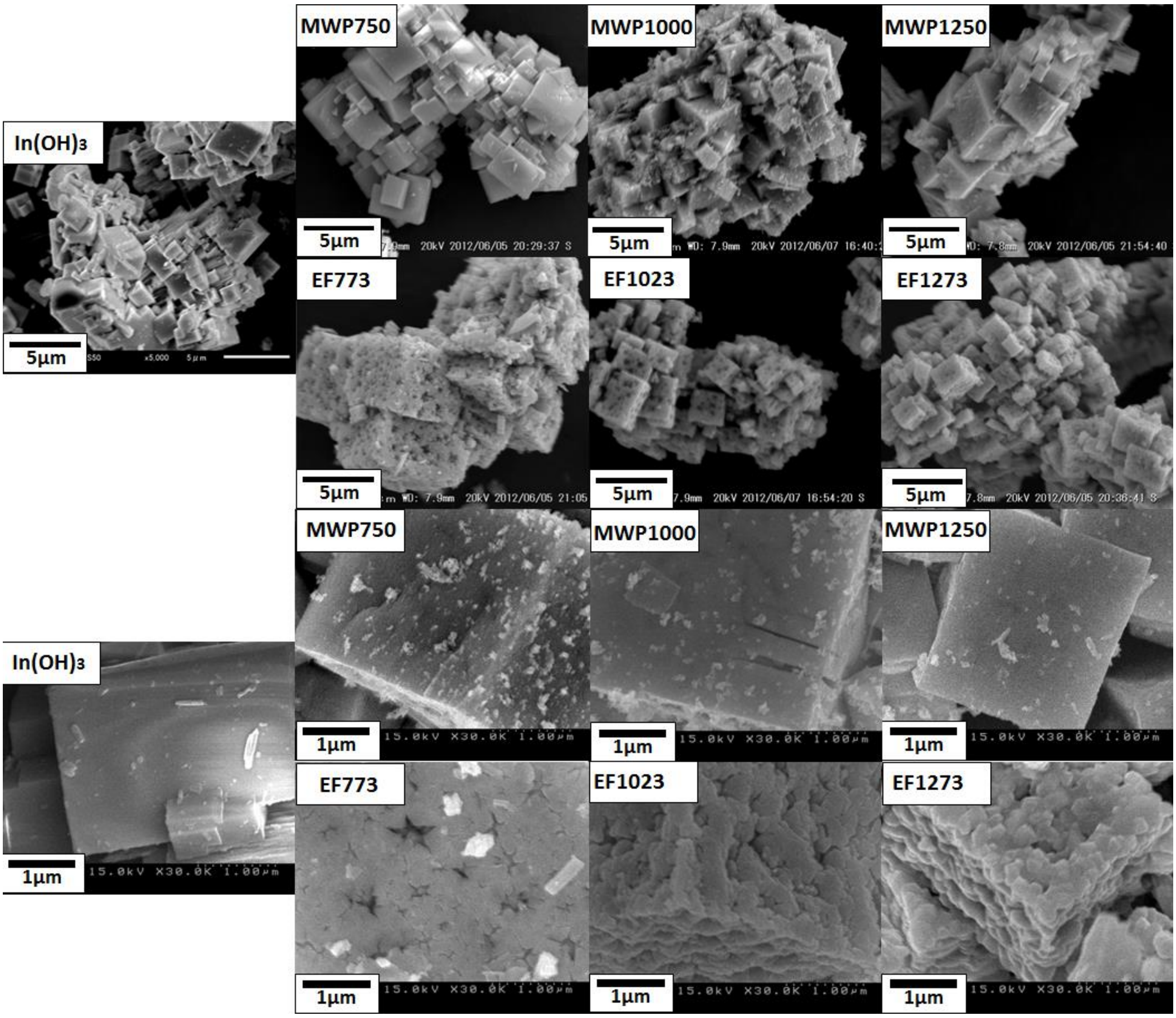

**Fig. 2.13**. SEM (upper) and FE-SEM (lower) images of $In(OH)_3$ and the products obtained from the microwave plasma and the electric furnace

The morphologies of the TPs are also shown in Fig. 2.14. Both the TP6 and TP9 that were smaller than 50 nm agglomerated with each other. In the thermal plasma, the injected $In(OH)_3$ was dehydrated once, but the anhydride ($In_2O_3$) still remained in the high-temperature region, wherein the temperature was higher than the boiling point of $In_2O_3$, and then vaporized fast. The vaporized component nucleated as $In_2O_3$, which was the most stable phase. Here, the fast cooling rate controlled the growth of the $In_2O_3$ nucleus, and then the nanoparticles were obtained. When the TP6 and TP9 were observed with low magnification, the TP6 was found to have been composed of particles that were bigger than tens of micrometers, and their surface was observed to have been covered with nanoparticles. $In_2O_3$ may be considered to be incompletely vaporized with 6kW argon thermal plasma. On the other hand, the TP9 was totally composed of nanoparticles due to its complete vaporization.

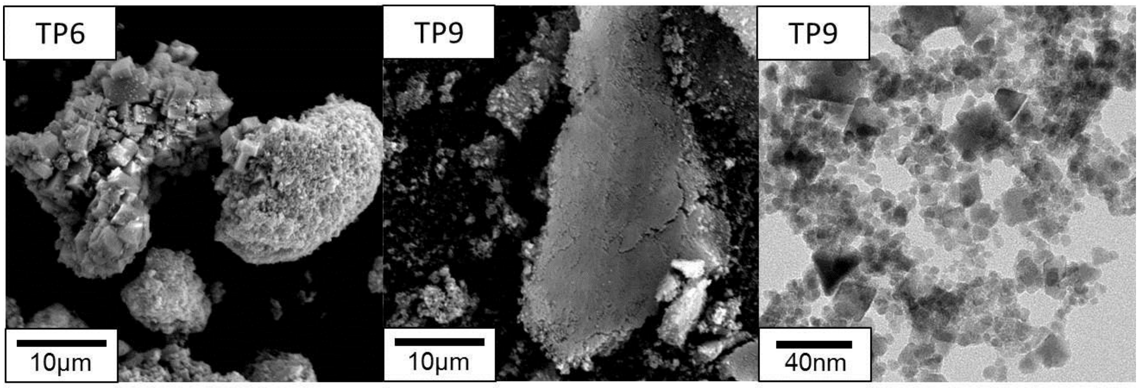

**Fig. 2.14**. SEM and TEM images of TP6 and TP9

### 2.3.3. Formation phenomena of $In_2O_3$

From the previous sections, it is known that the MWPs have the similar chemical composition but the different surface state with the EFs; the smooth surface of $In(OH)_3$ was remained by dehydration using the microwave plasma but not the electric furnace.

The formation of those cracks in the EFs is believed to have been determined by the diffusion rate of the dissociated water. The removal of the vapor-phase product in the lattice is the most important step in the determination of the micro-morphology in the solid-state reaction with degassing.

The vapor product in lattices is removed in two steps: the chemical step and the diffusion step. First, the vapor product is dissociated from the lattices in the chemical step, and then the dissociated vapor is diffused through the gap between the lattices, called the ‘molecular dimensioned capillary’ [58]. In the study of Okhotnikov et al. [59], the product of the diffusion-step-dominated dehydration had a smooth surface, whereas the product of the chemical-step-dominated dehydration had many cracks. The most possible cause of the formation of those cracks is the bursting of the vapors between the lattices due to their vapor pressure. When the diffusion is limited and the chemical step is fast enough, the dissociated vapors are confined between the lattices and then burst and form cracks. In contrast, when the diffusion is fast enough, the vapor can be removed with only a gap between the lattices, in which case the micro-morphology will be maintained.

Applying this results obtained here, the MWPs could be considered to have been prepared with the diffusion-step-dominated dehydration, and the EFs, with the chemical-step-dominated dehydration. The temperature and the heating rate are the major factors that determine the diffusion rate. As the temperature of the microwave plasma was much higher than that of the electric furnace, the diffusion rate in the microwave plasma also became much higher than that in the electric furnace. Another factor affecting the diffusion rate is the heating rate. Masuda et al. [60] reported that the crystallinity of the product is correlated with the presence of the dissociated water molecule. The dissociated water molecules may easily bond with this indium atom in the amorphous phase or the transition state, which will decrease the net diffusion rate. Additionally, these re-adsorbed water molecules make the diffusion path narrow, which negatively influence the molecular diffusion. Hence the diffusion of the dissociated water molecule may be disturbed in the amorphous phase. Fig. 2.15 shows a scheme of the dehydration in both the microwave plasma and the electric furnace. In the microwave plasma, the dehydration and the crystallization could have occurred almost simultaneously and could have increased the diffusion rate because the heating rate was fast enough. On the other hand, the diffusion wasn't enough because much of the dehydration was performed during the amorphous phase in the electric furnace. From the as-mentioned discussion, the high temperature and the fast heating rate of the microwave plasma were considered to promote the diffusion of the dissociated water and have an important role to keep the smooth surface.

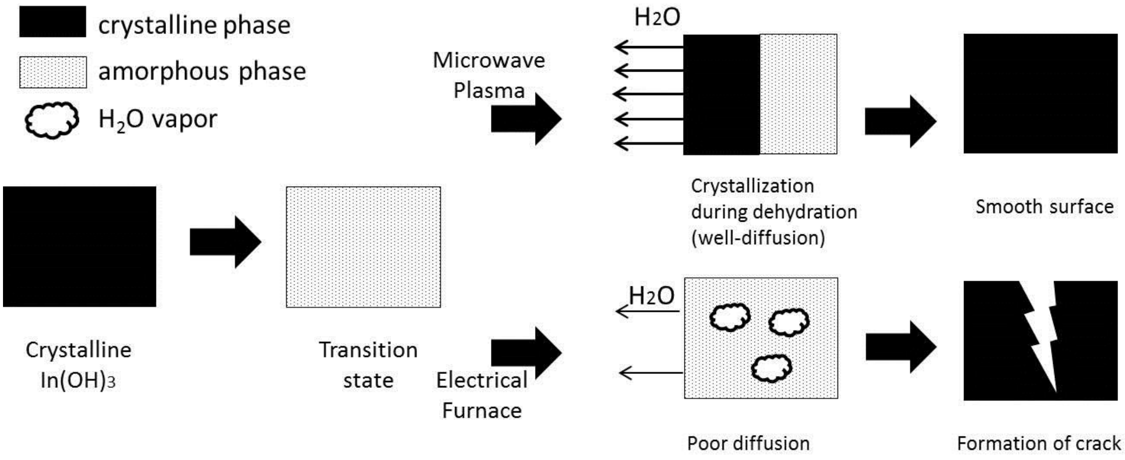

**Fig. 2.15**. The dehydration scheme in macro scale

In this chapter, the atmospheric pressure microwave plasma enabled the dehydration of the particle without both the morphology change and the evaporation. Although only the dehydration was tried in this thesis, the proposed mechanism suggests that this method has a possibility for general degassing reaction of the particle to obtain the original morphology.

## 2.4. Summary

The dehydration of $In(OH)_3$ was attempted as a model reaction of the particle preparation from the solid particle precursor using microwave plasma. Due to limitations of the microwave plasma temperature, $In(OH)_3$ injected into the plasma region didn’t evaporate but was only dehydrated to transform $In_2O_3$.

Comparison of the results by the microwave plasma with those by the thermal plasma and the electric furnace implied the specific reaction by the microwave plasma. The product of the microwave plasma had a smooth surface, whereas that of the electric furnace had a cracked and rough surface due to the bursting of the water vapor between the lattices since the diffusion of the dissociated water was poor due to the relatively low temperature and heating rate. In the DC thermal plasma, $In(OH)_3$ was evaporated and formed $In_2O_3$ nanoparticles by the vapor phase reaction.

The results of this chapter suggested that the rapid heating rate and the moderate temperature not to evaporate precursor of the atmospheric pressure microwave plasma enable dehydration of the solid particle precursor with maintaining the original surface state. It was quite different from those of the DC thermal plasma and those of the electric furnace.

## Chapter 3

# Synthesis of iron oxide-silica composite nanoparticles

## 3.1. Introduction

### 3.1.1. Iron oxide and iron oxide-silica composite particles

Magnetic materials have been widely applied to magnetic fluids [61, 62], data storage [63], biochemical applications (e. g. magnetic resonance imaging [64, 65], drug delivery [66]) and environmental remediation [67]. Among numerous magnetic materials, iron oxides are attracting considerable interest.

Although there are various iron oxide phases such as FeO, $\alpha$-$Fe_2O_3$, $\beta$-$Fe_2O_3$, $\gamma$-$Fe_2O_3$, $\varepsilon$-$Fe_2O_3$ and $Fe_3O_4$, the frequently mentioned phases are $\alpha$-$Fe_2O_3$, $\gamma$-$Fe_2O_3$ and $Fe_3O_4$; $\alpha$-$Fe_2O_3$ also called hematite having antiferromagnetic or ferromagnetic property is stable at low temperature region, $\gamma$-$Fe_2O_3$ also called maghemite is metastable phase, $Fe_3O_4$ also called magnetite is stable at high temperature.

$Fe_3O_4$ and $\gamma$-$Fe_2O_3$ have cubic spinel structure in common. However, $\gamma$-$Fe_2O_3$ has cation vacancy as written as $(Fe)(Fe_{5/3}\square_{1/3})O_4$ while $Fe_3O_4$ has fully packed spinel structure. Because $Fe_3O_4$ and $\gamma$-$Fe_2O_3$ exhibit superparamagnetic properties with particle size below 100nm, the synthesis of those nanoparticles have been continuously attempted [68-76].

## 3.1.2. Iron oxide-silica composite particles

Biochemical applications of iron oxide have been actively studied in recent years [77]. However, pure iron oxides cannot be applied because of large agglomeration, change of the magnetic properties and degradation in biological systems. Therefore, many researchers have studied inert material coated iron oxides or iron oxide/inert material composites [78-80] as favorable candidates to solve those problems. Coating inert material, especially silica on iron oxide provides enhanced colloidal stability and increased chemical resistance while keeping the original magnetic property.

Various methods have been researched to prepare coated iron oxide particles which include carbon/iron oxide [81-84], ceramic/iron oxide [85, 86] and metal/iron oxide [87, 88]. The preparation methods include liquid phase methods such as sol-gel, co-precipitation and controlled hydrolysis, in which additional processes have to be carried out to remove organic compounds used in the preparation process which limit their applications. Nevertheless it is hard to remove completely the organic compounds adsorbed on the products. To solve this problem, interest in employing a vapor phase method has grown [89-91]. As an alternative to a liquid phase method, vapor phase method leads to high purity products without post-treatment.

### 3.1.3. Particle preparation in multi-component system using plasma

For some decades, numerous researches frequently deal with multi-component particle such as doped ceramic, coated material and spinel ($AB_2O_4$) since their unique properties have attracted large interest in the application field [92-94]. Compared to the single-component system, multi-component system would lead to the formation of more various products by altering the experimental conditions (e.g. ratio of components, injection method). However the particle generation phenomena were not yet explained due to difficulties in predicting behaviors of various chemical species in the high temperature region. To prepare the desirable multi-composite particles from plasma processing, further understanding of the multi-component system in the plasma is required.

### 3.1.4. Purpose of this chapter

The researches of this chapter are performed with two purposes; one is to investigate the particle formation mechanism from the gaseous precursor in the atmospheric pressure microwave plasma. Another is to find out the effective factor to determine the final product in the plasma. As a model reaction, the synthesis of nanoparticles from Fe-Si-O multi-component system obtained from the decomposition of iron pentacarbonyl [$Fe(CO)_5$] and tetraethyl orthosilicate [$(C_2H_5O)_4Si$), known as TEOS] were performed. The results were compared with those by the DC thermal plasma. The particle formation mechanism was proposed from the observation of the particle morphologies and the phase compositions.

## 3.2. Experiments

### 3.2.1. Experimental apparatus

### Microwave plasma

Fig. 3.1 and Fig. 3.2 show the experimental apparatus of the atmospheric pressure microwave plasma. Prior to mention the difference between Fig. 3.1 and Fig.3.2, the common experimental apparatus is explained.

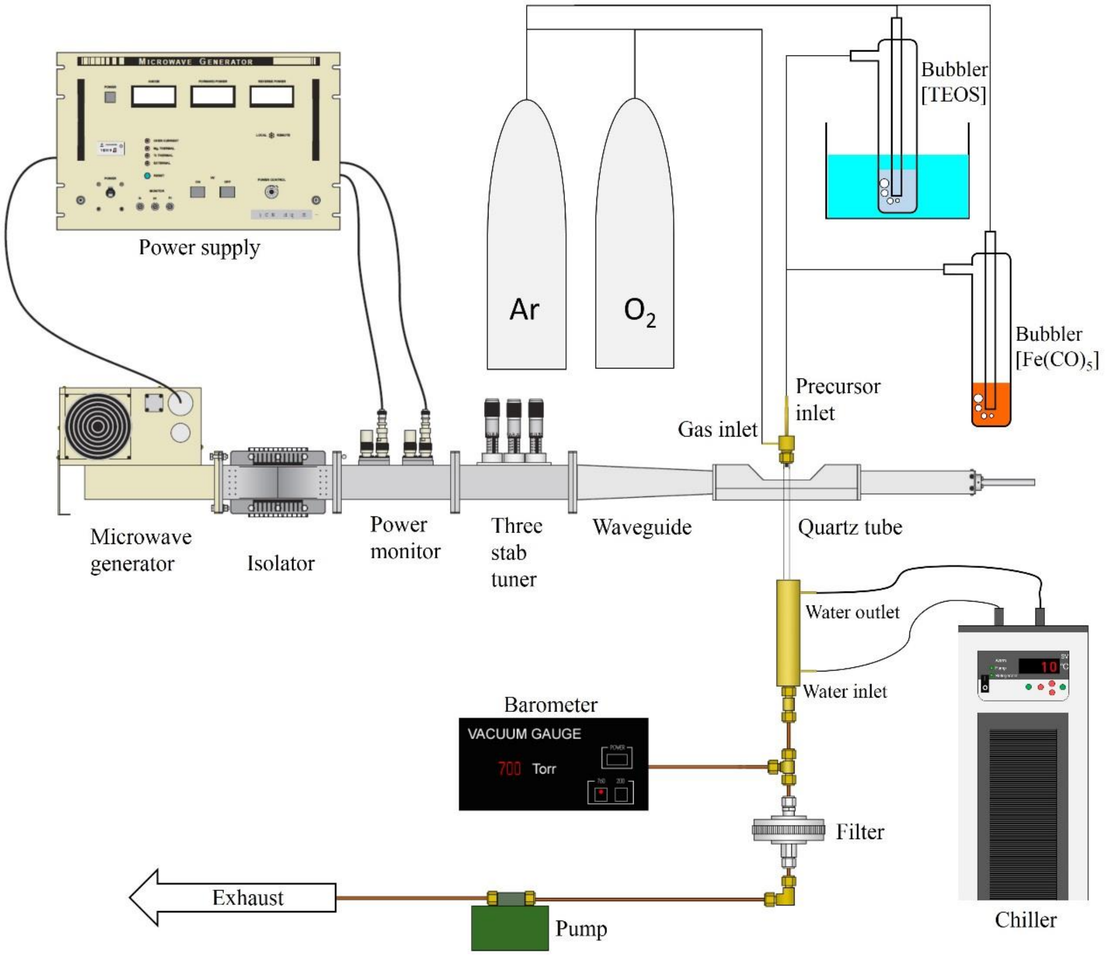

**Fig. 3.1**. Experimental apparatus for axial injection of precursors

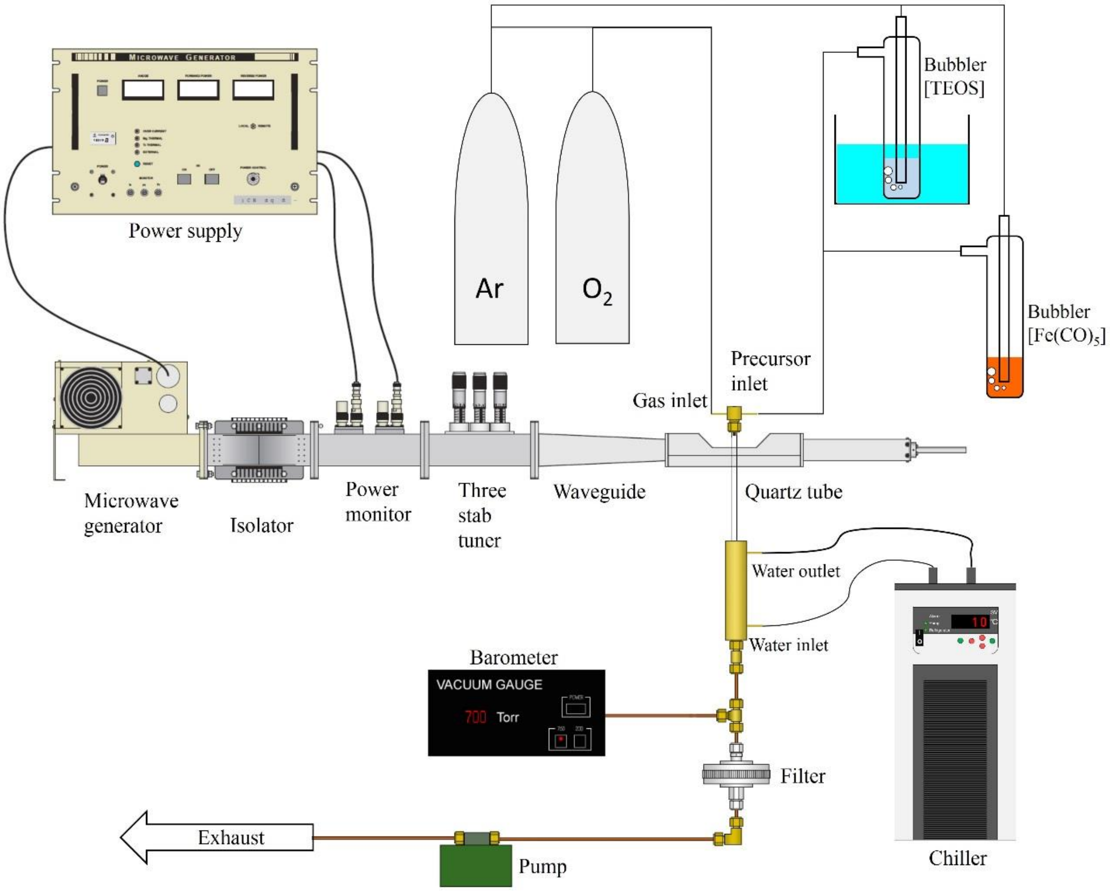

**Fig. 3.2**. Experimental apparatus for swirl injection of precursors

The generation part of the plasma is the same with that described in the previous chapter. However difference is that the mixture gas of argon and oxygen was used as a discharge gas. Therefore, the three stab tuner was adjusted to make reflection power close to zero under Ar-$O_2$ atmosphere.

The vapor of the precursors, $Fe(CO)_5$ and TEOS which are liquid at room temperature were bubbled and then carried by argon gas. As one of the operating variables, the ratio of Fe to Si in the feeding flow was controlled by varying the vapor pressure of each precursor. The vapor pressures were calculated by Antoine equation as follows;

$$log_{10}(P) = A - \frac{B}{T+C} \qquad (3.1)$$

where $P$ is vapor pressure (bar), $T$ is absolute temperature (K), $A$, $B$, and $C$ are Antoine equation parameters depending on the material. Antoine equation parameters of $Fe(CO)_5$ and TEOS and the available temperature ranges are listed in Table 3.1 [95].

**Table 3.1**. Antoine equation parameters of $Fe(CO)_5$ and TEOS

| | Temperature(K) | A | B | C |
|---|---|---|---|---|
| $Fe(CO)_5$ | 266.7~378 | 5.18943 | 1960.896 | -0.228 |
| TEOS | 289~441.7 | 4.17312 | 1561.277 | -67.572 |

The injection rates of the precursors were determined by the combination of the carrier gas flow rate and the bubbling temperature. The injection rates of the precursors are calculated as follows;

$$Injection\ rate\ [ml/min] = \frac{P[bar]}{1.01325\ [bar/atm]} \times carrer\ gas\ flow\ rate\ [ml/min]$$

The bubbling conditions of the precursors are summarized in Table 3.2. During all of the experiments, the bubbler filled with $Fe(CO)_5$ was exposed to the atmosphere at room temperature (298 K), while that with the TEOS was put in the water bath to change the vapor pressure of TEOS. The experiments with only $Fe(CO)_5$ or TEOS were performed to synthesis pure iron oxide and pure silica for comparison.

**Table 3.2**. Bubbling conditions of $Fe(CO)_5$ and TEOS

| | Temperature (K) | Carrier gas (Ar, ml/min) | Injection rate (ml/min) | Fe/Si |
|---|---|---|---|---|
| $Fe(CO)_5$ | 298 | 300 | 9 | 3 |
| TEOS | 323 | 300 | 3 | |
| $Fe(CO)_5$ | 298 | 200 | 6 | 1 |
| TEOS | 323 | 600 | 6 | |
| $Fe(CO)_5$ | 298 | 100 | 3 | 0.33 |
| TEOS | 333 | 500 | 9 | |
| $Fe(CO)_5$ | 298 | 400 | 12 | - |
| TEOS | - | | | |
| $Fe(CO)_5$ | - | | | - |
| TEOS | 323 | 1000 | 11 | |

The injecting line connected to the injection block shown in Chapter 2 was heated by a ribbon heater to prevent saturation of the vaporized precursors. The specification of the used quartz tube was the same as that used in Chapter 2 (i.d. : 9mm, o.d. : 11mm, length : 350mm). The end of the quartz tube was fixed to the double walled water cooling tube.

For plasma generation, the pure argon plasma with filament discharge was generated first and then the addition of oxygen led to the formation of the $Ar-O_2$ mixture plasma jet having blue-white color. The operating conditions of the plasma are summarized in Table 3.3.

**Table 3.3**. Operating conditions of atmospheric pressure microwave plasma

| Power | | 900W |
|---|---|---|
| Pressure | | 700~750 torr |
| Flow rate of discharge gas | Ar | 9 L/min |
| | $O_2$ | 1 L/min |

The experimental sequences are summarized as following;

1) The water bath was operated and heats until the target temperature.

2) The microwave argon plasma was generated by applying high frequency.

3) The oxygen flow was added to the plasma flow.

4) The feed flow was injected into the plasma.

5) The reaction was performed during 10minutes.

6) The synthesized particles were collected from the filter.

Once the precursors were being injected, the plasma glowed orange induced by excitation of iron atoms. The pictures of the plasma with shutter speed of 0.001 s before and after the precursor injection are shown in Fig. 3.3.

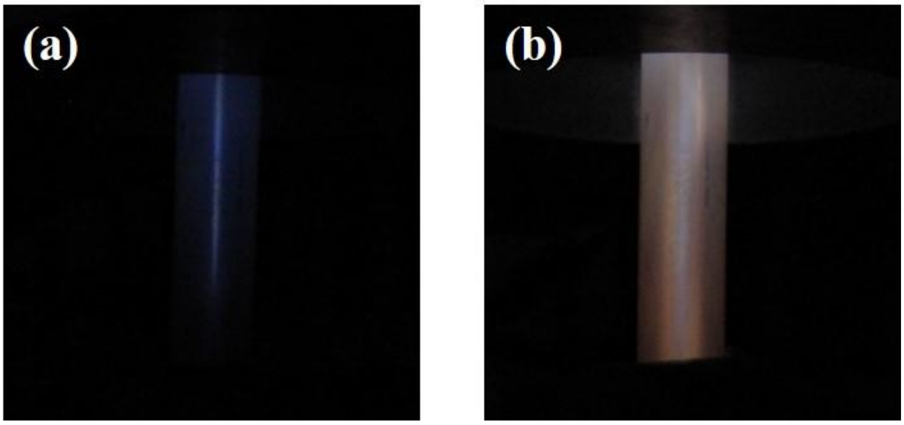

Fig. 3.3. Ar-$O_2$microwave plasma (a) before and (b) after precursor injection

The two types of apparatus were used for the experiments.

The apparatus shown in Fig. 3.1 is to inject the precursors parallel to the quartz tube axis, which is called ‘axial injection’ in this thesis. Axial injection makes the precursors carried to the discharged region having close to the maximum temperature.

The apparatus shown in Fig. 3.2 is to inject tangentially the precursors flow through the nozzle positioned symmetrically to the nozzle to inject the discharge gas, which is called ‘swirl injection’ in this thesis. With swirl injection, the precursors flowed the inner wall of the quartz tube like as ‘vortex’, which made the precursors pass through the lower temperature region.

The experiments are listed in Table 3.4.

**Table 3.4**. List of experiments and samples for microwave plasma

| Samples | Apparatus | Fe/Si | Precursor injection |
|---|---|---|---|
| MWP3 | Fig. 3.1 | 3 | Axial |
| MWP1 | Fig. 3.1 | 1 | Axial |
| MWP033 | Fig. 3.1 | 0.33 | Axial |
| MWPFe | Fig. 3.1 | Only Fe | Axial |
| MWPSi | Fig. 3.1 | Only Si | Axial |
| MWP3_S | Fig. 3.2 | 3 | Swirl |

## DC thermal plasma

Fig. 3.4 shows the experimental apparatus using the DC thermal plasma. The plasma generation system was the same as that in the previous chapter, but the reactor was changed. The precursors were injected through the nozzle located at a distance of 5 mm from the plasma jet exit. The operating conditions of the DC thermal plasma is summarized in Table 3.5.

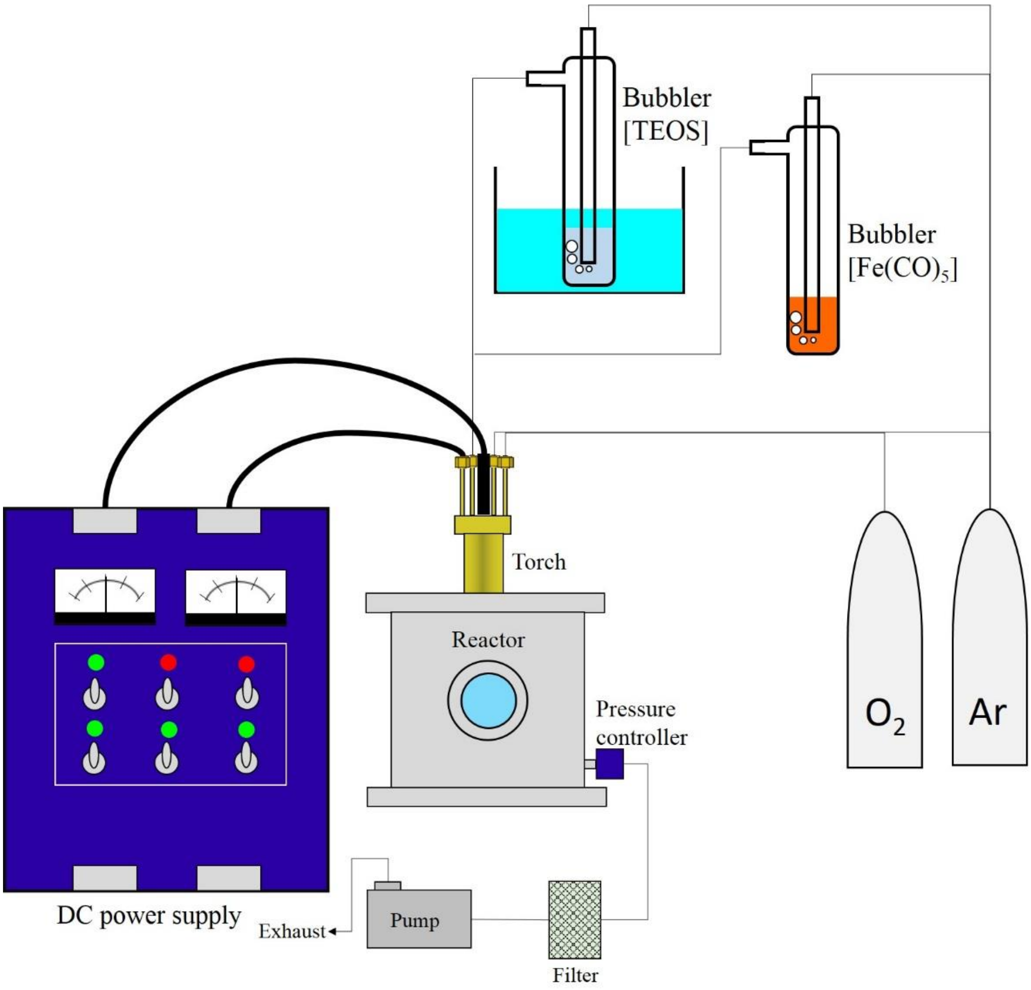

**Fig. 3.4**. Experimental apparatus using DC thermal plasma

**Table 3.5**. Operating conditions of DC thermal plasma

| | |
|---|---|
| Power | 7 kW (300 A, 25 V) |
| Pressure | 700~750 torr |
| Discharge gas | Ar : 10 L/min |
| Additional gas | $O_2$ : 1 L/min |

The experiments using the DC thermal plasma are listed in Table 3.6. Similarly the experiments using the microwave plasma, the ratio of Fe to Si was controlled.

**Table 3.6**. List of experiments and samples for DC thermal plasma

| Samples | Fe/Si |
|---|---|
| DCP3 | 3 |
| DCP1 | 1 |
| DCP033 | 0.33 |
| DCPFe | Only Fe |
| DCPSi | Only Si |

### 3.2.2. Characterization

The phase composition of the obtained particles was analyzed with an X-ray diffractometer (XRD, X’Pert-MPD-OEC, Philips) utilizing Cu Kα1 radiation with a wavelength of 1.540598Å. All samples were measured twice. At first, the scanned range of 2θ was from 20° to 80° with step size of 0.02° and time per step of 0.4 s/step. This measurement was to confirm the change of the phase composition. For the second time, the scanned range of 2θ was from 35° to 36.5° with step size of 0.01° and time per step of 5 s/step. The second measurement was to calculate lattice parameter as follows;

$$n\lambda = 2d\sin\theta \qquad (3.1)$$

$$a = \frac{d}{\sqrt{h^2+k^2+l^2}} \qquad (3.2)$$

Eq (3.1) is called Bragg’s equation where $n$ is an integer, $\lambda$ is X-ray wavelength (1.540598Å), $d$ is a lattice spacing and $\theta$ is half of 2θ at the peak. Eq (3.2) is to calculate a lattice parameter of a cubic unit cell from a lattice distance calculated from Eq (3.1) where $a$ is a lattice parameter and $h$, $k$, and $l$ are Miller indices of a corresponding plane.

The morphologies of the synthesized particles were observed by a transmission electron microscope (TEM, 2010F, JEOL) operating with the voltage of 200 kV.

The particles were dispersed in the isopropyl alcohol by ultrasound and then were sampled on the grid. The isopropyl alcohol was completely removed by drying the grid during some days.

## 3.3. Results and discussion

In this section, MWP3, MWP1 and MWP033 prepared by the microwave plasma with axial injection are considered as standard samples and then are compared with others. The comparison with DCP3, DCP1 and DCP033 is to investigate the difference by introducing the DC thermal plasma, with MWP3S is to investigate the effect of injection method. MWPFe, MWPSi, TPFe and TPSi were to refer the pure iron oxide and the pure silica.

This section is explained with the following step;

1) The morphologies of the products are shown and compared.
2) Phase composition of the products is analyzed and compared.
3) Thermodynamic consideration is introduced to explain the results.
4) The effect of each parameter is discussed from the combination of the results and the thermodynamic expectation.
5) The reaction model is proposed.

### 3.3.1. Morphologies of the synthesized particles

Prior to the explanation of TEM images, two points should be taken into consideration.

The first is that pure Fe or Fe-rich phase seems darker than pure Si or Si-rich phase in TEM image. Since Fe atom is heavier than Si atom, the transmittance of Fe atom against electron is lower than that of Si atom. It can be empirically expected that Fe or Si is easily oxidized under the presence of oxygen during vapor phase synthesis [96]. Therefore dark part is considered as pure iron oxide or iron oxide-rich phase.

The second is that amorphous phase is considered as pure silica or silica rich phase.

It is well-known that silica synthesized by thermal plasma has amorphous phase. Therefore the presence of the visible lattice in TEM images was an important factor to distinguish iron oxide and silica.

### a) MWPFe

As shown in Fig. 3.5, the pure iron oxide particles have polygonal morphologies as well as well-crystallized lattice structure. The particle size is ranged from below 5 nm to over 100 nm.

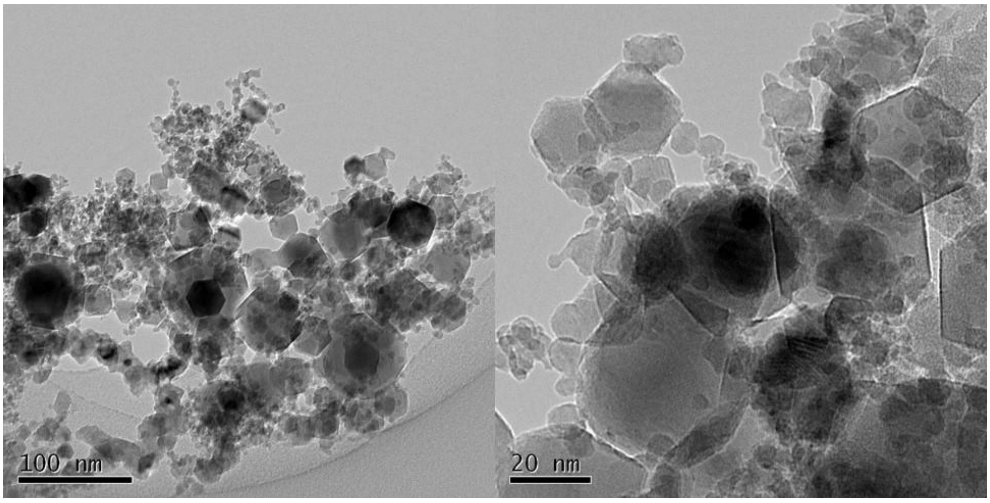

**Fig. 3.5**. TEM images of pure iron oxide prepared by microwave plasma

### b) MWPSi

As shown in Fig. 3.6, the pure silica particles have irregular morphologies and seems to be linked to each other. It is reported that silica nanoparticle made from TEOS by vapor phase reaction has the linked morphologies because $OH^-$ or $H_2O$ do a role to connect each particle after plasma region although silica particle sampled in the flame region was spherical. In our research, the irregular morphologies are expected as a contribution of $OH^-$ or $H_2O$ as reported [97]. Therefore this deformation of the silica particles somewhat limited the observation of the original structure of the silica-rich phase.

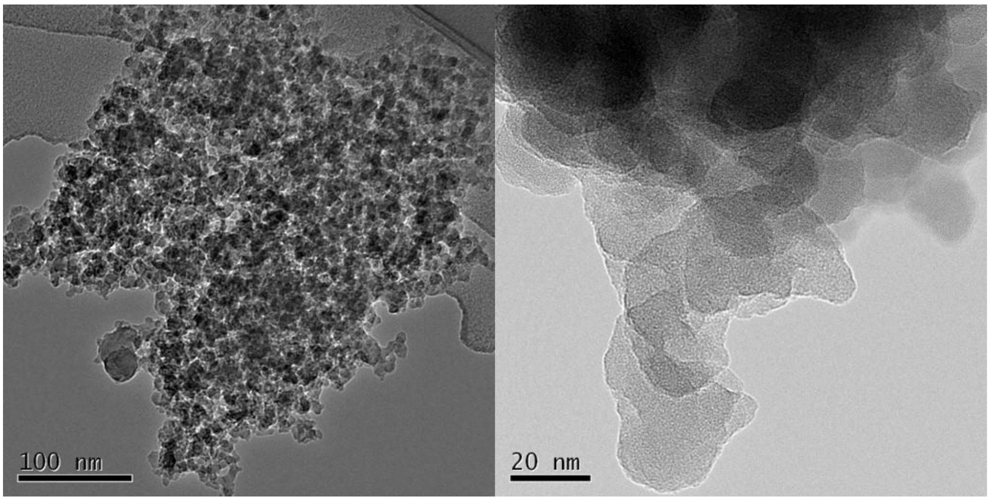

**Fig. 3.6**. TEM images of pure silica prepared by microwave plasma

### c) MWP3

Fig. 3.7 shows TEM images of MWP3 where broad particles size distribution from the particle below 5 nm to over 100 nm is observed. The some particles over 50 nm have the thin external layer with thickness of 1~2 nm. From the previous mention, this layer is expected as silica layer. This layer was not observed at the particles below 20 nm, but a small amount of silica particles attached to the crystalline iron oxide particles were observed. It is noted that MWP3, unlike pure iron oxide or pure silica, has many spherical particles.

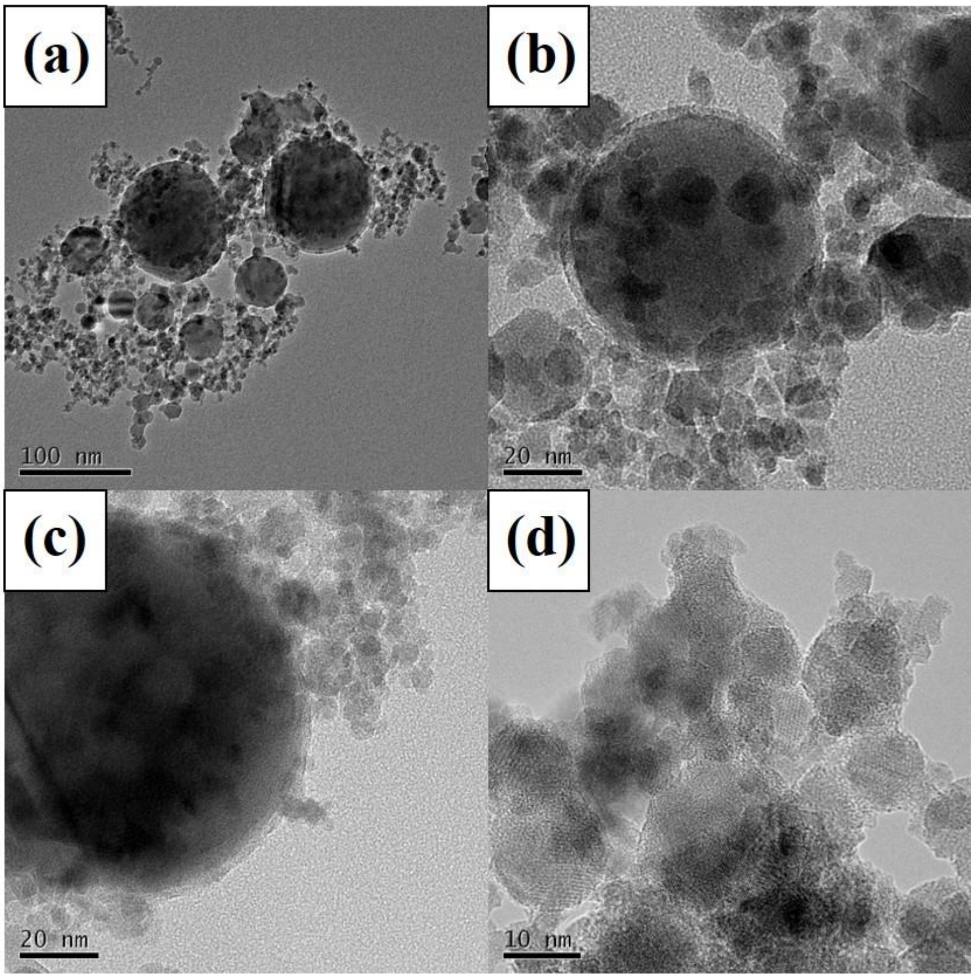

**Fig. 3.7**. TEM images of MWP3 with various magnification

### d) MWP1

Fig. 3.8 shows TEM images of MWP1 where broad particle size distribution is still observed as like as MWP3. The external layer is not observed, opposite to MWP3. Although most of the particles have spherical morphologies with the crystalline structure, some particles have irregular morphologies observed at the pure silica. It seems that the pure silica or the Si-rich phase are formed as the Fe/Si ratio decreased.

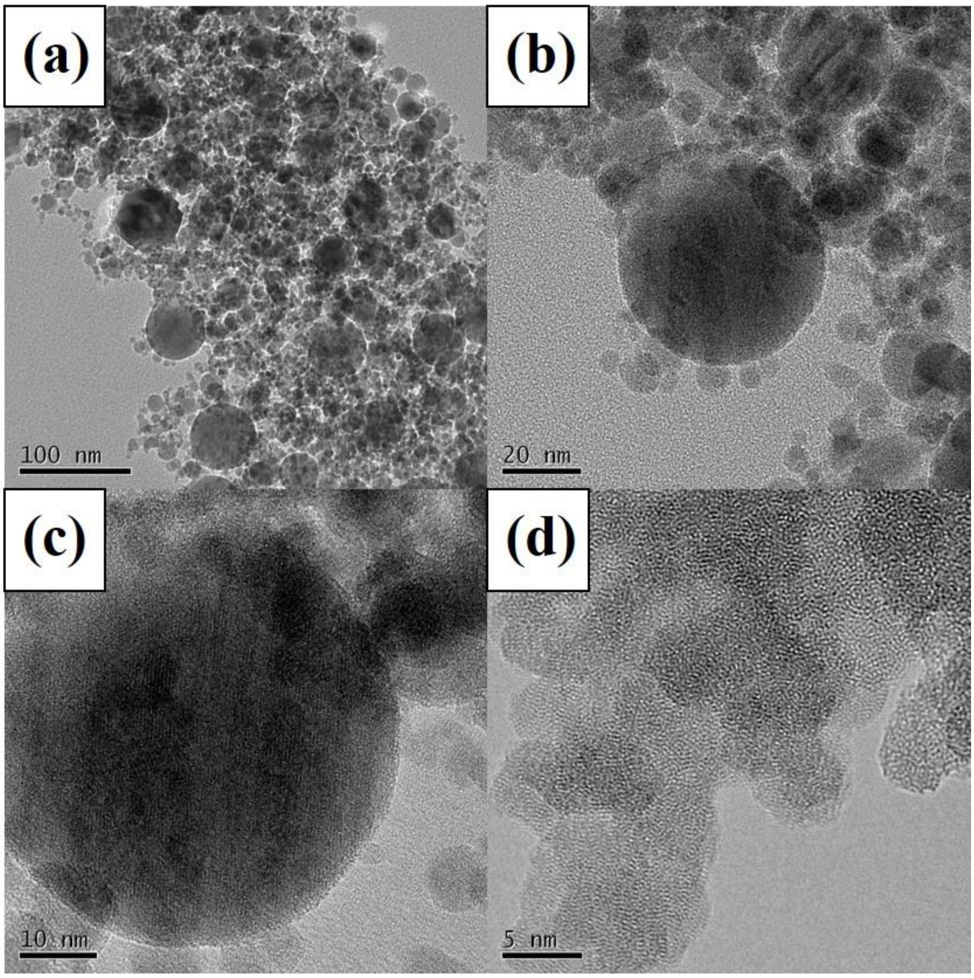

**Fig. 3.8**. TEM images of MWP1 with various magnification

### e) MWP033

Fig. 3.9 shows TEM images of MWP033. Likewise with MWP1, the particles do not have any clear external layer and mainly have spherical morphologies. Nevertheless the crystalline particles seem still considerable, showing the similar morphologies to MWP1 in spite of small ratio of Fe. Fig. 3.9 (d) shows that the crystalline parts indicated with red circles are located in the amorphous silica matrix. It implies that the silica and the iron oxide co-exist although it is difficult to distinguish one particle due to the deformation of the silica particle by as-mentioned reason.

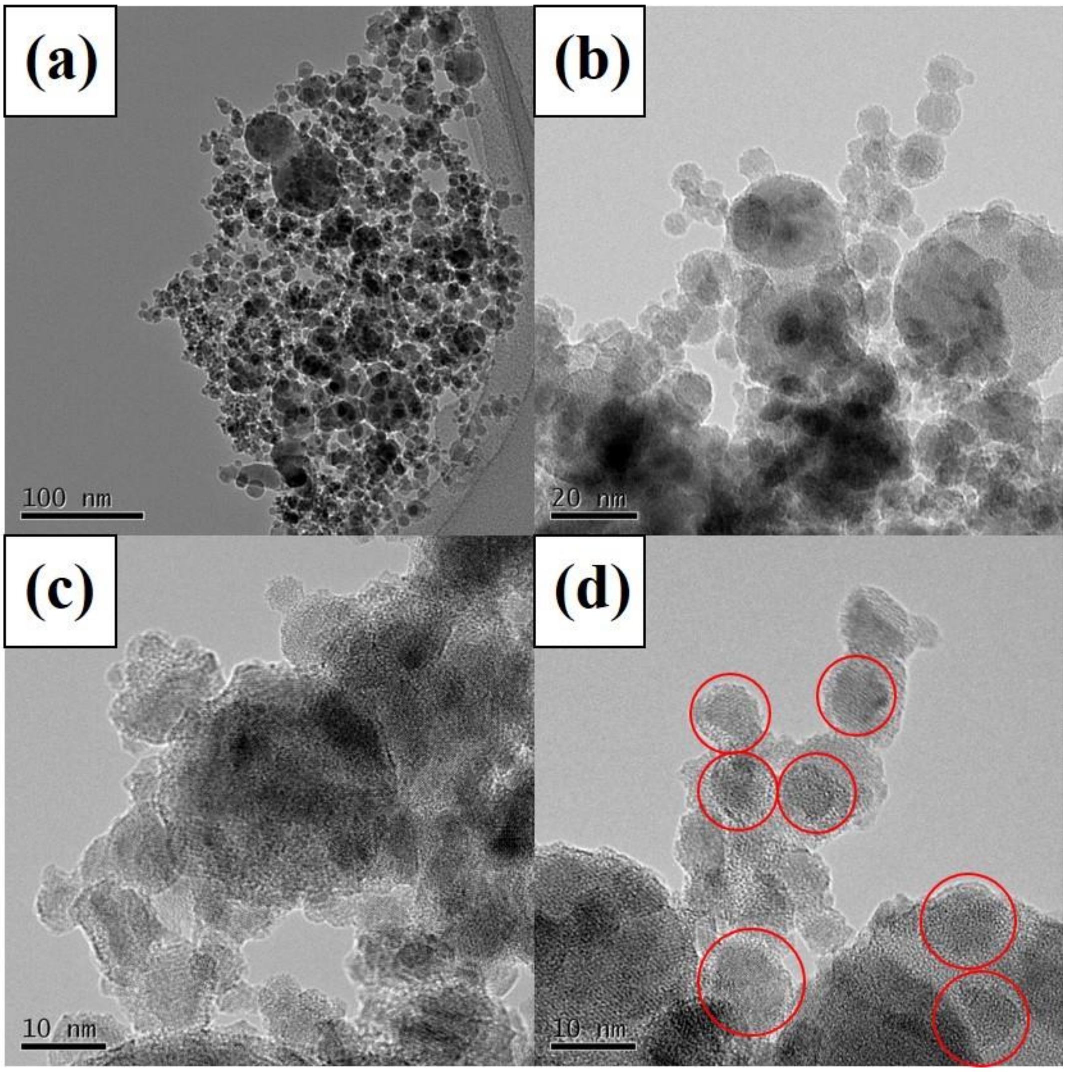

**Fig. 3.9**. TEM images of MWP033 with various magnifications

## f) DCPFe and DCPSi

The pure iron oxide and the pure silica prepared by the DC thermal plasma are shown in Fig. 3.10 and Fig. 3.11, respectively. Although Fig. 3.10 shows some polygonal particles as shown in MWPFe, the number of those particles is less than that of MWPFe. Since the polygonal iron oxide is considered as a result of crystallization, MWPFe has high crystallinity than DCPFe.

DCPSi shown in Fig. 3.11 seems similar to MWPSi.

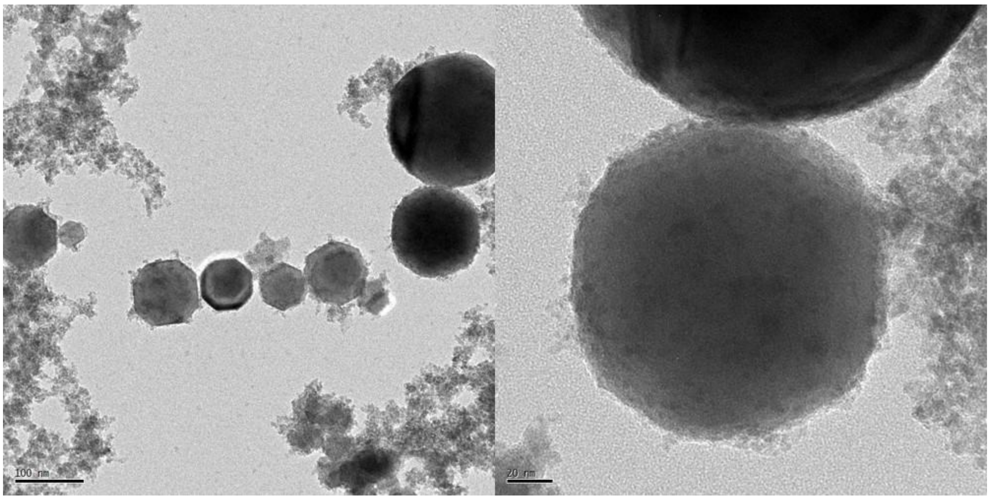

**Fig. 3.10**. TEM images of pure iron oxide prepared by DC thermal plasma

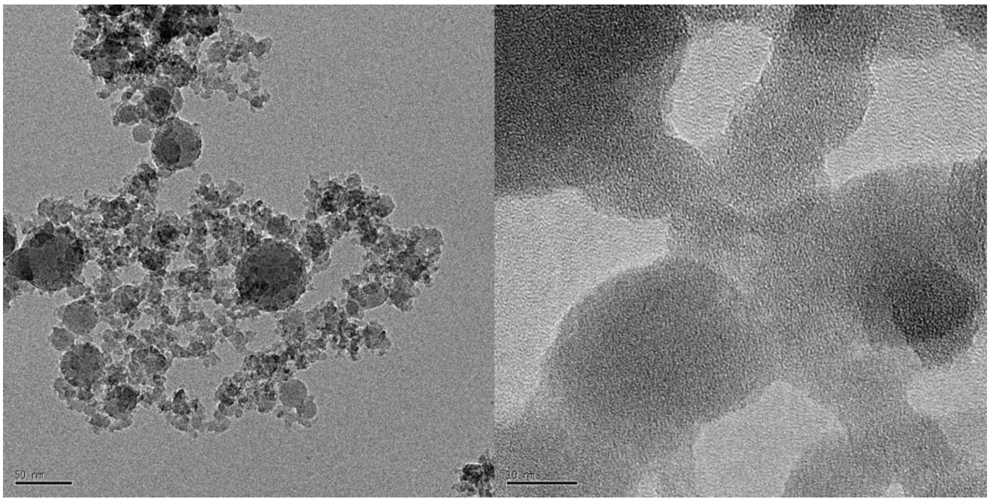

**Fig. 3.11**. TEM images of pure iron oxide prepared by DC thermal plasma

## g) DCP3

DCP3 consists of large spherical particles over 100 nm and small particles below than that. The large particles have an amorphous external layer as like as MWP3. However there are two obvious differences; one is that the thickness of the external layer is thicker than that of MWP3, another is that most of the large particles were coated while only some particles were coated in case of MWP3. The large particles shown in the following Fig. 3.13 demonstrate that. The small particles seem to have similar morphologies with those of MWP3.

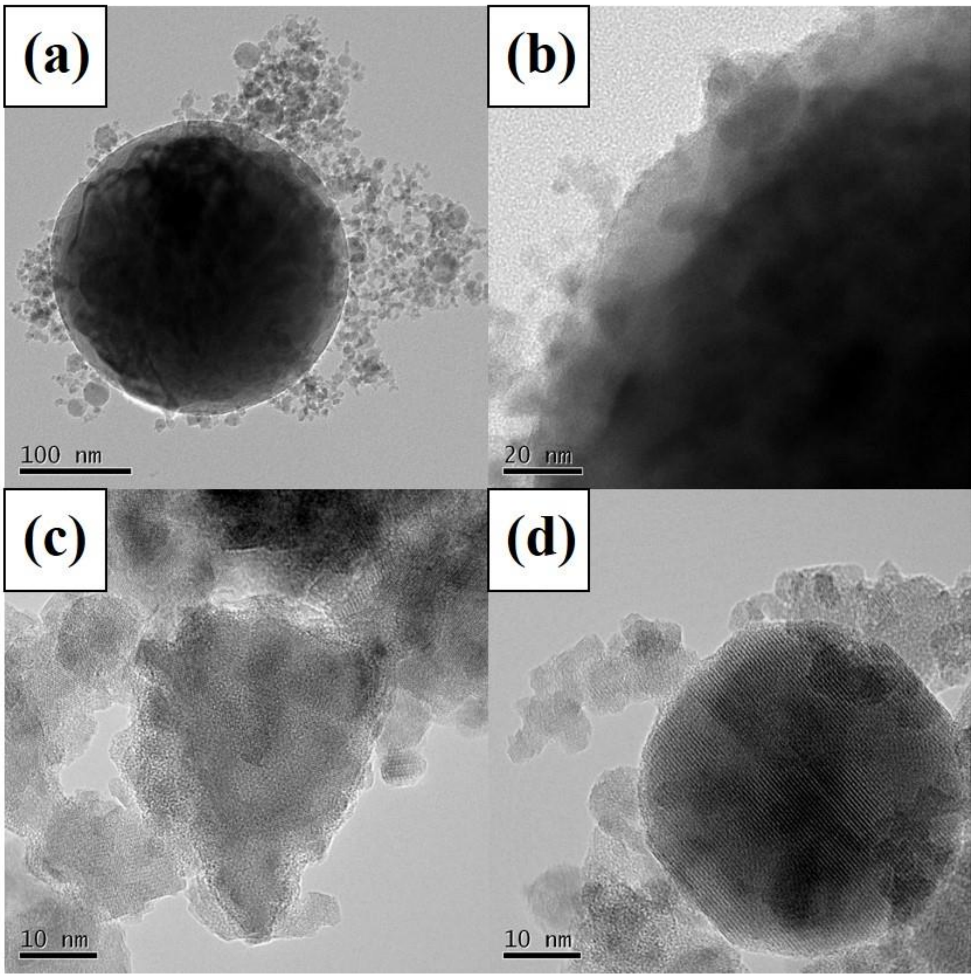

**Fig. 3.12**. TEM images of DCP3 with various magnification

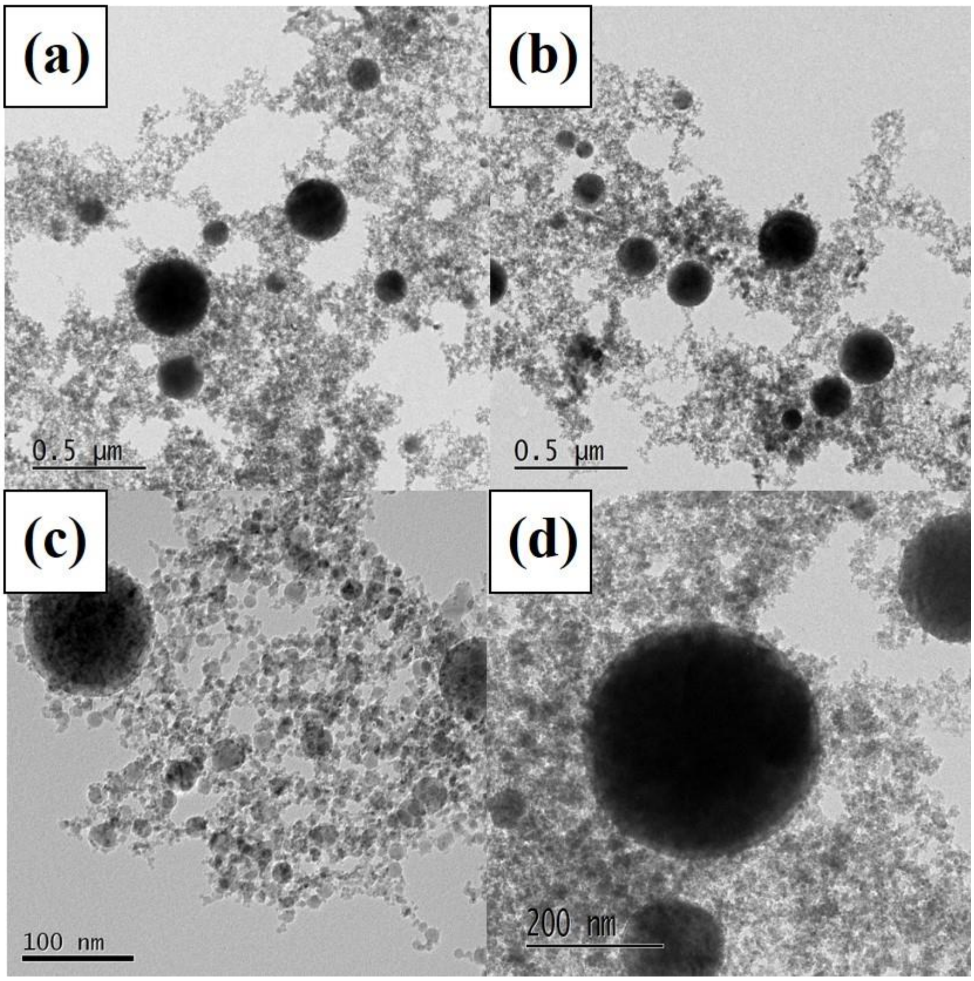

**Fig. 3.13**. TEM images of large particles coated by silica in DCP3

## h) DCP1

DCP1 has different morphologies from MWP3, MWP1, MWP033 and DCP3. In Fig. 3.14 (a) and (b), it seems similar with the pure silica. When observed with high magnification as shown in Fig. 3.14 (c), dark spots expected as iron oxide are observed. Fig. 3.14 (d) shows that those spots have crystal lattice. Therefore it seems that small crystalline particles are distributed in the amorphous matrix. Actually it seems similar with MWP1, however the size of the crystalline part is smaller than that of MWP1.

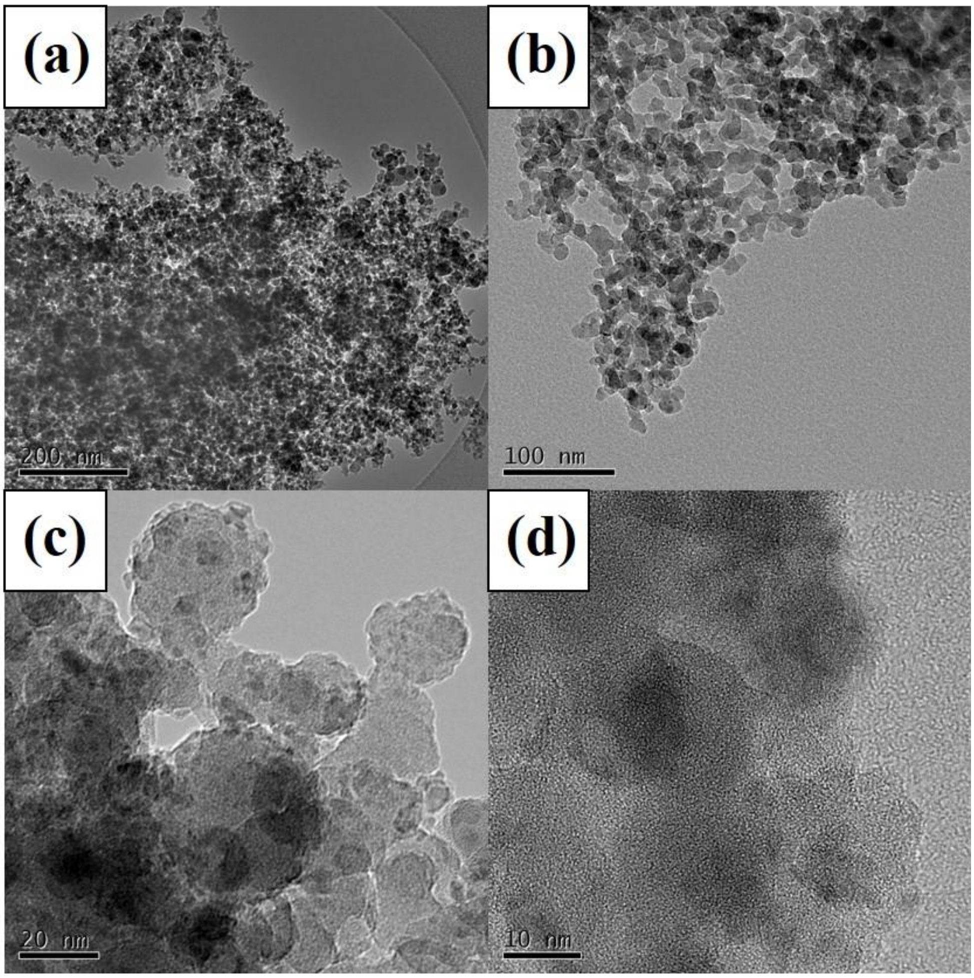

**Fig. 3.14**. TEM images of DCP1 with various magnification

### i) DCP033

DCP033 has almost the same morphologies with DCP1 having the linked morphologies of the silica and the small iron oxide spot. It seems almost the same as DCP1. However the amount of crystalline particles is less than that of DCP1. It should be focused on that MWP1 and MWP033 have similar morphologies while MWP3 has a different morphology from those.

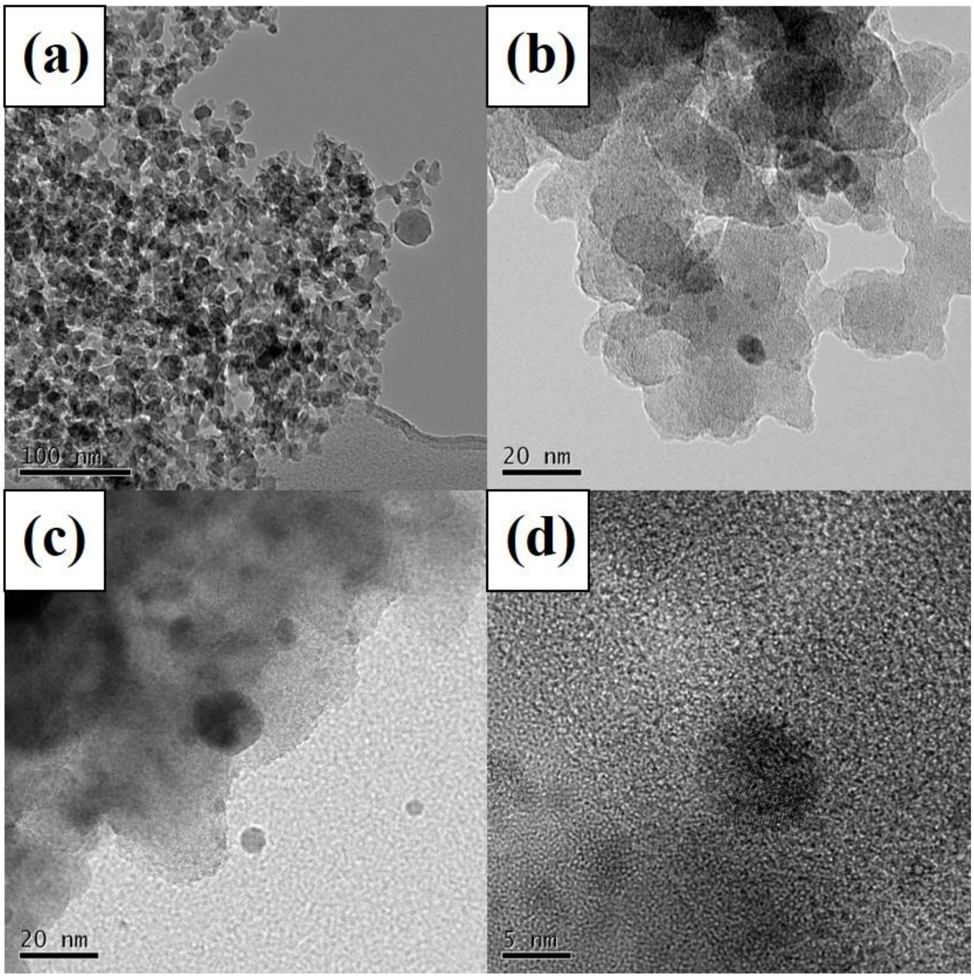

**Fig. 3.15**. TEM images of DCP033 with various magnification

The results of TEM analysis are summarized in Table 3.7.

**Table 3.7**. Summarization of morphologies of the particles observed by TEM

| | Description |
|---|---|
| MWPFe | Polygonal crystalline particles |
| MWPSi | Amorphous particles with irregular morphologies linked each other |
| MWP3 | Crystalline spherical particles but some of those have a thin amorphous external layer with thickness below 2nm. |
| MWP1 | Separation of crystalline phase and amorphous phase are observed but most of the particles are spherical and have crystalline phase. |
| MWP033 | Crystalline phase and amorphous phase co-exist in a particle |
| DCPFe | Polygonal crystalline particles |
| DCPSi | Amorphous particles with irregular morphologies linked each other |
| DCP3 | Crystalline spherical core and amorphous external layer with thickness over several nm |
| DCP1 | Small crystalline particles are distributed in the amorphous matrix. |
| DCP033 | Small crystalline particles are distributed in the amorphous matrix but the amount of crystalline particles is less than that of DCP1. |

### 3.3.2. Chemical composition

Prior to the discussion with the XRD results, it should be considered that only the crystalline phase could be qualitative analyzed by XRD. Although many amorphous site was observed in the TEM images, the amorphous phase just shows the broad peak around 25°. What contributes the most to those amorphous peak may be the amorphous silica. It is well-known that the plasma synthesized silica used to be amorphous because of the quenching process. In contrast, the crystalline phase may be almost the iron oxide or iron oxide-related phase which is focused on during the following discussion.

The XRD patterns of MWP3, MWP1, MWP033, DCP3, DCP1, DCP0333 and the reference patterns of $\gamma$-$Fe_2O_3$, $Fe_3O_4$ and $Fe_2SiO_4$ are shown in Fig. 3.16. Although broad peaks indicating amorphous phase are observed, the patterns having the maximum intensity around 36° are observed from the XRD patterns of MWP3, MWP1, MWP0333 and DCP3. Those patterns are close that of $\gamma$-$Fe_2O_3$ or $Fe_3O_4$ having have almost similar XRD patterns due to a similar structure as explained in *Introduction*.

These phase should be distinguished by calculating lattice parameter. Some researchers have reported how to distinguish these phase. Fortunately many of those researches deal with $\gamma$-$Fe_2O_3$, $Fe_3O_4$, $Fe_2SiO_4$ and these solid-solution due to importance of FeO-$SiO_2$ system which are main components of the Earth and the slag [98-101]. The lattice parameter are calculated by Eq (3.1) and Eq (3.2) because the peaks of the samples is considered to have the cubic unit cell. It is also noted that the lattice parameter of DCP1 and DCP033 could not be estimated due to the absence of any peak. The results of the calculation are summarized in Table 3.8. It is noted that the results of the second measurement mentioned in section 3.2.2 were used for the calculation of Table 3.8.

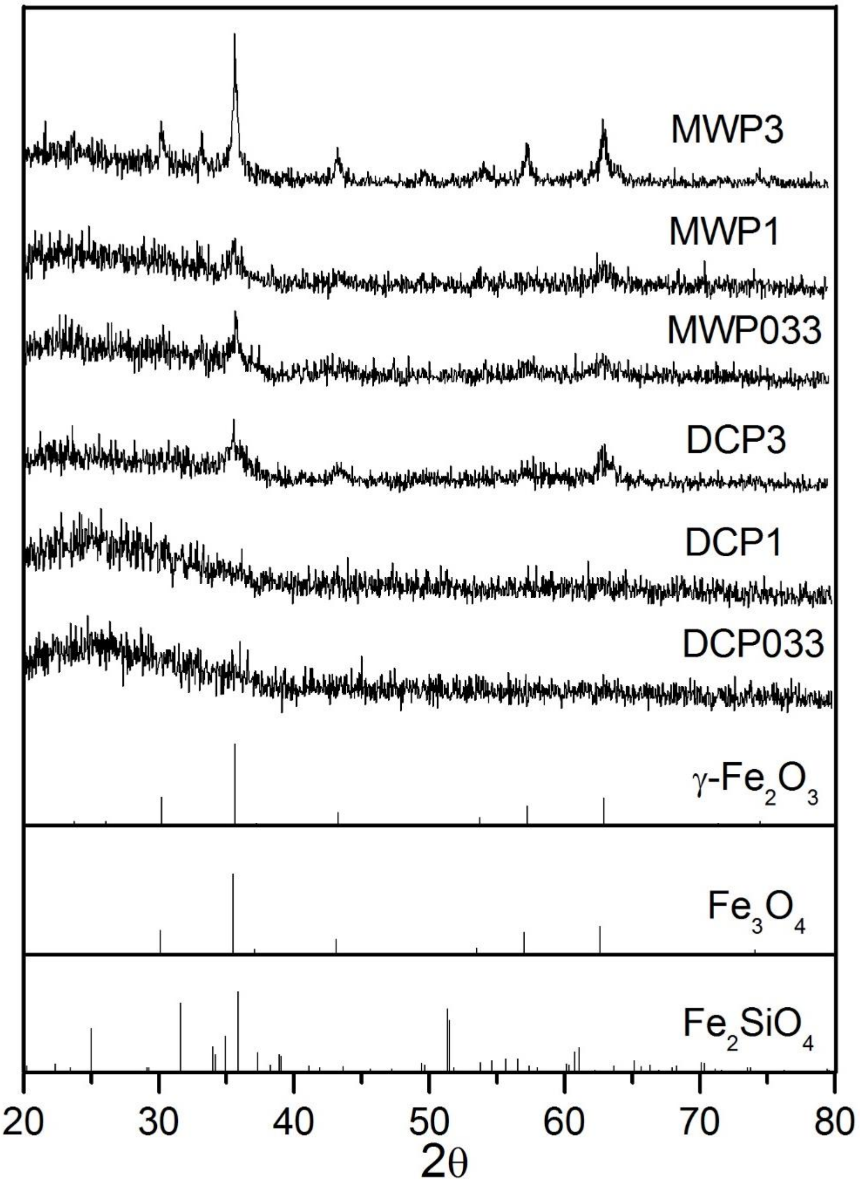

**Fig. 3.16**. XRD patterns of the samples prepared by microwave plasma with axial injection and by DC thermal plasma with various Fe/Si ratio

**Table 3.8**. Lattice parameter and silicon content of samples

| | Lattice parameter (Å) |
|---|---|
| MWPFe | 8.353 |
| MWP3 | 8.350 |
| MWP1 | 8.349 |
| MWP033 | 8.349 |
| DCPFe | 8.390 |
| DCP3 | 8.367 |
| DCP1 | - |
| DCP033 | - |

Absence of the peaks at DCP1 and DCP0333 is due to poor crystallization of the particles. Generally the samples prepared by the microwave plasma have relatively higher crystallinity than those by the DC thermal plasma. It may be because rapid cooling of thermal plasma limits crystal growth. Therefore it is implied that the crystallization is promoted in the microwave plasma rather than the DC thermal plasma.

Based on Table 3.8, the samples are compared as follows.

### a) MWPFe vs DCPFe

The lattice parameter of MWPFe is 8.353 while that of DCPFe is 8.390. Since Si-species were not used to synthesize MWPFe and DCPFe, the difference of the lattice parameter cannot be explained by the silicon content in the iron oxide structure. Faivre et al. investigated the lattice parameter of $Fe_3O_4$ and $\gamma$-$Fe_2O_3$ [102]. They reported 8.3907 for $Fe_3O_4$ and 8.3470 for $\gamma$-$Fe_2O_3$, which corresponds to DCPFe and MWPFe, respectively. The phase transformation of iron oxides is related to the temperature. It is known that $Fe_3O_4$ transforms to $\gamma$-$Fe_2O_3$ which is a metastable phase at 200~300℃ and then transforms soon to $\alpha$-$Fe_2O_3$ at 300~370℃ [103]. It is also well-known that $Fe_3O_4$

is stable phase at high temperature under oxygen rich condition. Therefore we can expect that if the cooling rate is fast enough, $Fe_3O_4$ phase freezes and then is obtained. If the cooling rate is not fast enough, $Fe_3O_4$ phase may transform to $\gamma$-$Fe_2O_3$ and finally $\alpha$-$Fe_2O_3$. Our results show that the expectation is valid. $Fe_3O_4$ was obtained by the DC thermal plasma having a faster cooling rate than the microwave plasma while $\gamma$-$Fe_2O_3$ was obtained by the microwave plasma. Actually other researchers have reported that $\gamma$-$Fe_2O_3$ can be easily synthesized by the microwave plasma [74, 75, 104, 105].

### b) MWPFe vs MWP3

Someone may predict that the MWP3 is also $\gamma$-$Fe_2O_3$ as like as MWPFe since both samples have close lattice parameters to that of $\gamma$-$Fe_2O_3$. To confirm that, those samples were heated in the electric furnace for 30 minutes at 773 K. Pictures of the samples before and after heat-treatment are shown in Fig. 3.17. The color of the samples before the heat-treatment were almost same, while the colors after the heat-treatment showed the difference. The color of MWPFe changed from dark brown to red, while that of MWP3 was maintained. The change of color means the transformation of the iron oxide from spinel structure including $Fe_3O_4$, $\gamma$-$Fe_2O_3$, $Fe_{3-x}Si_xO_4$ to $\alpha$-$Fe_2O_3$. However, the Si content in the crystalline iron oxide is believed to delay the phase transformation. Therefore it is considered from the results of the XRD and the heat-treatment that MWPFe and MWP3 are different and MWP3 includes Si in the iron oxide structure.

### c) MWP3 vs DCP3

MWP3 includes more silicon in the crystalline phase than DCP3. However since the Fe/Si ratio of the precursor flow of MWP3 and DCP3 was same, it is expected that the extra Si may exist in the amorphous phase. When it is combined with the comparison of the TEM images, the external layer of the large spherical particles in DCP3 is considered as the extra silica which cannot penetrate into the iron oxide lattice. To confirm the difference between MWP3 and DCP3, those samples were heated in the electric furnace for 30 minutes at 773 K as same as the above comparison between MWPFe and MWP. Pictures of those samples before and after heat-treatment are shown in Fig. 3.17. The color of DCP3 became close to red while that of MWP3 didn’t so change. From the above discussion, it is believed that MWP3 and DCP3 have different phase composite.

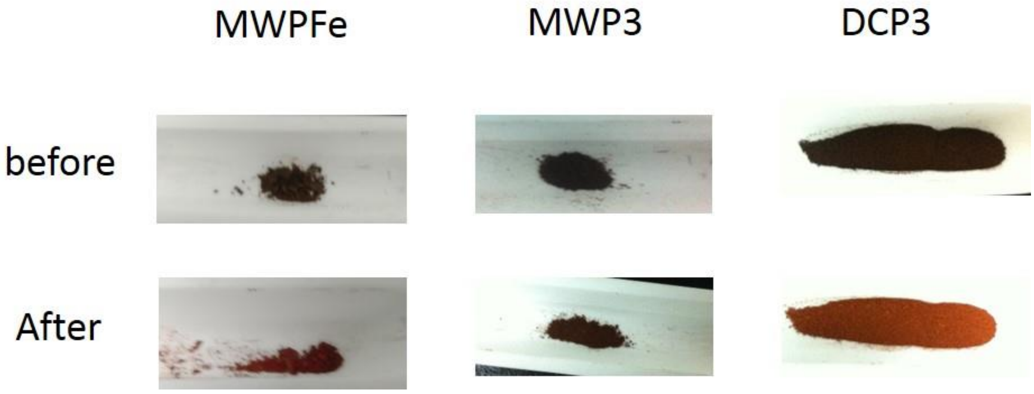

**Fig. 3.17**. Pictures of MWP3 and DCP3 before and after heat-treatment

**d) MWP3 vs MWP1 vs MWP033**

What is interesting is that the crystalline phases of these three samples have almost the same lattice parameter meaning almost the same phase composition. It is considered that the iron oxide-silica composite having the lattice parameter of 8.35 Å is the final crystalline product obtained from Fe-Si-O system. It will be discussed with thermodynamic consideration in the next section.

The chemical compositions confirmed from the XRD results and the above discussion are listed in Table 3.9.

**Table 3.9**. Chemical composition of the samples confirmed from XRD analysis

| Fe/Si ratio | Microwave plasma | DC thermal plasma |
|---|---|---|
| 3 | FeO-$SiO_2$ composite | FeO-$SiO_2$ composite* |
| 1 | FeO-$SiO_2$ composite | Amorphous |
| 0.33 | FeO-$SiO_2$ composite | Amorphous |
| Only Fe | $\gamma$-$Fe_2O_3$ | $Fe_3O_4$ |
| Only Si | Amorphous | Amorphous |

*However, the peaks of DCP3 deviates a little from those of MWP3, MWP1, and MWP033. In addition, the result of the heat treatment also shows the difference, remaining the possibility of the different composition from MWP3, MWP1, and MWP033.

### 3.3.3. Thermodynamic consideration

To explain the formation of the particles with various morphologies, we introduce a thermodynamic approach. The particle formation phenomena are considered to consist of two parts; one is a condensation of Fe- and Si-gaseous phase, another is quenching of the condensed phase. In this section, both are investigated with the thermodynamic consideration.

#### 3.3.3.1. Condensation of Fe- and Si-gaseous phase

In this section, the thermodynamic approach is introduced to explain the condensation of the gaseous phase. Many researchers have introduced the concept of nucleation temperature, which considers not only super-saturation but also collision, and surface tension of the condensed phases. However introducing the nucleation temperature theory to the multi-component system makes the calculation so complicated. Therefore we introduced only condensation of gaseous precursor in the equilibrium state in place of nucleation temperature. What is the most important is the relative behavior of Fe-species and Si-species. From our assumption, it is considered that the comparison of the condensation temperature is enough to compare the relative behavior of those phases. Although whether the composition and the behavior of the gaseous flow agrees with those in the equilibrium state is one of the main issues in thermal plasma chemistry, we assumed that it agrees with the equilibrium behavior.

First, typical equilibrium diagram of $75Fe(CO)_5$-$25(C_2H_5O)Si_4$-$700O_2$-9200Ar was calculated to confirm general behavior of Fe- and Si- related phase using the commercial program Factsage 5.3.1 which calculates equilibrium composition where Gibbs free energy is minimized. The diagram is shown in Fig. 3.18.

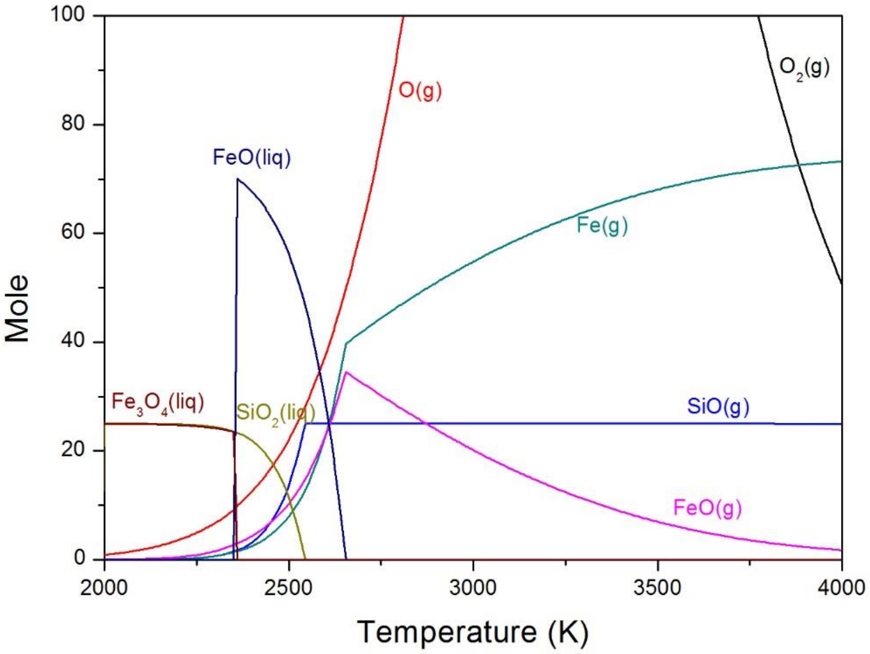

**Fig. 3.18**. Equilibrium diagram of 75Fe$(CO)_5$-25$(C_2H_5O)Si_4$-700$O_2$-9200Ar system

It is noted that only the species related to the condensation are sketched in Fig.3.18. Fe (g) and FeO (g) which are Fe-gaseous species are condensed to FeO (liq). SiO (g) which is Si-gaseous species is condensed to $SiO_2$ (liq). Although FeO (liq) is formed at the higher temperature than $SiO_2$(liq), the temperature at which Fe- or Si-species are condensed is changeable as the partial pressure of Fe- or Si-gaseous phase. Here, the condensation temperature is defined as the temperature where the condensed phase starts to form. The condensation temperature of FeO (liq) as Fe-condensed phase and $SiO_2$ (liq) as Si-condensed phase were calculated for different Fe/Si ratio and is shown in Fig. 3.29.

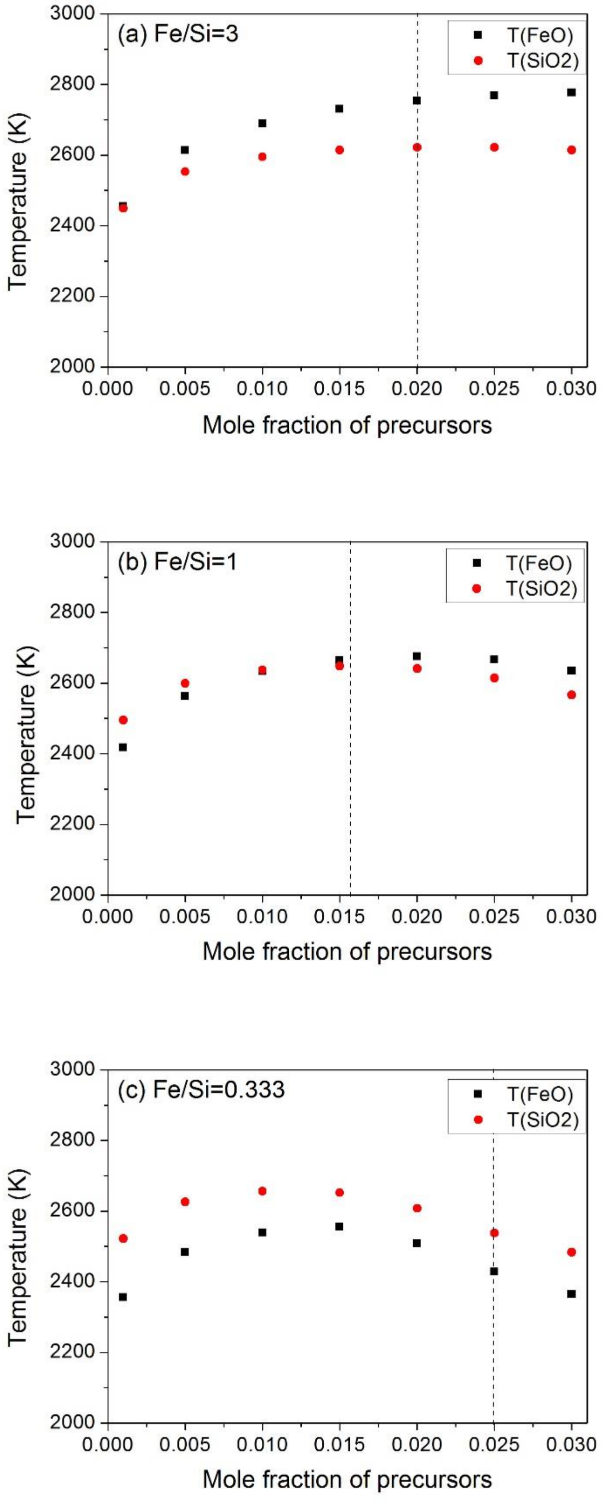

**Fig. 3.19**. Condensation temperature of FeO (liq) and SiO2 (liq) with Fe/Si ratio of (a) 3, (b) 1, and (c) 0.333; (dash line: mole fraction of precursors at experimental condition)

The condensation temperatures were calculated to evaluate the effect of the Fe/Si ratio and the mole fraction of the precursors. Because of the axial injection of the precursor flow and low Reynolds number (Re < 1,000), the precursor flow in the quartz tube is expected as laminar flow. Therefore the mixing of the precursor flow was expected to be poor so that the mole fraction in the precursor flow was assumed to be maintained during the condensation process. The dash lines in Fig. 3.19 indicate the mole fraction of each precursor used in each experimental condition.

Fig. 3.19 (a), (b) and (c) showed the condensation temperatures as a function of the mole fractions of the precursors when Fe/Si=3, 1 and 0.333.

When Fe/Si=3 (Fig.3.19(a)), FeO has slightly higher condensation temperature than $SiO_2$ at low mole fraction of the precursors. However the difference increases as the mole fraction increases. The higher nucleation temperature means a prior nucleation. Once FeO is condensed, the partial pressure of FeO around the condensed particle decreases. Therefore Si-rich phase becomes easily condensed on the surface of the as-condensed particle. As a result, the particle is composed of two phase separated each other.

When Fe/Si=1 (Fig. 3.19 (b)), the differences of the condensation temperature are not so large at the all of mole fraction regions. Therefore $SiO_2$ and FeO may be condensed simultaneously, forming the individual condensed particles.

When Fe/Si=0.333 (Fig. 3.19 (c)), $SiO_2$ has a higher nucleation temperature than FeO against all mole fractions. However FeO exists as a particle on $SiO_2$ core but not forms an external layer although $SiO_2$ is condensed earlier. It may be because FeO has a higher surface tension than $SiO_2$ through all temperature region.

### 3.3.3.2. Quenching of the condensed phase

The condensed particles at the previous section were cooled along the plasma flow. During the cooling sequence, the iron oxide phase and the silica phase in those particles were expected to diffuse. It is remarkable that the arrangement of FeO and $SiO_2$ resulted from the condensation is almost the same as the morphologies of the particles prepared by the DC thermal plasma, which means poor diffusion during the quenching sequence in the DC thermal plasma. On the other hand, the morphologies of the particles prepared by the microwave plasma changed during the quenching sequence. With the relatively low quenching rate, FeO and $SiO_2$ are mixed by the inner-particle diffusion. The determination of the final phase in the mixed oxide can be explained by a phase equilibrium diagram. The phase diagram enables to predict some points thus even if it is difficult to predict the exact final product with the phase diagram since the Fe-Si-O system in our experiments undergoes the processes which are far from the equilibrium such as the condensation and the quenching. The phase equilibrium diagram of a FeO-$SiO_2$ system in Fe-saturated condition shown in Fig. 3.20 implies the final phase includes fayalite ($Fe_2SiO_4$) regardless the initial composition of the condensed particle [106].

Above mentioned, MWP3, MWP1, and MWP033 also have almost FeO-$SiO_2$ phase of almost the same composition in common, although those patterns do not exactly correspond to the peaks of $Fe_2SiO_4$. From Fig. 3.16 the strongest peak of MWP3, MWP1, MWP033, DCP3, $Fe_2SiO_4$, $Fe_3O_4$, and $\gamma$-$Fe_2O_3$ are summarized in Table 3.10.

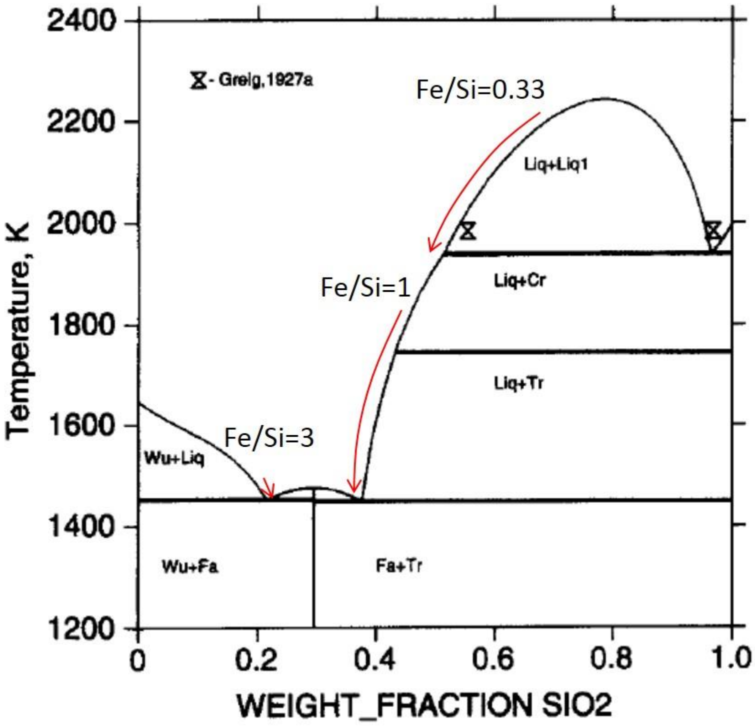

**Fig. 3.20**. Phase equilibrium diagram of a FeO-$SiO_2$ system in Fe-saturated condition (Abbreviations: Wu-wurtzite, Fa-fayalite, Tr-tridimite, Cr-cristabolite, Liq-liquid, Liql-silica rich liquid.)

**Table 3.10**. The strongest peaks of the samples and the reference

| Sample | MWP3 | MWP1 | MWP033 |
|---|---|---|---|
| Peak (°) | 35.63 | 35.64 | 35.63 |
| Sample | DCP3 | DCP3 | DCPFe |
| Peak (°) | 35.56 | 35.62 | 35.46 |
| Sample | $Fe_3O_4$ | γ-$Fe_2O_3$ | $Fe_2SiO_4$ |
| Peak (°) | 35.48 | 35.63 | 35.89 |

The strongest peaks of the materials are located close to each other. Furthermore the broad peaks make it difficult to distinguish the peaks. Here, an explanation is proposed to know if there are $Fe_2SiO_4$ in MWP3, MWP1, and MWP033. Fe/Si=3, Fe/Si=1 and Fe/Si=0.33 are corresponding to 22%, 46% and 71% respectively when it is written as weight fraction of $SiO_2$, x-axis of Fig. 3.20. The FeO-$SiO_2$ composite in the phase diagram approaches to fayalite which is the line positioned at $SiO_2$ fraction of 0.3. Concerning this, MWP3 approaches to fayalite from the left side, being separated to wurtzite (FeO). Since FeO is unstable at the room temperature, it may transform easily to the crystalline $Fe_3O_4$ or $\gamma$-$Fe_2O_3$. As a result, there is a possibility that both the crystalline iron oxide and the crystalline fayalite can be present. In contrast, both MWP1 and MWP033 approaches from the right side, meaning that MWP1 and MWP033 may undergo the similar mechanism. Actually it is observed from the TEM images that MWP1 and MWP033 have similar morphologies which are distinguished from that of MWP3. Approaching from the right side, $SiO_2$ is first solidified and then finally the fayalite is obtained. In this route, the iron oxide is not obtained. When we apply this explanation to the XRD result, the broad peaks of MWP1 and MWP033 is considered of the fayalite. In addition, some peaks of MWP3 corresponding to $Fe_3O_4$ or $\gamma$-$Fe_2O_3$ also may be explained, suggesting the co-existence of the iron oxide and the fayalite. However, the above explanation is nothing more than one of the possibility expected from the combination of the phase diagram and the XRD result. To find out exactly it, further analysis and further discussion about material science are required.

As a result, the cooling rate of the plasma flow should be considered. Generally DC thermal plasma has higher cooling rate as well as heating rate than microwave plasma. It is reported that DC non-transferred plasma has cooling rate with order of $10^7$ K/s

[107], while microwave plasma has that of $10^5$ K/s [108]. The lower cooling rate may provide long diffusion time which enable the diffusion of the components in the particles composed of the separated phases. The absence of the silica amorphous layer and the higher Si content in the crystalline iron oxide may be resulted from the low cooling rate. On the contrary to this, the higher cooling rate of the DC thermal plasma may suppress the diffusion, promoting the silica external layer and the individual silica particles.

#### 3.3.3.3. Confirmation of the effect of the condensation temperature

Here, we focus on MWP3_S shown in Fig. 3.21. Unlike MWP3, MWP3_S does not have any amorphous external layer and seems rather similar to MWP1. It is considered as a result of simultaneous condensation of the iron oxide and the silica. With the swirl injection, the mole fraction of the precursor decreases due to the mixing with the discharge gas flow having a much higher flow rate. As confirmed from Fig. 3.19 (a), the condensation temperature of the iron oxide and the silica become closer as the mole fraction of the precursor decreases when Fe/Si=3. Therefore the combination of the decrease in the mole fraction makes the condensed phase simultaneously generated as like as MWP1. With the simultaneous condensation, FeO and $SiO_2$ are easily mixed so that the external layer is not observed. This result enables to confirm that the difference of the condensation temperature contributed to make the difference in the particle morphology.

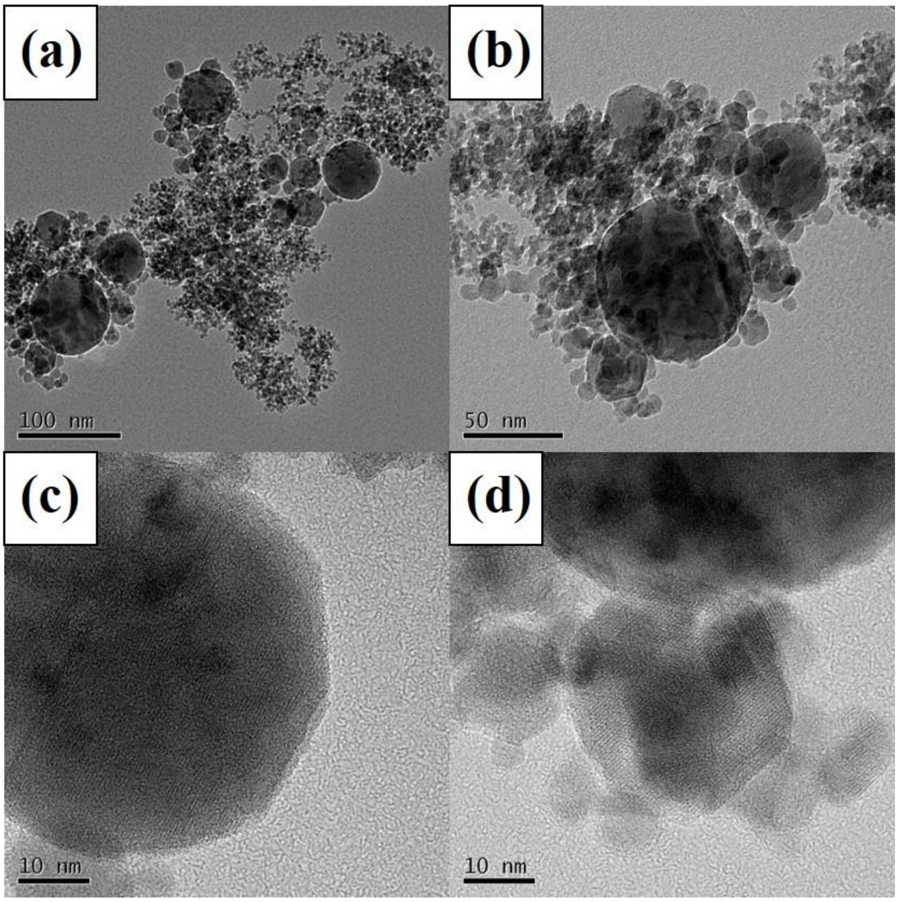

**Fig. 3.21**. TEM images of MWP3_S with various magnifications

### 3.3.4. Formation phenomena of iron oxide-silica composite

The expected particle formation phenomena from the discussion of the previous section are visualized in Fig. 3.22.

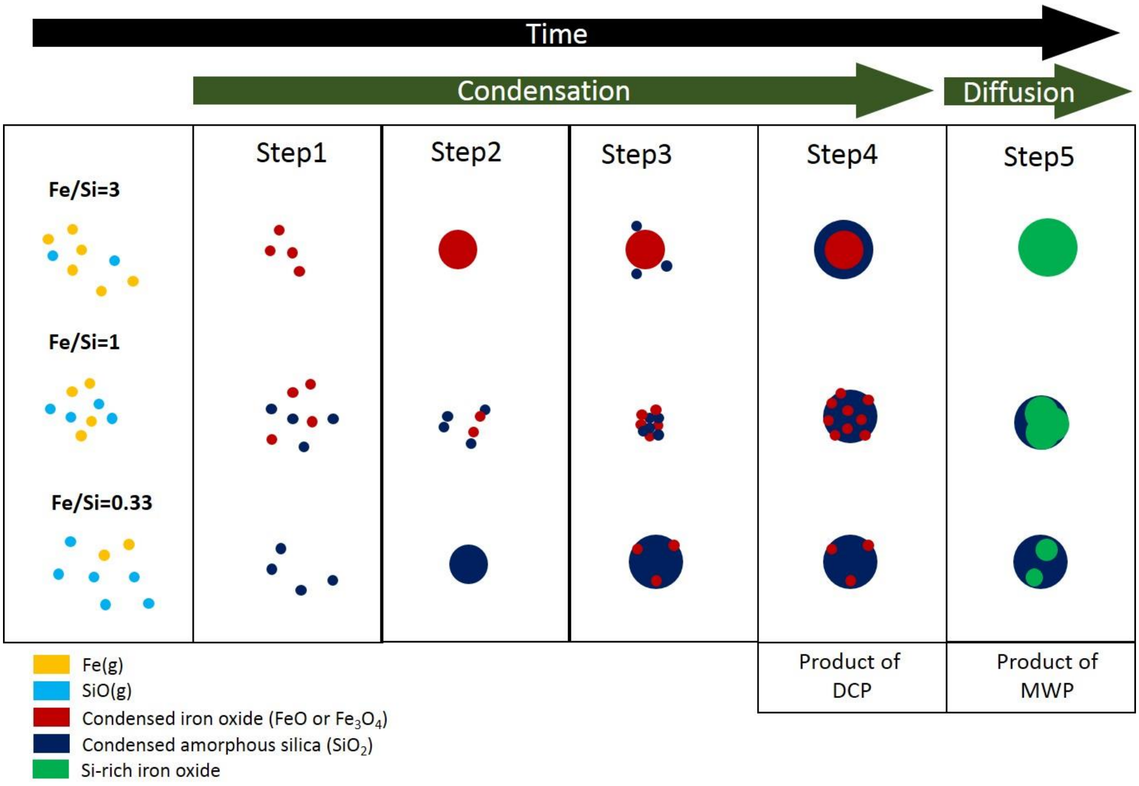

**Fig. 3. 22**. Scheme of particle formation phenomena

When Fe/Si=3, Fe(g) first condenses to the iron oxide. Until the temperature decreases to the condensation temperature of the silica, the iron oxide is condensed alone and grows. If the temperature reaches the condensation temperature of the silica, the silica is condensed. Because heterogeneous nucleation is prior to homogeneous nucleation, the silica is easily condensed on the surface of the iron oxide. Due to the low surface tension of the silica, it covers the iron oxide, forming core-shell structure. In the DC thermal plasma, the particle escapes from the hot region and freezes at this step. In the microwave plasma, the particle is still in the hot region and the separated components in a particle diffuse. Finally the iron oxide-silica composite is obtained although some large particles still have thin external layer.

When Fe/Si=1, Fe(g) and SiO(g) condense simultaneously to the iron oxide and the silica, respectively. By the collision between the condensed particles, the iron oxide and the silica are irregularly arranged and then the particle composed of both the iron oxide and the silica is formed. In the DC thermal plasma, the diffusion of each component in the particle is poor so that the particle freezes, keeping the separation of the two phases. In the microwave plasma, the components diffuse in the particle. Finally the iron oxide-silica composite is obtained.

When Fe/Si=0.33, SiO(g) first condenses to the silica. Until the temperature decreases to the condensation temperature of the silica, the silica is condensed alone and grows. If the temperature reaches the condensation temperature of the iron oxide, the iron oxide is condensed. On the contrary to Fe/Si=3, the iron oxide is easily condensed on the surface of the silica. However since the surface tension of the silica is lower than that of the iron oxide, the iron oxide does not coat but just is adsorbed. It leads to the similar result of the condensation to that when Fe/Si=1. In the DC thermal plasma, the particle freezes keeping the iron oxide particle on the silica surface. In the microwave plasma, the iron oxide diffuses into the silica so that the iron oxide-silica composite is partly formed. It is noticed that the results when Fe/Si=0.33 are similar to those when Fe/Si=1 in the both plasmas.

## 3.4. Summary

The particle preparation in Fe-Si-O system was performed using the atmospheric microwave plasma. The results were compared those of the DC thermal plasma. The variety of the particle morphology was synthesized as the Fe/Si ratio changes. However the particles prepared by the microwave plasma had the iron oxide-silica composite phase regardless the Fe/Si ratio with the higher Si content than that of the DC thermal plasma. Therefore it is summarized that the moderate quenching rate of the microwave plasma provided enough time the components in the particle to diffuse. The results of this chapter also propose that the microwave plasma may be applicable to the processing to require the relatively long residence time than that of the DC thermal plasma.

## Chapter 4

# Effect of microwave plasma on particle processing

## 4.1. Introduction

It is confirmed from the previous chapters that the heating sequence and the cooling sequence have an important role to determine the final product. In Chapter 2, the moderate heating rate of the microwave plasma brought the different results compared to those by the DC thermal plasma and the electrical furnace, contributing to the formation of the smooth surface. In Chapter 3, the moderate cooling rate of the microwave plasma led to the different products from those by the DC thermal plasma, contributing to the diffusion of the components in the particle. In this chapter, the calculations are performed with two model. One is a particle flowing in the high temperature region of the plasma, corresponding to Chapter 2. The particle undergoes reaction, melting and evaporation as it is heated. Another is a multi-component particle flowing in the cooling region of the plasma, corresponding to Chapter 3.

The purpose of this chapter is to demonstrate the experimental results qualitatively and finally to investigate the unique particle processing using the atmospheric pressure microwave plasma.

## 4.2. Velocity and temperature of the plasmas

The velocity and the temperature distribution of the atmospheric pressure microwave plasma and the DC thermal plasma are referred from the existing researches [107, 108]. The plasma have the temperature and the velocity distribution along the center of the axial direction (r = 0). Those distributions are shown in Fig. 4.1.

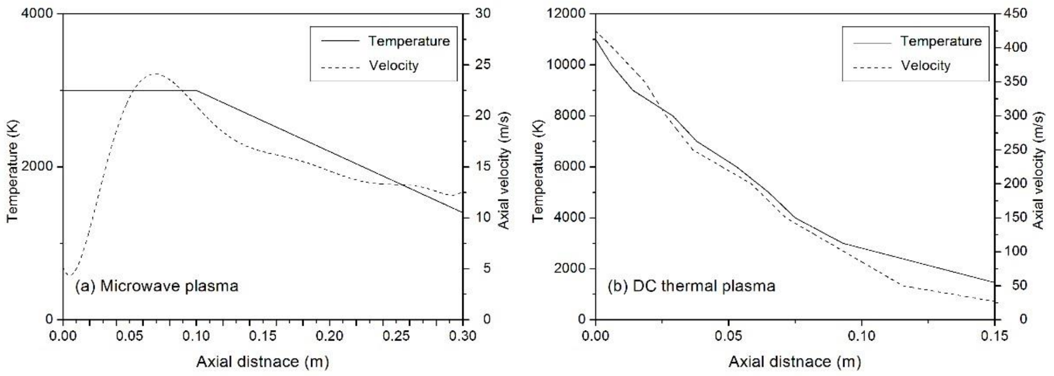

**Fig. 4.1**. Temperature and velocity distribution of

(a) microwave plasma and (b) DC thermal plasma

The microwave plasma has the maximum temperature about 3,000 K and the maximum axial velocity about 20 m/s. The temperature distribution shows that there is the region where the highest temperature is maintained, called as ‘plasma column’. It have been already reported that the temperature of the microwave plasma does not fluctuate in the plasma column. The axial velocity has the lowest value near the injection part because the swirl flow is yet strong here. However the axial velocity increases as it flows due to the dissipation of the swirl flow.

The DC thermal plasma has the maximum temperature over 10,000 K and the maximum axial velocity over 400 m/s. The temperature and the velocity of the DC thermal plasma decrease continuously in contrast to the microwave plasma.

# 4.3. Particle heating

## 4.3.1 Governing equations

### 4.3.1.1 Temperature variation

The particle temperature in a one-dimensional plasma is calculated from the following energy balance equation if the reaction or phase transition is not concerned [109].

$$A_p h_p \left(T_f - T_p\right) = m_p C_{p_p} \frac{dT_p}{dt} \quad (4.1)$$

Where $m_p$ is mass of a particle, $C_{pp}$ is specific heat of a particle, $T_p$ is surface temperature of a particle, $T_f$ is a temperature of a fluid, $t$ is time, $A_p$ is surface area of a particle and, $h_p$ is a heat transfer coefficient. The left term of Eq (4.1) means the energy required to increase the particle temperature per time. The right term of Eq (4.1) means the energy transferred to the particle from the plasma per time. Therefore Eq (4.1) indicates that how much particle temperature can change by the energy applied to the particle. Here $h_p$ is calculated from Eq (4.2) if the spherical particle is assumed

$$Nu = \frac{h_p D_p}{k} = \left(2 + 0.6 Re^{\frac{1}{2}} Pr^{\frac{1}{3}}\right) \left(\frac{\rho_0 \mu_0}{\rho_s \mu_s}\right)^{0.6} \left(\frac{C_{p_o}}{C_{p_s}}\right)^{0.38} \quad (4.2)$$

Where $Nu$ is Nusselt number, $D_p$ is particle diameter, $Re$ is Reynolds number, $Pr$ is Prandtl number, $k$ is thermal conductivity of a fluid, $\rho_0$ is density of a fluid at the bulk plasma temperature, $\rho_s$ is density of a fluid at the particle surface temperature, $\mu_0$ is viscosity of fluid at the bulk plasma temperature, $\mu_s$ is viscosity of fluid at the particle surface temperature, $C_{p0}$ is specific heat of fluid at the bulk plasma temperature and $C_{ps}$ is specific heat of fluid at the particle surface temperature. *Re* and *Pr* are obtained from the following relationship.

$$Re = \frac{D_p(u_f - u_p)\rho_f}{\mu_f} \qquad (4.3)$$

$$Pr = \frac{\mu_f C_{p_f}}{k} \qquad (4.4)$$

Where $u_f$ is velocity of a fluid, $u_p$ is velocity of a particle, $\rho_f$ is density of a fluid, $\mu_f$ is viscosity of fluid, $C_{pf}$ is specific heat of a fluid. In Eq (4.2), (4.3) and (4.4), all of the thermodynamic properties are used as the average of those between the fluid temperature and the particle surface temperature. It is noticed that the velocity term of Reynolds number is relative velocity between the fluid velocity and the particle velocity, ($u_f$ - $u_p$).

If the reaction or the phase transition is concerned, the energy balance for the particle heating is written as the follows;

$$Q_p = Q_R + Q_s + Q_m + Q_e \qquad (4.5)$$

where $Q_p$ is the total heat applied to the particle from the plasma, $Q_R$ is the heat required for the reaction, $Q_S$ is the heat required for the temperature increase of the particle surface, $Q_m$ is the heat required for the melting and $Q_e$ is the heat required for the evaporation.

Based on Eq (4.1), the balance equation can be written as the temperature range.

$$T_p < T_r \,,\ A_p h_p\left(T_f - T_p\right) = m_p C_{p_p} \frac{dT_p}{dt} \tag{4.6}$$

$$T_r \le T_p \le (T_r + 50)\,,\ A_p h_p\left(T_f - T_p\right) = \left(C_{p_p} + \frac{\Delta H}{50}\right) m_p \frac{dT_p}{dt} \tag{4.7}$$

$$(T_r + 50) < T_p < (T_m - 5)\,,\ A_p h_p\left(T_f - T_p\right) = m_p C_{p_p} \frac{dT_p}{dt} \tag{4.8}$$

$$(T_m - 5) \le T_p \le (T_m + 5)\,,\ A_p h_p\left(T_f - T_p\right)$$

$$= \left(\frac{C_{p_p} + C_{p_l}}{2} + \frac{L_m}{10}\right) m_p \frac{dT_p}{dt} \tag{4.9}$$

$$(T_m + 5) < T_p < T_e,\ A_p h_p\left(T_f - T_p\right) = m_p C_{p_l} \frac{dT_p}{dt} \tag{4.10}$$

where $T_r$ is the reaction temperature, $T_m$ is the melting temperature, $T_e$ is the evaporation temperature, $\Delta H$ is the enthalpy of the reaction, $C_{pl}$ is specific heat at liquid phase, and $L_m$ is a latent heat of melting.

The reaction is assumed to start at $T_r$ and finish at ($T_r$ + 50). Also the melting occurs during 10 K with the specific latent heat of $L_e$/10 [J/K·Kg] due to the convenience of the calculation. When $T_p$ reaches $T_e$, the evaporation starts without further increase of $T_p$. The evaporation of the particle is treated at the next section.

### 4.3.1.2. Evaporation

If the particle temperature reaches the evaporation temperature, the particle diameter can be calculated by the following equation.

$$h_p\left(T_f - T_e\right) = (-\frac{dr_p}{dt})\rho_p L_e \qquad (4.13)$$

Here $r_p$ is a radius of a particle, equal to $D_p/2$ and $L_e$ is latent heat of evaporation. Since the particle temperature is constant during the phase transition, it doesn't become a function of time any more but the particle diameter does. When $r_p = 0$, it is said that the particle is completely evaporated.

### 4.3.1.3. Velocity variation

A particle with the initial velocity $u_0$ changes with the fluid velocity. The variation of the relative velocity between the fluid and the particle is calculated by Eq (4.14).

$$\frac{d(u_f - u_p)}{dt} = \frac{18\mu_f}{\rho_p D_p^2}\frac{C_D Re}{24}\left(u_f - u_p\right) + g \qquad (4.14)$$

Where $C_D$ is drag coefficient and $g$ is gravitational acceleration. For the limits of low Reynolds number, the factor $C_D Re/24$ approaches unity. $g$ is introduced since the axial direction in our experiments forwards to the gravitactic orientation. Eq (4.5) means the acceleration of the particle in the flow so that the integral of Eq (4.5) enable to obtain the velocity of the particle because the fluid velocity is given from the plasma. For all calculations, the initial particle velocity $u_{p0}$ is assumed as 2 m/s.

### 4.3.2. Properties of particle

In the calculation for the particle heating, we try to describe the behavior of $In(OH)_3$ as like as in Chapter 2. In an effort of that, the particle properties was chosen close to those of the particle actually used in the experiments. Actually the properties of $In(OH)_3$ is desirable during the initial step, the properties of $In_2O_3$ are used for whole calculations due to the difficulty to obtain those. In addition the latent heats are referred from those of alumina since it was difficult to obtain those of $In_2O_3$. The properties of the particle are summarized at Table 4.1.

**Table 4.1**. Properties of particle

| | |
|---|---|
| Diameter ($D_p = 2\times r_p$) | 10 μm |
| Density ($\rho_p$) | 7179 Kg/m3 |
| Molar mass | 0.27764 Kg/mol |
| Reaction temperature ($T_r$) | 500 K – 550 K |
| Enthalpy of reaction ($\varDelta H$) | $4.68\times10^5$ J/Kg |
| Melting temperature ($m_p$) | 2186 K |
| Latent heat of melting ($L_m$) | $1.0\times10^6$ J/Kg |
| Evaporation temperature ($T_e$) | 2800 K |
| Latent heat of evaporation ($L_e$) | $2.5\times10^7$ J/Kg |

### 4.3.3. Assumptions

The followings are assumed for the calculation.

1) The particle has spherical morphology.

2) Radiation from/to the particle is neglected.

3) The influence of the gas product obtained from the reaction or the evaporation of the particle on the plasma properties is neglected.

4) The temperature in the particle is constant.

### 4.3.4. Properties of fluid

Since the calculation for the particle heating is performed to explain the experimental results of Chapter 2, the properties of the fluid in the calculation are chosen as used in Chapter 2. The properties of the air is used for the calculation using the microwave plasma. In case of the calculation using the DC thermal plasma, the two types of the fluid are concerned; One is the pure argon and another is the argon-nitrogen mixture with ratio of 8:2. The thermodynamic properties of the argon-nitrogen mixture are obtained by concerning the mole fraction of each gas component.

## 4.3.5. Results and discussion

Fig. 4.2 shows the change of the temperature and the particle diameter along the atmospheric microwave air plasma flow. The particle with the initial diameter of 10μm rapidly undergoes the reaction, the melting and reaches the evaporation temperature. The final particle diameter is 8.29μm.

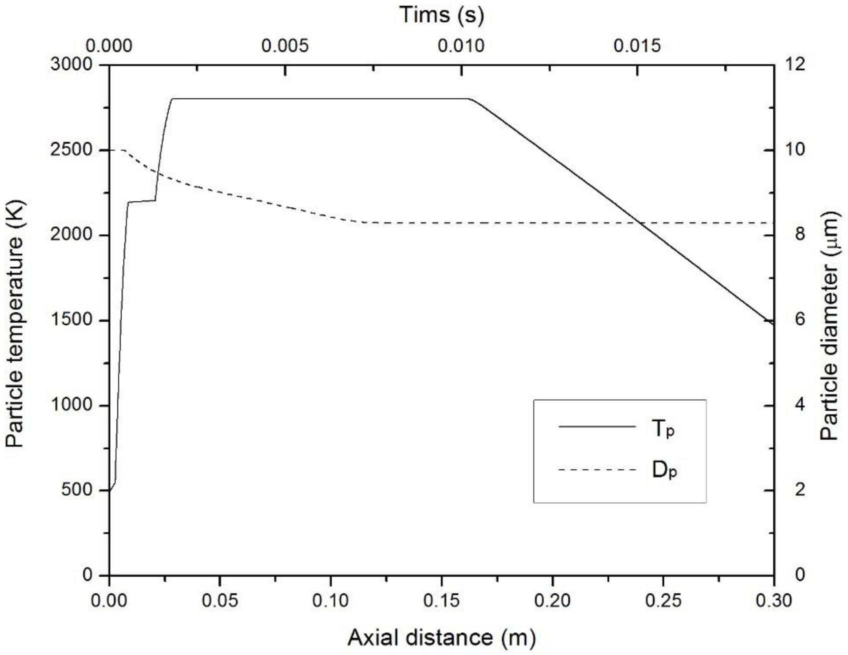

**Fig. 4.2**. Temperature and diameter change of the 10 μm particle in the microwave air plasma (straight line : particle temperature, dash line : diameter)

Fig. 4.3 shows the change of the temperature and the particle diameter along the DC thermal argon plasma flow. The range of the axial distance here was set-up from 0 m to 0.15 m based on the experimental apparatus, while that of the microwave plasma from 0 m to 0.3 m. However it does not affect the evaporation performance since the temperature after 0.15 m is lower than the evaporation temperature. The final particle diameter is 9.33 μm. It is remarkable that the evaporation performance of the DC thermal plasma was not as well as that of the microwave plasma. The reason for this is considered as the low thermal conductivity of the argon. The thermal conductivity of the argon, the nitrogen and the air are plotted in Fig. 4.4. It seems that the thermal conductivity of the nitrogen and the air have peaks. These peaks are due to the dissociation and the recombination of $N_2$ and $O_2$ which promotes the heat transfer in the discharge region. The thermodynamic properties of the nitrogen and the air introduced in this calculations assumes the equilibrium state of the dissociation and the recombination of $N_2$ and $O_2$. The peak at 3,800 K for the air is due to the dissociation and the recombination of $O_2$. The peak at 7,000 K for both the nitrogen and the air is due to the dissociation and the recombination of $N_2$. Therefore introducing the nitrogen or the air is expected to promote the evaporation of the particle. The reason that the particle is evaporated in the microwave air plasma can be also explained with this in some degree.

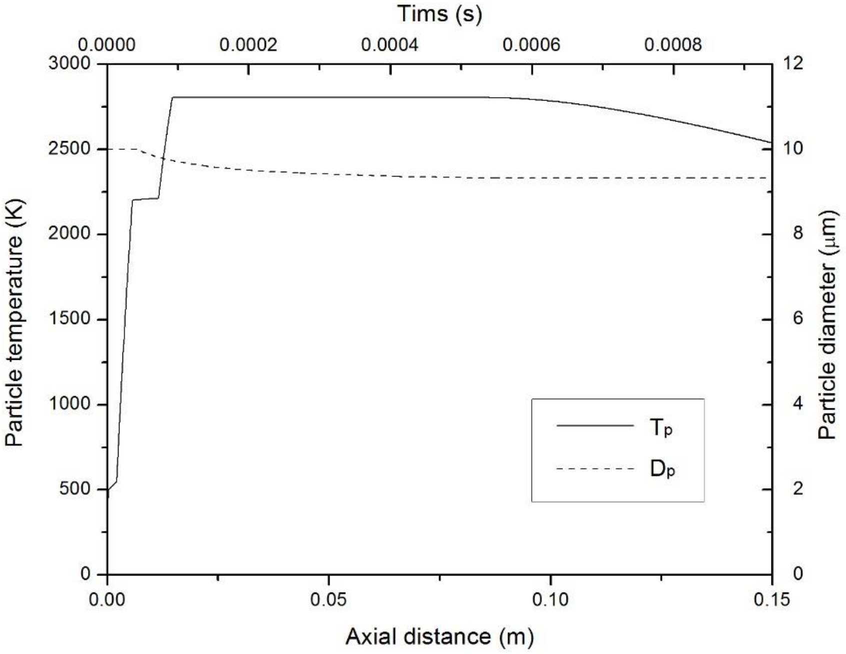

**Fig. 4.3**. Temperature and diameter change of the 10 μm particle in the DC thermal argon plasma (straight line : particle temperature, dash line : diameter)

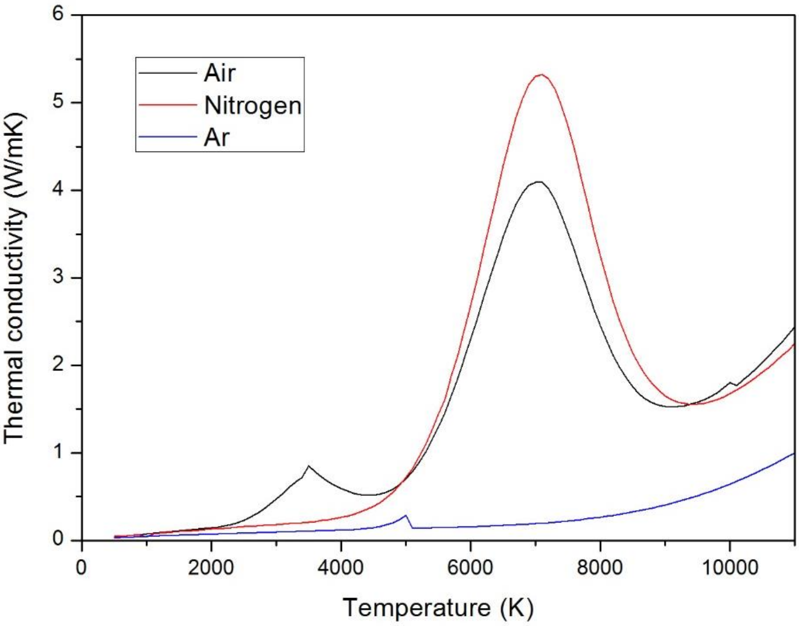

**Fig. 4.4**. Thermal conductivity of argon, nitrogen, and air

Fig. 4.5 shows the change of the temperature and the particle diameter along the DC thermal argon (80%)-nitrogen (20%) mixture plasma flow. The final particle diameter is 7.43 μm. The evaporation performance enhanced by the addition of the nitrogen as expected above.

The diameter after the plasma treatment and the evaporation ratio of the particle is summarized in Table 4.2. The evaporation ratio is defined as the ratio of the difference of the particle volume after and before the plasma treatment to the initial particle volume. It is remarkable that the evaporation performance of the DC thermal plasma was not as well as that of the microwave plasma. The reason for this is considered as the low thermal conductivity of the argon. The thermal conductivity of the argon, the nitrogen and the air are plotted in Fig. 4.4. It seems that the thermal conductivity of the nitrogen and the air have peaks. These peaks are due to the dissociation and the recombination of $N_2$ and $O_2$ which promotes the heat transfer in the discharge region. The thermodynamic properties of the nitrogen and the air introduced in this calculations assumes the equilibrium state of the dissociation and the recombination of $N_2$ and $O_2$. The peak at 3,800 K for the air is due to the dissociation and the recombination of $O_2$. The peak at 7,000 K for both the nitrogen and the air is due to the dissociation and the recombination of $N_2$. Therefore introducing the nitrogen or the air is expected to promote the evaporation of the particle. The reason that the particle evaporated in the microwave air plasma can be also explained with this in some degree.

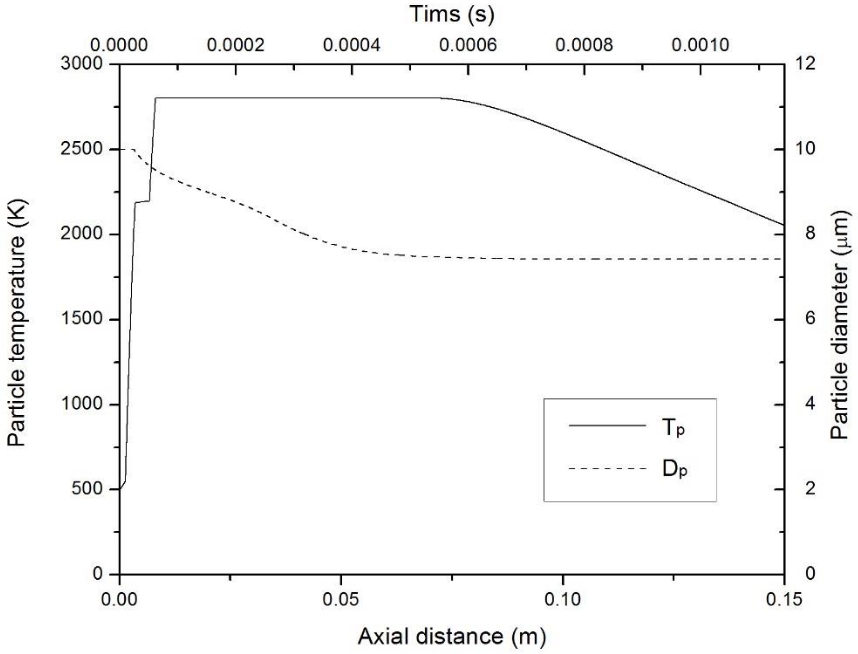

**Fig. 4.5**. Temperature and diameter change of the 10 μm particle in the DC thermal argon-nitrogen mixutre plasma

(straight line : particle temperature, dash line : diameter)

**Table 4.2**. Diameter and evaporation ratio of the particle in each plasma

| | Diameter (μm) | Evaporation ratio |
|---|---|---|
| Before evaporation | 10 | |
| Microwave air plasma | 8.29 | 0.43 |
| DC thermal argon plasma | 9.33 | 0.19 |
| DC thermal Ar-$N_2$ plasma | 7.43 | 0.59 |

## 4.4. Particle quenching

In this section, the cooling of the multi-component particle is concerned. In Chapter 3, the difference of the quenching rate was considered to make the difference of the diffusion rate in the particle. To demonstrate that, we calculate the diffusion distance of the component in the particle as a function of the quenching rate. In this calculation, the temperature and the velocity of the particle is assumed as same as those of the fluid because the particle is small ($D_p < 100$ nm).

### 4.4.1. Diffusion in the particle

Prior to the calculation, the particle model is shown in Fig. 4.6. Although the particle seemed like sphere in Chapter 3, the diffusion in a slab is assumed in this calculation.

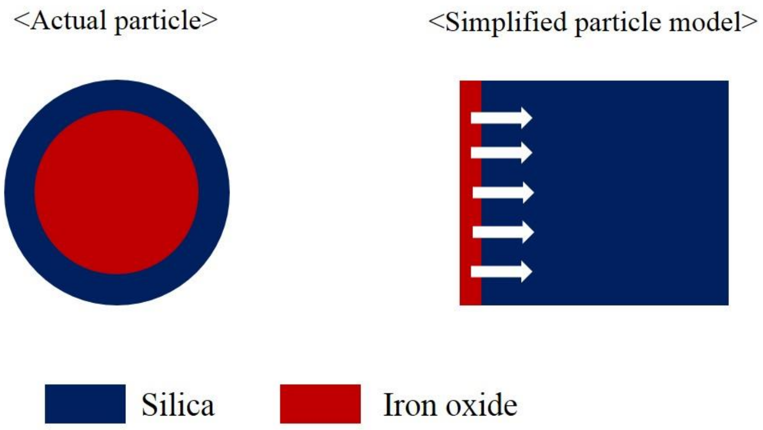

**Fig. 4.6**. Scheme of the particle model

Since the relationship between the time and the degree of diffusion is calculated, the unsteady-state diffusion is assumed. The governing differential equation for this is called Fick's second law of diffusion written by the following equation.

$$\frac{\partial C}{\partial t} = D\frac{\partial^2 C}{\partial x^2} \qquad (4.15)$$

where $C$ is concentration of diffusion component, $t$ is time, $D$ is diffusivity, and $x$ is distance in direction of diffusion.

For diffusion into or out of a slab with constant diffusivity, the solution for the average concentration $c$ is as the follows [110];

$$\frac{C_s - C}{C_s - C_0} = \frac{8}{\pi}\left[e^{-a_1 Fo_m} + \frac{1}{9}e^{-9a_1 Fo_m} + \frac{1}{25}e^{-25a_1 Fo_m} + \cdots\right] \qquad (4.16)$$

where $C_s$ is surface concentration of diffusing component, $C_0$ is initial concentration in the slab, $a_1$ is $(\pi/2)^2$ and $Fo_m$ is Fourier number for mass transfer. $Fo_m$ is written by the follow expression;

$$Fo_m = \frac{Dt}{s^2} \qquad (4.17)$$

where s is one-half slab thickness.

Therefore if the time ($t$), the surface concentration ($C_s$), the initial concentration ($C_0$) and the final average concentration ($C$) are determined, the diffusion distance (2s) is obtained.

## 4.4.2. Parameters

In the simplified particle model, the iron oxide phase diffuses to the silica layer by one-way diffusion and the concentration of the iron oxide is maintained as constant. The parameters in Eq (4.16) and Eq (4.17) except $t$ should be determined.

For the concentration, $C_s = 1$, $C_0 = 0$, and $C = 0.67$ are assumed. The reason for $C = 0.67$ is that the final product by the diffusion is considered as $Fe_2SiO_4$.

The time for the diffusion, $t$ is calculated from the quenching rate. Since the particle is condensed at 2,500 K and is solidified at 1,500 K, $t$ is calculated by the following equation;

$$t[s] = \frac{(2500\ K - 1500\ K)}{Quenching\ rate\ [K/s]}$$

The quenching rate is varied from $10^0$ to $10^{10}$ K/s.

For the diffusivity, the diffusivity of iron in $SiO_2$ is used as written by

$$D = 4 \times 10^{-8} exp\left(\frac{-1.51\ eV}{kT}\right)$$

where k is Boltzmann constant for the electron ($8.617 \times 10^{-5}$ eV/K) and $T$ is temperature [110]. In addition, $D$ at 2000K is used for all temperature region for the convenience of the calculation.

### 4.4.3. Results and discussion

The result of the calculation shown in Fig. 4.7 implies the diffusion distance is proportional to the root of the quenching rate. From Fig. 4.1, the quenching rate from 2,500 K to 1,500 K was about $10^5$ K/s for the microwave plasma and about $10^7$ K/s for the DC thermal plasma. The red dash lines in Fig. 4.7 indicate the quenching rate and the corresponding diffusion distance for the microwave plasma and the DC thermal plasma, respectively. The diffusion distance in the microwave plasma is 8.3 nm while that in the DC thermal plasma 0.83 nm. When combined with the results in Chapter 3, it is implied that the external layer formed by the different condensation temperature of the iron oxide and the silica with the thickness of several nm disappears during the quenching process in the microwave plasma.

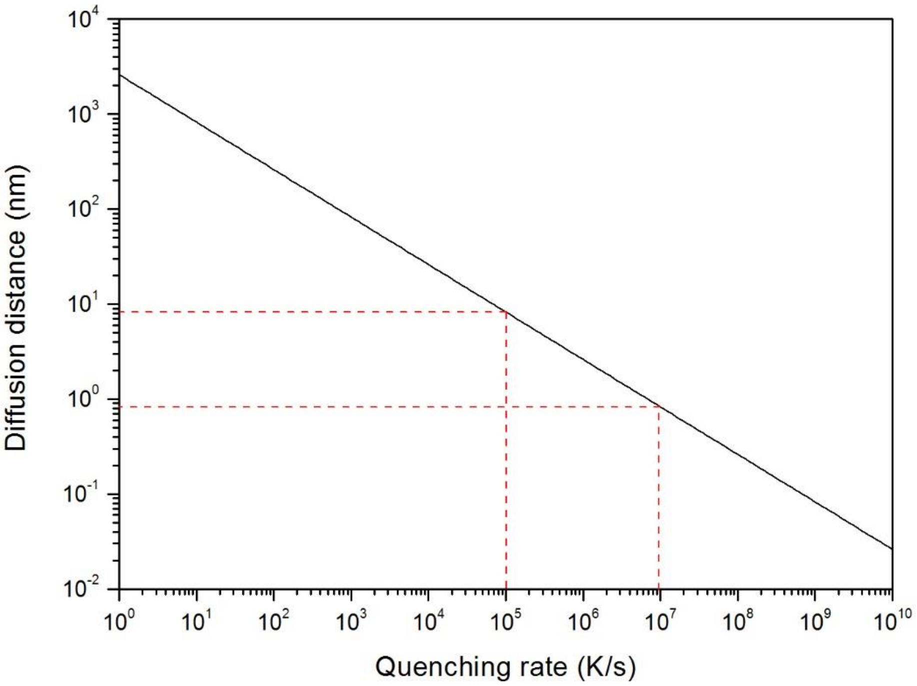

**Fig. 4.7**. Diffusion distance of Fe in $SiO_2$ as a function of quenching rate

## 4.5. Summary

In this chapter, the calculations were performed to demonstrate the results obtained from the previous chapters.

For the demonstration of Chapter 2, the performance of the particle evaporation during the particle heating in the microwave plasma and the DC thermal plasma was calculated. The results of the calculations implied that the microwave plasma having the moderate temperature enables the moderate particle heating compared to the DC thermal plasma.

For the demonstration of Chapter 3, the diffusion distance in the particle during the particle quenching in the microwave plasma and the DC thermal plasma was calculated. The result showed that the diffusion in the microwave plasma is faster than that in the DC thermal plasma.

## Chapter 5

# Conclusions

The particle preparation was performed using the atmospheric pressure microwave plasma. The atmospheric pressure microwave plasma can induce the reactive field with the moderate temperature close to 3,000 K compared to that of the thermal plasma but still higher than that of the conventional method. In this thesis, the particle processing using these reactive field has tried to investigate the factor to lead to the unique particle formation phenomena.

In Chapter 2, the preparation of the indium oxide ($In_2O_3$) by the dehydration of the indium hydroxide ($In(OH)_3$) was conducted. $In_2O_3$ prepared by the microwave plasma did not evaporate in contrast with that by the DC thermal plasma and had the smooth surface in contrast with that by the electric furnace. The unique heating rate of the microwave plasma was considered to have an important role to prepare the smooth surface by promoting the diffusion of the dehydrated vapor as well as to dehydrate $In(OH)_3$ without the evaporation.

In Chapter 3, the synthesis of the iron oxide-silica composite was conducted. The synthesized particles by the microwave plasma had the iron oxide-silica mixed phase, while the iron oxide and the silica were separated in that by the DC thermal plasma. The moderate quenching rate of the microwave plasma was considered to permit the diffusion in the condensed particle, while the rapid quenching rate of the DC thermal plasma froze the condensed particle.

From Chapter 2 and Chapter 3, the moderate heating and quenching rate is believed to induce the difference from the DC thermal plasma. To evaluate that, the temperature variation and the evaporation of the particle in the plasma corresponding Chapter 2 and the diffusion distance in the particle during the quenching process corresponding Chapter 3 were calculated in Chapter 4. It is confirmed that the microwave plasma enables the moderate particle heating compared to the DC thermal plasma and that the diffusion in the multi-component particle is faster at the microwave plasma than the DC thermal plasma. Finally it was concluded that the temperature of the microwave plasma close to 3,000 K induced the relatively low heating and quenching rate, which contributed to the preparation of the unique particle.

# References

[1] Maher I. Boulos, Pierre Fauchais, and Emil Pfender, “THERMAL PLASMA 1”, Plenum Press, New York, 1994.

[2] P. H. Yih and V. Saxena, “A review of SiC reactive ion etching in fluorinated plasmas,” *Physica Status Solidi.*, 202 (1997) 605-642.

[3] P. Pleshko, N. Apperley, L. L. Zimmerman, K. A. Pearson, T. A. Sherk, E. J. St.Pierre, B. Hairabedian, F. Bradney, and R. L. J. Foster: “Design of a plasma flat panel large screen display for high volume manufacture,” *Displays,* 5 (1984) 21-32.

[4] J. Wilden, J. P. Bergmann and H. Frank: “Plasma transferred arc welding—modeling and experimental optimization,” *J. Therm. Spray Tech.*, 15 (2006) 779-784.

[5] F. W. Crawford: “Microwave plasma devices—Promise and progress.” *Proceedings of the IEEE,* 59 (1971) 4-19.

[6] Alexander Fridman, “PLASMA CHEMISTRY”, Cambridge University Press, New York, 2008.

[7] K. Gadonna, O. Leroy, P. Leprince, L. L. Alves, and C. Boisse-Laporte, “Study of Gas Heating by a Microwave Plasma Torch,” *J. Mod. Phys.*, 3 (2012) 1603-1615.

[8] E. Tatarova, F. M. Dias, E. Felizardo, J. Henriques, M. J. Pinheiro, C. M. Ferreira and B. Gordiets, “Microwave air plasma source at atmospheric pressure: Experiment and theory,” *J. Appl. Phys.*, 108 (2010) 123305-123305.

[9] S. Y. Moon and W. Choe, “Parametric study of atmospheric pressure microwave-induced Ar/$O_2$ plasmas and the ambient air effect on the plasma,” *Physics of plasmas,* 13 (2006) 103503-103503.

[10] S. Ono, T. Suganuma, and Y. Suzuki, “Oxygen radical density in atmospheric

pressure Ar-$O_2$ microwave plasma for plasma cleaning," International Plasma Chemistry Society Conference.

[11] H. S. Uhm, J. H. Kim, and Y. C. Hong, "Microwave steam torch,"*Appl. Phys. Lett.*, 90 (2007) 211502-211502.

[12] W. L. T. Chen, J. Heberlein, and E. Pfender, "Temperature and velocity measurements in turbulent argon-helium plasma jets," *Proceedings of Tenth International Symposium on Plasma Chemistry, Bochum, Germany*, Vol. 1 (1991).

[13] G. Mauer, R. Vaßen, and D. Stöver, "Plasma and particle temperature measurements in thermal spray: approaches and applications," *J. Therm. Spray Tech.*, 20 (2011) 391-406.

[14] R. Ye, T. Ishigaki, J. Jurewiez, P. Proulx, and M. I. Boulos, "In-flight spheroidization of alumina powders in Ar–$H_2$ and Ar–$N_2$ induction plasmas," *Plasma Chem. Plasma Proc.*, 24 (2004): 555-571.

[15] M. P. Planche, J. F. Coudert, and P. Fauchais: "Velocity measurements for arc jets produced by a DC plasma spray torch," *Plasma Chem. Plasma Proc.*, 18 (1998) 263-283.

[16] K. Etemadi and E. Pfender: "Impact of anode evaporation on the anode region of a high-intensity argon arc," *Plasma Chem. Plasma Proc.*, 5 (1985) 175-182.

[17] W. H. Peter, T. Muth, W. Chen, Y. Yamamoto, B. Jolly, N. A. Stone, G. M. D. Cantin, J. Barnes, M. Paliwal, R. Smith, J. Capone, A. Liby, J. Williams, and C. Blue, "Titanium Sheet Fabricated from Powder for Industrial Applications," *JOM.*, 64 (2012) 566-571.

[18] A. V. Besov and I. K. Batrak, "Application of technology of plasma spraying in the fabrication of articles for medical devices," *Powder Metall. Met. Ceram.*, 44 (2005)

511-516.

[19] F. F. O. Orumwense, B. A. Okorie, E. O. Okeakpu, E. N. Obiora, and L. I. Onyeji "Sintered copper–graphite powder compacts for industrial applications," *Powder metallurgy,* 44 (2001) 62-66.

[20] K. Byrappa and T. Adschiri, "Hydrothermal technology for nanotechnology," P*rog. Cryst. Growth Charact. Mater.,* 53 (2007) 117-166.

[21] Brian G. Trewyn, Igor I. Slowing, Supratim Giri, Hung-Ting Chen, and Victor S.-Y. Lin, "Synthesis and Functionalization of a Mesoporous Silica Nanoparticle Based on the Sol–Gel Process and Applications in Controlled Release," *Acc. Chem. Res.*, 40 (2007) 846-853.

[22] Jian-Feng Chen, Yu-Hong Wang, Fen Guo, Xin-Ming Wang, and Chong Zheng, "Synthesis of Nanoparticles with Novel Technology: High-Gravity Reactive Precipitation," *Ind. Eng. Chem. Res.*, 39 (2000) 948-954.

[23] Tae-Hee Kim, Sooseok Choi and Dong-Wha Park, "Effects of $NH_3$ Flow Rate on the Thermal Plasma Synthesis of AlN Nanoparticles," *J. Korean Phys. Soc.*, 63, No. 10 (2013) 1864-1870.

[24] Dong-Wook Kim and Dong-Wha Park, "Preparation of indium tin oxide (ITO) nanoparticles by DC arc plasma," *Surf. Coat. Tech.*, 205 (2010) S201-S205.

[25] Dong-Wook Kim, Tae-Hee Kim, Hyun-Woo Park, and Dong-Wha Park, "Synthesis of nanocrystalline magnesium nitride ($Mg_3N_2$) powder using thermal plasma," *Appl. Surf. Sci.*, 257 (2011) 5375-5379.

[26] Sneha Samal, Dong-Wook Kim, Kyo-Seon Kim, and Dong-Wha Park, "Direct synthesis of $TiO_2$ nanoparticles by using the solid-state precursor $TiH_2$ powder in a thermal plasma reactor," *Chem. Eng. Res. Des.*, 90 (2012) 1074-1081.

[27] Sooseok Choi, Jiro Matsuo, and Takayuki Watanabe, "Synthesis of $AlB_{12}$ and $YB_{66}$ Nanoparticles by RF Thermal Plasmas," *J. Phys.*, 441 (2013) 012030.

[28] Sooseok Choi, Jiro Matsuo, Yingying Cheng, and Takayuki Watanabe, "Preparation of boron-rich aluminum boride nanoparticles by RF thermal plasma," *J. Nanopart. Res*, 15 (2013) 1820.

[29] Soo-Jung Lee, Jinsub Choi, and Dong-Wha Park, "Synthesis of ZnO nanopowders by DC thermal plasma for dye-sensitized solar cells", *Mater. Sci. Eng. B*, 178 (2013) 489– 495.

[30] G. Vissokov, Lv. Grancharov, Tsv. Tsvetanov, "On the Plasma-Chemical Synthesis of Nanopowders," *Plasma Sci. Tech.*, 5 (2003) 2039-2050.

[31] Dieter Vollath, "Plasma synthesis of nanopowders," *J. Nanopart. Res*, 10 (2008) 39–57.

[32] Jun Ho Seo, Dong Uk Kim, Jun Seok Nam, Sang Hee Hongw, Sung Bum Sohn and Soon Mo Song, "Radio Frequency Thermal Plasma Treatment for Size Reduction and Spheroidization of Glass Powders Used in Ceramic Electronic Devices," *J. Am. Ceram. Soc.*, 90 (2007) 1717–1722.

[33] Wonkyung Lee, Sooseok Choi, Seung-Min Oh and Dong-Wha Park, "Preparation of spherical hollow alumina particles by thermal plasma," *Thin Solid Films*, 529 (2013) 394–397.

[34] Z. Károly and J. Szépvölgyi, "Plasma spheroidization of ceramic particles," *Chem. Eng. Proc.*, 44 (2005) 221–224.

[35] Soon Cheon Cho, Yong Cheol Hong, and Han Sup Uhm, "A synthesis of purified aluminum fluoride powder by atmospheric microwave-plasma torch", *Jpn. J. Appl. Phys.*, 47 (2008) 297-300.

[36] Vivekanand Kumar, Jeong H. Kim, Chandrashekhar Pendyala, Boris Chernomordik, and Mahendra K. Sunkara, Gas-Phase, bulk production of metal oxide nanowires and nanoparticles using a microwave plasma jet reactor, *J. Phys. Chem. C*, 112 (2008) 17750-17754.

[37] Takeo Hyodo, Masayuki Murakami, Yasuhiro Shimizu, and Makoto Egashira, Preparation of hollow alumina microspheres by microwave-induced plasma pyrolysis of atomized precursor solution, *J. Euro. Ceram. Soc.*, 25 (2005) 3563-3572.

[38] K. Murugan, S. B. Chandrasekhar, and J. Joardar, Nanostructured α/β-tungsten by reduction of $WO_3$ under microwave plasma, *Int. J. Refract. Met. Hard Mater.*, 29 (2011) 128-133.

[39] Yong Cheol Hong, Jong Hun Kim, Soon Cheon Cho, and Han Sup Uhm, *Phys. Plasmas*, 13 (2006) 063506.

[40] Jalal Azadmanjiri, George P. Simon, Kiyonori Suzuki, Cordelia Selomulya and John D. Cashion, “Phase reduction of coated maghemite ($\gamma$-$Fe_2O_3$) nanoparticles under microwave-induced plasma heating for rapid heat treatment,” *J. Mater. Chem.*, 22 (2012) 617–625.

[41] Chan Uk Bang, Yong Cheol Hong, and Han Sup Uhm, “Synthesis and characterization of nano-sized nitride particles by using an atmospheric microwave plasma technique”, *Surf. Coat. Tech.*, 201 (2007) 5007-5011.

[42] Yong Cheol Hong, Taihyeop Lho, Bong Ju Lee, Han Sup Uhm, O Pil Kwon, and Suck Hyun Lee, “Synthesis of titanium dioxide in $O_2$/Ar/$SO_2$/$TiCl_4$ microwave torch plasma and its band gap narrowing”, *Curr. Appl. Phys.*, 11 (2011) 517-520.

[43] Shou Zhe Li, Y. C. Hong, Han. S. Uhm, and Zhe Kui Li, “Synthesis of nanocrystalline iron oxide particles by microwave plasma jet at atmospheric pressure”,

*Jpn. J. Appl. Phys.*, 43 (2004) 7714-7717.

[44] J. H. W. De Wit, “Structural Aspects and Defect Chemistry in $In_2O_3$,”*J. Solid State Chem.*, 20 (1977) 143-148.

[45] P. D. CKing and T. D. Veal, “Conductivity in transparent oxide semiconductors,” *J. Phys.: Condens. Matter*, 23 (2011) 334214.

[46] Vishal D. Ashok and S. K. De, “Growth Kinetics of Self-Assembled Indium Hydroxide and Oxide in Electrolytic Alkali Halide Solution,” *J. Phys. Chem.*, 115 (2011) 9382–9392.

[47] J. Xua, X. Wang, J. Shen, “Hydrothermal synthesis of $In_2O_3$ for detecting $H_2S$ in air,” *Sens. Actuators B*, 115 (2006) 642–646.

[48] T. Sato, “Preparation and thermal decomposition of indium hydroxide,” *J. Therm. Ana. Calorim.*, 82 (2005) 775–782.

[49] T. Mitsui, T. Matsui, R. Kikuchi, and K. Eguchi, “Microstructural Transformation with Heat-Treatment of Aluminum Hydroxide with Gibbsite Structure,” *Chem. Soc. Jpn.*, 82 (2009) 618–623.

[50] M. Figlarz, J. Guenot and F. Fievet-Vincent, “Morphological and topotactical aspects of the reactions $Co(OH)_2 \rightarrow CoOOH$ and $CoOOH \rightarrow Co_3O_4$,” *J. Mater. Sci.*, 11 (1976) 2267-2270.

[51] H. Naono and K. Nakai, “Thermal Decomposition of γ-FeOOH Fine Particles,” *J. Colloid Interface Sci.*, 128 (1989) 146-156.

[52] M. Hafeez, T. Zhai, A. S. Bhatti, Y. Bando, and D. Golberg, “Oxygen Vacancy Driven Modulations in $In_2O_3$ Pyramidal Beaded Nanowires”, *Cryst. Growth Des.*, 12 (2012) 4935–4943.

[53] V. Golovanov, M. A. Maki-Jaskari, T. T. Rantala, G. Korotcenkov, V. Brinzari, A.

Cornet, and J. Morante, “Experimental and theoretical studies of indium oxide gas sensors fabricated by spray pyrolysis”, *Sens. Actuators B,* 106 (2005) 563-571.

[54] P. K. BISWAS, A. DE, L. K. DUA, and L. CHKODA, “Surface characterization of sol–gel derived indium tin oxide films on glass”, *Bull. Mater. Sci.*, 29 (2006) 323-330.

[55] H. P. Song, A. L. Yang, H. Y. Wei, Y. Guo, B. Zhang, G. L. Zheng, S. Y. Yang, X. L. Liu, Q. S. Zhu, Z. G. Wang, T. Y. Yang, and H. H. Wang, “Determination of wurtzite InN/cubic $In_2O_3$ heterojunction band offset by x-ray photoelectron spectroscopy”, *Appl. Phys. Lett.,* 94 (2009) 222114.

[56] G. TYULIEV, and S. ANGELOV, “THE NATURE OF EXCESS OXYGEN IN $Co_3O_{4+\varepsilon}$”, *Appl. Surf. Sci.,* 32 (1988) 381-391.

[57] M. Himmerlich, Ch. Y. Wang, V. Cimalla, O. Ambacher, and S. Krischok, “Surface properties of stoichiometric and defect-rich indium oxide films grown by MOCVD,” *J. Appl. Phys.*, 111 (2012) 093704.

[58] V. B. Okhotnikov, B. I. Yakobson, and N. Z. Lyakhov, “Kinetics of thermal dehydration of $Li_2SO_4 \cdot H_2O$”, *React. Kinet.Catal.Lett.*, 23(1983) 125-130.

[59] V.B. Okhotnikov, S.E. Petrov, B.I. Yakobson, and N.Z. Lyakhov, “Thermal decomposition of materials with layered structures - dehydration of calcium sulphate dii-iydrate single crystals”, *React. Solids*, 2 (1987) 359-372.

[60] Y. Seto, H. Sato, and Y. Masuda, “Effect of water vapor pressure on thermal dehydration of lithium sulfate monohydrate”, *Thermochim. Acta*, 388 (2002) 21-25.

[61] L.J. Love, J.F. Jansen, T.E. Mcknight, Y. Roh, T.J. Phelps, L.W. Yeary, and G.T. Cunningham, “Ferrofluid field induced flow for microfluidic applications”, *IEEE ASME Trans. Mechatronics.,* 10 (2005) 68.

[62] M. Gonzales-Weimuller, M. Zeisberger, and K. M. Krishnan, “Size-dependant

heating rates of iron oxide nanoparticles for magnetic fluid hyperthermia”,*J.Magn.Magn.Mater.* 321 (2009) 1947.

[63] A. Chakraborty, “Kinetics of the reduction of hematite to magnetite near its Curie transition”,*J.Magn.Magn.Mater.* 204 (1999) 57.

[64] D.K. Kim, M. Mikhaylova, F. H. Wang, J. Kehr, B. Bjelke, Y. Zhang, T. Tsakalakos, and M. Muhammed, “Starch-coated superparamagnetic nanoparticles as MR contrast agents”,*Chem. Mater.* 15 (2003) 4343.

[65] C. Corot, P. Robert, J. Idée, and M. Port, “Recent advances in iron oxide nanocrystal technology for medical imaging. Advanced drug delivery reviews”,*Adv. Drug Deliv. Rev.* 58 (2006) 321.

[66] A.K. Gupta and S. Wells, “Surface-modified superparamagnetic nanoparticles for drug delivery: preparation, characterization, and cytotoxicity studies”,*IEEE Trans. Nanobiosci.* 3 (2004) 66.

[67] P. I. Girginova, A. L. Daniel-da-Silva, C. B. Lopes, P. Figueira, M. Otero, V. S. Amaral, E. Pereira, and T. Trindade, “Silica coated magnetite particles for magnetic removal of $Hg^{2+}$ from water”, *J. Colloid Interface Sci.* 345 (2010) 234.

[68] C. E. Sjögren, C. Johansson, A. Nevestadn, P. C. Sontum, K. Briley- Sæbø , and A. K. Fahlvikf, “Crystal size and properties of superparamagnetic iron oxide (SPIO) particles. Magnetic resonance imaging”, *Magn. Reson. Imaging* 15 (1997) 55.

[69] E. H. Mert, H. Yıldırım, A. T. Üzümcü, and Hüseyin Kavas, “Synthesis and characterization of magnetic polyHIPEs with humic acid surface modified magnetic iron oxide nanoparticles”, *React. Funct. Polym.*, 73 (2013) 175-181.

[70] G. Sharma and P. Jeevanandam, “Synthesis of self-assembled prismatic iron oxide nanoparticles by a novel thermal decomposition route”, *RSC Advances*, 3 (2013)

189-200.

[71] P. Xu, Gu. Zeng, D. Huang, S. Hu, C. Feng, C. Lai, M. Zhao, C. Huang, N. Li, Z. Wei, and G. Xie, “Synthesis of iron oxide nanoparticles and their application in Phanerochaete chrysosporium immobilization for Pb(II) removal”, *Colloids and Surfaces A: Physicochem. Eng. Aspects*, 419 (2013) 147-155.

[72] S. Liza E. and P.V. Mohanan, “Dextran stabilized iron oxide nanoparticles: Synthesis, characterization and in vitro studies”, *Carbohyd. Polym.*, 92 (2013) 726-732.

[73] X. Liu, X. Meng, and J. Zhao, “Synthesis of nanocrystalline iron oxides with mesostructure as desulfurizer”, *Mater. Lett.*, 92 (2013) 255-258.

[74] D. Vollath, D. V. Szabó, R. D. Taylor, J. O. Willis, and K. E. Sickafus, “Synthesis and Properties of Nanocrystalline Superparamagnetic $\gamma$-$Fe_2O_3$”, *NanoStruct. Mater.*, 6 (1995) 941-944.

[75] D. Vollath, D. V. Szabó, R. D. Taylor, and J. O. Willis, “Synthesis and magnetic properties of nanostructured maghemite”, *J. Mater. Res.*, 12 (1997) 2175-2182.

[76] J. Grabis, G. Heidemane, and D. Rašmane, “Preparation of $Fe_3O_4$ and $\gamma$-$Fe_2O_3$ nanoparticles by liquid and gas phase processes”, *Mater. Sci.*, 14 (2008) 292-295.

[77] T. E. Babutina, N. V. Boshitska, O. A. Ivashchenko, A. O. Perekos, V. Z. Voinash, and I. V. Uvarova1, “NANOSIZED IRON AND IRON OXIDE POWDERS PROMISING FOR MEDICINE”, *Powder Metall. Met. Ceram.*, 48 (2009) 365-370.

[78] C. Huang, C. Hou, C. Chen, Y. Tsai, L. Chang, H. Wei, K. Hsieh, and C. Chan, “Magnetic $SiO_2/Fe_3O_4$ colloidal crystals”, *Nanotechnology*, 19 (2008) 055701.

[79] M.E. Khosroshahi and L.Ghazanfari, “Preparation and characterization of silica-coated iron-oxide bionanoparticles under $N_2$ gas”, *Physica E* 42 (2010) 1824.

[80] Y. Kobayashi, S. Saeki, M. Yoshida, D. Nagao, and M. Konno, “Synthesis of

spherical submicron-sized magnetite/silica nanocomposite particles", J. *Sol-Gel Sci. Tech.* 45 (2008) 35.

[81] Ding Zhou, Tian-Long Zhang, and Bao-Hang Han, One-step solvothermal synthesis of an iron oxide–graphene magnetic hybrid material with high porosity, *Micropor. Mesopor. Mater.*, 165 (2013) 234-239.

[82] R. G. Mendes, B. Koch, A. Bachmatiuk, A. A. El-Gendy, Y. Krupskaya,A. Springer, Rü. Klingeler, O. Schmidt, B. Büchner, S. Sanchez, M. H. Rümmeli, "Synthesis and toxicity characterization of carbon coated iron oxide nanoparticles with highly defined size distributions", *Biochimica et Biophysica Acta*,1840 (2014) 160–169.

[83] H. Bae, T. Ahmad, I. Rhee, Y. Chang, S. U. Jin, and S. Hong, "Carbon-coated iron oxide nanoparticles as contrast agents in magnetic resonance imaging", Nanoscale Research Letter, 7:44 (2012)

[84] M. N. Nadagouda and D. A. Lytle, "Microwave-Assisted Combustion Synthesis of Nano Iron Oxide/Iron-Coated Activated Carbon, Anthracite, Cellulose Fiber, and Silica, with Arsenic Adsorption Studies", *J. Nanotech.*, 2011 (2011) 8.

[85] Alexandra Teleki, Marcel Suter, Piran R. Kidambi, Olgac Ergeneman, Frank Krumeich, Bradley J. Nelson, and Sotiris E. Pratsinis, "Hermetically Coated Superparamagnetic $Fe_2O_3$ Particles with $SiO_2$ Nanofilms," *Chem. Mater.*, 21 (2009) 2094–2100.

[86] R. Snovski, J. Grinblat, M. Sougrati, J. Jumas, and S. Margel, "Synthesis andcharacterizationofiron,ironoxide and ironcarbidenanostructures", *J. Magn. Magn. Mater.* 349 (2014) 35-44.

[87] R. Krishnaveni, "Synthesis of Iron Oxide Coated Nickel Oxide Nanoparticles and Its Characterization", Proceeding of ICANMEET-2013 (2013).

[88] E. Iglesias-Silva, J.L. Vilas-Vilela, M.A. López-Quintela, J. Rivas, and M. Rodríguez, L.M. Leóna, *J.Non-Cryst. Solids* 356 (2010) 1233–1235.

[89] Sheryl H. Ehrmana and Sheldon K. Friedlander, "Phase segregation in binary $SiO_2$/$TiO_2$ and $SiO_2$/$Fe_2O_3$nanoparticle aerosols formed in a premixed flame," *Journal of Materials Research*, 14 (1999) 4551-4561.

[90] D. Li, W. Y. Teoh, C. Selomulya, R. C. Woodward, R. Amal, and B. Rosche, "Flame-Sprayed Superparamagnetic Bare and Silica-Coated Maghemite Nanoparticles: Synthesis, Characterization, and Protein Adsorption-Desorption," *Chem. Mater.*, 18 (2006) 6403-6413.

[91] J. L. H. Chau, M. K. Hsu, and C. C. Kao, "Microwave plasma synthesis of Co and SiC-coated Co nanopowders", *Mater. Letters* 60 (2006) 947.

[92] D.W. Jung and D.W. Park, "Synthesis of nano-sized antimony-doped tin oxide (ATO) particles using a DC arc plasma jet," *Appl. Surf. Sci.*, 255 (2009) 5409–5413.

[93] I. Mohaia, L. Gal, J. Szepvolgyi, J. Gubicza and Z. Farkas, "Synthesis of nanosized zinc ferrites from liquid precursors in RF thermal plasma reactor," *Journal of the European Ceramic Society*, 27 (2007) 941–945.

[94] S. Rizk, M.B. Assouar, C. Gatel, M. Belmahi, J. Lambert and J. Bougdira, "Synthesis of carbon coated β-SiC nanofibers by microwave plasma assisted chemical vapour deposition in $CH_4$/$H_2$ gas mixture," *Diamond & Related Materials*, 17 (2008) 1660–1665.

[95] NIST Chemistry WebBook, http://webbook.nist.gov/chemistry/

[96] P. Lei, A. M. Boies, S. Calder, and S. L. Girshick, "Thermal plasma synthesis of superparamagnetic iron oxide nanoparticles", *Plasma Chem. Plasma Process*, 32 (2012) 519-531.

[97] A. Abdali, B. Moritz, A.Gupta, H. Wiggers and C. Schulz, "Hybrid microwave-plasma hot-wall reactor for synthesis of silica nanoparticles under well-controlled conditions," *Journal of Optoelectronics and Advanced Materials*," 12 (2010) 440 – 444.

[98] W. Kim, C. Y. Suh, S. W.k Cho, K. M. Roh, H. Kwon, K. Song and I. J. Shon, "A new method for the identification and quantification of magnetite–maghemite mixture using conventional X-ray diffraction technique," *Talanta*, 94 (2012) 348– 352.

[99] C.J. Goss, "Saturation Magnetisation, Coercivity and Lattice Parameter Changes in the System $Fe_3O_4$-$\gamma$-$F_2O_3$, and Their Relationship to Structure," *Phys. Chem. Minerals,* 16 (1988) 164-171.

[100] T. Yamanaka and M. Okita, "Magnetic properties of the $Fe_2SiO_4$-$Fe_3O_4$ spinel solid solutions," *Phys. Chem. Minerals*, 28 (2001) 102-109.

[101] T. Yamanaka, H. Shimazu, and K. Ota, "Electric conductivity of $Fe_2SiO_4$-$Fe_3O_4$ spinel solid solutions," *Phys. Chem. Minerals*, 28 (2001) 110-118.

[102] Anna Fischer, Manuel Schmitz, Barbara Aichmayer, Peter Fratzl, and Damien Faivre, "Structural purity of magnetite nanoparticles in magnetotactic bacteria," *J. R. Soc. Interface*, 8 (2011) 1011-1018.

[103] K. Haneda, and A. H. Morrish, "Magnetite to Maghemite Transformation in Ultrafine Particles," *J. Physique*, 38 (1977) C1-321.

[104] C. Chou, J. Phillips, "Plasma production of metallic nanoparticles", *J. Mater. Res.*, 7 (1992) 2107-2113.

[105] D. Vollath, and D. V. Szab´o, R. D. Taylor, and J. O. Willis, "Synthesis and magnetic properties of nanostructured maghemite," *J. Mater. Res.*, 12 (1997) 2175-2182.

[106] O. B. Fabrichnaya, and B. Sundman, “The assessmeut of thermodynamic parameters in the Fe-O and Fe-Si-O systems,” *Gembimica et Cosmochimica Acta*, 61 (1997) 4539-4555.

[107] Tae-Hee Kim, Sooseok Choi, Dong-Wook Kim, and Dong-Wha Park, “Simulation on preparation of metal nitride particle by thermal plasma”, Institute for Computational Fluids Dynamics (ICFD) 2010 Conference (2010)

[108] A. Averroes, “The treatment of airborne asbestos with atmospheric pressure microwave air plasma”, PhD. thesis, Tokyo Institute of Technology, 2011.

[109] 神沢 淳, “プラズマ伝熱”, 信山社出版, Tokyo, 1992.

[110] D. A. Ramappa and W. B. Henley, “Diffusion of Iron in Silicon Dioxide”, *J. Electrochem. Soc.*, 146 (1999) 3773-3777.

# Acknowledgements

Above all, I express deeply appreciation to my supervisor, Prof. Hidetoshi Sekiguchi who gave guidance for me to become a researcher. Due to his guidance and support, I could accomplish my doctoral course. He made me grow internally as well as academically. I never forgot what I was taught by him. I also thank to Prof. Masaaki Suzuki, Prof. Dong-Wha Park, Prof. Wiwut Tanthapanichakoon, Prof. Shinsuke Mori and Prof. Yusuke Shimoyama for examining my thesis and giving the valuable comments. Especially I should express my gratitude to Prof. Dong-Wha Park who is the supervisor on my master's course at Inha University. Due to his support, I could conduct my doctoral course in Tokyo Institute of Technology and start the research on the plasma processing. Next, I appreciate Prof. Kodama for supporting my research with the careful attention. I greatly appreciate all of the members of Sekiguchi Laboratory including who already graduated as well as are currently affiliated. I also appreciate the members of Park Laboratory in Inha University, especially Mrs. Tae-Hee Kim, who helped the experiments using the thermal plasma. Dr. Sooseok Choi also gave me many comments about the plasma, so that I appreciate him. I appreciate staffs of Center for Advanced Materials Analysis for giving advices about the material analysis as well as corresponding my requests. I am also grateful to Moritani Scholarship Foundation for the financial support.

Finally, I would like to express my special thanks to my family; my grandmother, my father, my mother and my sister. Always my family supported and cheered me unconditionally. It has been the one of my buttress during my academic course.